

Title	Nanofabrication towards biophotonics
Authors	Jones, Daniel
Publication date	2015
Original Citation	Jones, D. 2015. Nanofabrication towards biophotonics. PhD Thesis, University College Cork.
Type of publication	Doctoral thesis
Rights	© 2015, Daniel Jones. - http://creativecommons.org/licenses/by-nc-nd/3.0/
Download date	2024-09-22 12:26:24
Item downloaded from	https://hdl.handle.net/10468/2720

Ollscoil na hÉireann
NATIONAL UNIVERSITY OF IRELAND



Nanofabrication towards Biophotonics

A Thesis Presented to
the National University of Ireland
for the degree of Doctor of Philosophy

by

Daniel Jones

Supervised by Dr. Alan O’Riordan

& Dr. Pierre Lovera



Department of Electrical & Electronic Engineering

&

Tyndall National Institute

University College Cork

January 2015

Declaration

I hereby declare that this thesis is my own work and certify to the best of my knowledge it contains no materials previously published or written by another person, or substantial proportions of material which have been accepted for the award of any other degree or diploma at University College Cork or any other educational institution, except where due acknowledgement is made in the thesis in accordance with the standard referencing practices. Any contribution made to the research by others, with whom I have worked directly at Tyndall National Institute - University College Cork or elsewhere, is explicitly acknowledged in the thesis. I also declare that the intellectual content of this thesis is the product of my own work, except to the extent that assistance from others in the project's design and conception or in style, presentation and linguistic expression is acknowledged.

I declare that this is a true copy of my thesis, including any final revisions, as approved by my thesis committee and the Graduate Studies office, and that this thesis has not been submitted to any other University or Institution.

Daniel Jones

Table of Contents

Chapter 1: Introduction

1.1	Introduction to thesis.....	3
1.2	Introduction to plasmonics.....	3
1.2.1	Bulk plasmons.....	4
1.2.2	Surface plasmons.....	7
1.2.2.1	Localised Surface Plasmons (LSP).....	7
1.2.2.2	Gold nanoparticles for label-free sensing applications.....	8
1.2.2.3	LSP in nanoholes.....	9
1.2.2.4	Surface plasmon polaritons (SPP).....	10
1.2.2.5	Wave vectors.....	11
1.2.2.6	Methods to excite SPPs.....	12
1.3	Plasmonic array of nanoholes.....	16
1.3.1	Optical properties.....	16
1.3.2	Simulations.....	21
1.3.3	Fabrication of nanoplasmonic structures.....	22
1.3.3.1	Top down approaches.....	22
1.3.3.2	Self-assembly methods.....	26
1.4	Nanohole arrays: applications to biosensing.....	29
1.4.1	Applications.....	29
1.4.2	Existing Biosensing Technologies.....	31
1.4.3	Kretschman vs Nanohole.....	35
1.4.4	General challenges to point of care diagnostics.....	35
1.5	Scope of Thesis.....	37
1.6	References.....	38

Chapter 2: Fabrication of plasmonic nanohole arrays and their use as label free biosensors

2.1	Introduction.....	53
2.2	Experimental.....	55
2.2.1	Metal evaporation.....	55
2.2.2	FIB milling.....	55
2.2.3	Lift off.....	55
2.2.4	Simulations.....	55
2.2.4.1	Computational volume.....	56
2.2.4.2	Permittivity of gold.....	56
2.2.4.3	Transmission spectra.....	57

2.2.5	Optical images.....	57
2.2.6	Transmission spectra.....	57
2.2.7	SEM.....	58
2.2.8	AFM.....	58
2.2.9	Bulk refractive index sensing.....	58
2.2.10	Attachment chemistry.....	58
2.2.10.1	Gold cleans.....	58
2.2.10.2	Sensor biomodification.....	59
2.2.11	SPR assay.....	60
2.3	Results and discussion.....	61
2.3.1	Structural characterisation.....	61
2.3.2	Spectroscopic characterisation.....	64
2.3.3	Simulations.....	66
2.3.4	Bulk refractive index measurements.....	67
2.3.5	Assay development.....	69
2.3.5.1	Gold attachment.....	69
2.3.5.2	Surface Plasmon Resonance.....	70
2.3.6	Bio assay on nanohole array.....	71
2.4	Summary and Conclusion.....	73
2.5	References.....	74

Chapter 3: Development of a point of care platform for label-free, multiplexed, real-time detection of cancer biomarkers

3.1	Introduction.....	81
3.2	Experimental.....	82
3.2.1	Fabrication of nanohole arrays.....	82
3.2.2	Optical setups.....	82
3.2.2.1	Measuring intensity from direct transmission.....	82
3.2.2.2	Measuring the spectrum from direct transmission.....	84
3.2.3	Microfluidic delivery.....	85
3.2.3.1	Microfluidic setup.....	85
3.2.3.2	Integration of microfluidics with nanohole sensors.....	86
3.2.4	Assay procedures.....	86
3.2.4.1	SPR-2 assays.....	87
3.2.4.2	Assays on the microscope.....	88
3.2.4.3	Assays on the custom built system.....	89
3.3	Results and discussion.....	91

3.3.1	Selection and characterisation of bioprobes and assay development.....	91
3.3.1.1	Selection of biomarkers	91
3.3.1.2	Assay development on SPR2.....	91
3.3.1.3	Characterisation of bioprobes	92
3.3.1.4	Optimised assay	94
3.3.2	Development of the optical readout platform	95
3.3.2.1	Optical designs.....	95
3.3.2.2	Spectral acquisition.....	97
3.3.2.3	LabVIEW acquisition	98
3.3.2.4	System resolution.....	99
3.3.3	Assay experiments	101
3.3.3.1	Assays on the commercial microscope.....	101
3.3.3.2	Real time assays	105
3.4	Summary and Conclusion	109
3.5	References	110

Chapter 4: Arrays of anisotropic shaped nanoholes and novel applications

4.1	Introduction	112
4.2	Experimental	113
4.2.1	Fabrication.....	113
4.2.2	Optical characterisation.....	113
4.2.3	FDTD simulations of nanohole arrays	114
4.2.3.1	Transmission spectrum	115
4.3	Results and discussion	116
4.3.1	Characterisation of the nanohole arrays.....	116
4.3.2	FDTD simulated near field profiles	118
4.3.3	Application as anti-counterfeiting tag.....	121
4.4	Summary and Conclusion	123
4.5	References	124

Chapter 5: Summary, Conclusion and Future Work

5.1	Summary and Conclusion	130
5.2	Future Work	131

Appendices	139
-------------------------	-----

Abstract

This thesis explores methods for fabrication of nanohole arrays, and their integration into a benchtop system for use as sensors or anti-counterfeit labels. Chapter 1 gives an introduction to plasmonics and more specifically nanohole arrays and how they have potential as label free sensors compared to the current biosensors on the market. Various fabrication methods are explored, including Focused Ion Beam, Electron Beam Lithography, Nanoimprint lithography, Template stripping and Phase Shift Lithography. Focused Ion Beam was chosen to fabricate the nanohole arrays due to its suitability for rapid prototyping and its relatively low cost. In chapter 2 the fabrication of nanohole arrays using FIB is described, and the samples characterised. The fabricated nanohole arrays are tested as bulk refractive index sensors, before a bioassay using whole molecule human IgG antibodies and antigen is developed and performed on the sensor. In chapter 3 the fabricated sensors are integrated into a custom built system, capable of real time, multiplexed detection of biomolecules. Here, scFv antibodies of two biomolecules relevant to the detection of pancreatic cancer (C1q and C3) are attached to the nanohole arrays, and detection of their complementary proteins is demonstrated both in buffer (10 nM detection of C1q Ag) and human serum. Chapter 4 explores arrays of anisotropic (elliptical) nanoholes and shows how the shape anisotropy induces polarisation sensitive transmission spectra, in both simulations and fabricated arrays. The potential use of such samples as visible and NIR tag for anti-counterfeiting applications is demonstrated. Finally, chapter 5 gives a summary of the work completed and discusses potential future work in this area.

Acknowledgments

Firstly, I would like to thank Dr. Alan O’Riordan for giving me the opportunity to complete my PhD at the Tyndall National Institute. His guidance, advice and mentoring has been invaluable and I have learned a great deal from him over the course of my PhD.

I also wish to thank Dr. Pierre Lovera. His Viva was the first I experienced, a short time after starting, and due to all his guidance, time and help, I have reached that stage too.

I also would like to thank the other supervisors and post docs (past and present) of the Nanotechnology group for their advice and their time whenever I needed it: Dr. Aidan Quinn, Dr. Mary Manning, Dr. Hugh Doyle, Dr Daniela Iacopino, Dr Brenda Long, Dr Claire Barrett, Dr Nicolas Sassiati, Dr Karen Dawson, Dr Micheál Burke, and Dr Armelle Montrose.

I would particularly like to thank all the students in the nanotechnology group and the friends I have made in Tyndall throughout the years, for the many social gatherings that were a welcome distraction.

Thanks to my parents for all the support they always give, and to my brothers.

Last, but not least, thanks Micki.

Daniel

To my family

Chapter 1

Introduction

1.1 Introduction to thesis

This thesis explores the potential of nanohole arrays for use in label free, real time sensing, of pancreatic biomarkers, both in buffer and human serum. The introduction focuses on plasmonics and describes the plasmonic effects that occur on nanohole arrays. Fabrication methods are explored, including top down and self-assembly approaches, and the pros and cons to each method discussed. The fabrication method chosen, using Focused Ion Beam, is described in detail in the second chapter along with the characterisation of the fabricated samples. To explore the sensing potential of the nanohole arrays, simulations and bulk refractive index measurements are performed. Cleans are explored to attach biomolecules to the nanohole arrays and the successful detection of IgG antibodies and antigen confirms that the nanohole arrays are suitable for sensing applications. In chapter 3, the nanohole arrays are incorporated into an optical setup allowing for real time measurements from a dedicated LabVIEW program. This setup is integrated with microfluidic pumps, and assays using pancreatic cancer biomarkers are developed. Using the custom built setup, real time detection of the cancer biomarkers, in buffer and human serum, is achieved. Finally, chapter 4 explores the polarisation dependent spectra that are exhibited from arrays of elliptical nanoholes. Simulations are performed to give an understanding of the physics behind this and the potential of these arrays for anti-counterfeiting is shown.

1.2 Introduction to plasmonics

The field of plasmonics is the study of interactions of electromagnetic radiation (light) and metallic interfaces. It is a broad research field with potential applications ranging from faster data transmission [1], mask less high resolution lithography [2], more efficient light emitting diodes [3, 4] and data storage [5] to even more unusual fields, such as holograms [6] and invisibility cloaks [7]. The applications within the medical and biological fields include: imaging, sensing, spectral analysis, targeted drug delivery, manipulation and heating of biomolecules or cells using plasmonic effects [8]. The heating of gold nanoparticles, to kill the cells they are attached to, is being investigated as a method of cancer treatment [9]. In addition to all of these potential applications for plasmonics there is a large amount of research on bioanalytical sensors [10, 11].

1.2.1 Bulk plasmons

Plasmons can be described as an oscillation of free electron density with respect to the fixed positive ions in a metal. As electrons are displaced, the charge from the ions in the metal exerts an attractive force on the electrons, which attempts to move them back to their original locations. These interactions cause plasmons to oscillate, once they are excited. The frequency at which electrons oscillate in a metal is called the plasma frequency (ω_p) and is defined as [12],

$$\omega_p = \sqrt{\frac{Ne^2}{\epsilon_0 m}} \quad (1.1)$$

where N is the conduction electron density, e is the charge on the electron, m is the electron mass and ϵ_0 is the permittivity of free space.

Table 1.1: Values for electron charge, mass and the permittivity of free space

Charge on electron (e)	$1.60217657 \times 10^{-19}$ coulombs
Electron mass (m)	1 eV or 1.783×10^{-36} kg
Permittivity of free space (ϵ_0)	8.854×10^{-12} F/m

The properties of a bulk material can be described by its relative permittivity or dielectric function (ϵ). In the case of a metal, this dielectric function is a function of the frequency ω . A simple approximation of the dielectric function, is to describe the metal as a free electron gas (where the metal is assumed to be a cloud of free electrons distributed uniformly over the interior of the solid and moving against a fixed background of positive ion cores) with the metal dielectric function ϵ_m given by,

$$\epsilon_m(\omega) = 1 - \frac{\omega_p^2}{\omega^2} \quad (1.2)$$

where ω is the frequency of light and ω_p is the plasma frequency of the metal. The dielectric function is less than 0 for frequencies below the plasma frequency and more than 0 for higher frequencies. For metals such as gold ($\omega_p \sim 1.37 \times 10^{16}$ Hz [13]) and silver ($\omega_p \sim 1.36 \times 10^{16}$ Hz [14]) the frequency of visible light falls below ω_p giving a negative dielectric function. This means that the refractive index (defined as $n = \sqrt{\epsilon}$) is imaginary, meaning the lightwave cannot propagate in the metal and is reflected by it giving it a mirror like surface.

However, in real metals, plasmons are damped by inelastic processes such as collisions of electrons in the material. To take this into account, a damping frequency γ is introduced and ε_m is re-evaluated as,

$$\varepsilon_m(\omega) = 1 - \frac{\omega_p^2}{\omega^2 + i\gamma\omega} \quad (1.3)$$

The dielectric function is complex in this model ($\varepsilon_m = \varepsilon_m' + i\varepsilon_m''$) where [12],

$$\varepsilon_m'(\omega) = 1 - \frac{\omega_p^2}{\omega^2 - \gamma^2} \quad (1.4)$$

$$\varepsilon_m''(\omega) = \frac{\omega_p^2\gamma}{\omega^3 - \omega\gamma^2} \quad (1.5)$$

This characteristic dielectric function for metals is based on the Drude model. For simple real metals at room temperature (e.g. gold and silver) such a response is not found experimentally over all frequencies, but does give a very good approximation at lower frequencies as is shown in Figure 1.1.

For visible light ω is in the order of $4 - 8 \times 10^{15} \text{ Hz}$. For a metal like gold ($\gamma_{Au} \sim 4 \times 10^{13} \text{ Hz}$) [13] γ is much smaller than ω . Hence ε_m'' is small and ε_m' close to that described without damping. At high frequencies, the metal dielectric function approaches 1 according to the equations above. In reality, this is not the case, due to the influence of the positive background of the metal ion cores. The first term of equation (1.3) can be replaced with ε_∞ to take this into account (which is the value that ε_m approaches when $\omega \rightarrow \infty$ [12]).

$$\varepsilon_m(\omega) = \varepsilon_\infty - \frac{\omega_p^2}{\omega^2 + i\gamma\omega} \quad (1.6)$$

This Drude model adequately describes the dielectric function only for metals when the photon energies are below the threshold of the transitions between electronic bands. For noble metals, interband transitions start to occur for energies in excess of 1 eV (See Table 1.2). Above the band edge, photons are very efficient in exciting electrons to higher bands.

Table 1.2: Plasma frequency (ω_p) and frequency of onset for interband transitions (ω_{int}) for metals [15].

	ω_p (eV)	ω_{int} (eV)
Silver	9.2	3.9
Gold	8.9	2.3
Copper	8.7	2.1
Aluminium	12.7	1.41

Figure 1.1 shows a comparison of the modelled dielectric function against measured values for gold. It shows that for energies above 2.3 eV the model is not accurate.

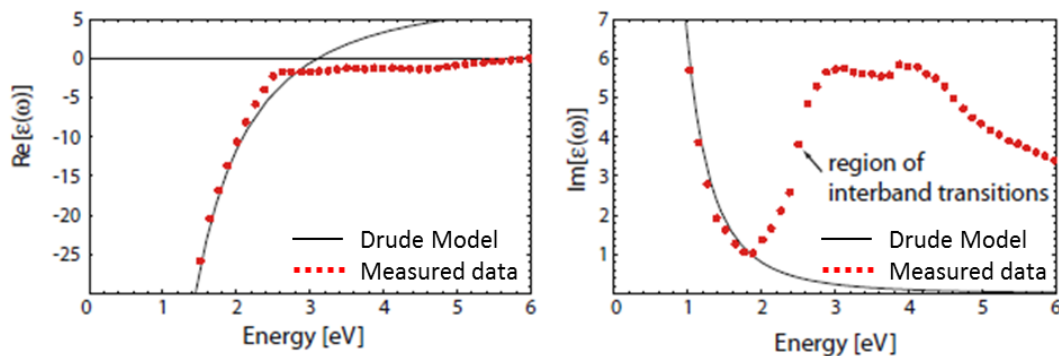


Figure 1.1: Dielectric function of the Drude model of the free electron gas (solid line) compared to measured values for gold (dots) [12].

This is because at 2.3 eV the interband effects start to occur in gold (see Table 1.2). It is at these energies that light is absorbed by gold as electrons from the valence band are excited to the conduction band. It is these interband effects where light is absorbed at certain wavelengths that give metals their distinctive colours. Gold absorbs this blue light and reflects the red and green giving its ‘gold’ colour.

Interband transitions can be described using the classical picture of a bound electron with a resonant frequency. This leads to a Lorentz-Oscillator term that is added to the Drude model. This Drude-Lorentz model gives a good approximation for the dielectric function of metals over the whole frequency range. It can therefore be incorporated into simulations using the finite-difference time-domain (FDTD) scheme and will be used in the following sections.

1.2.2 Surface plasmons

Bulk plasmons can oscillate through the bulk metal but light cannot penetrate the metal to excite them as in accordance with Maxwell's laws; the electric fields only penetrate short distances into the metal surface. However, surface plasmons can be optically excited at the surface of the metal of which there are two distinct types; localised surface plasmons (LSPs) and surface plasmon polaritons (SPPs). LSPs occur when light is shone onto metal nanoparticles and are confined to the boundary of these sub-wavelength particles. On the other hand, SPPs can be excited on flat metal surfaces (at the metal-dielectric boundary) by an electromagnetic force and can propagate along the surface [16]. Both LSPs and SPPs will be described in detail in the following section.

1.2.2.1 Localised Surface Plasmons (LSP)

When light is shone onto metal nanoparticles, the electric field of the light can excite electrons in the conduction band. This results in coherent localised plasma oscillation, as show in Figure 1.2. These excitations are called localised surface plasmons (LSPs) and the resonant frequency depends on the properties of the nanoparticles; including size, geometry and dielectric constant [17]. As light interacts with a particle, it induces a dipole moment that is proportional to the applied electric field *via* the polarisability α . For a sphere that is much smaller than the wavelength of light, the applied electric field can be assumed to be constant over the whole particle. In this electrostatic approximation the polarisability is given by,

$$\alpha = 4\pi a^3 \frac{\epsilon_m(\omega) - n^2}{\epsilon_m(\omega) + 2n^2} \quad (1.7)$$

where n is the refractive index of the dielectric surrounding the particle and a is the radius of the particle. The maximum value for the polarisability will occur when the denominator is minimum, and as, $\epsilon_m'' \ll |\epsilon_m'|$ in the visible region for metals like gold, this occurs (to a first order approximation) when,

$$\epsilon_m'(\omega) = -2n^2 \quad (1.8)$$

This is the Fröhlich condition, corresponding to the resonance condition for excitation of LSPs [12]. From equation 1.8, we see that ϵ_m' must be negative and this limits the excitation of LSPs to metal particles. When the LSP is excited, both absorption and

scattering are greatly enhanced which are effects that can be measured optically. Extinction measurements are used when there are a large amount of nanostructures, such as a solution of nanoparticles [18]. In contrast, scattering measurements based on Dark Field microscopy are used when there is a low density of nanoparticles as there is a much higher signal to noise ratio [19].

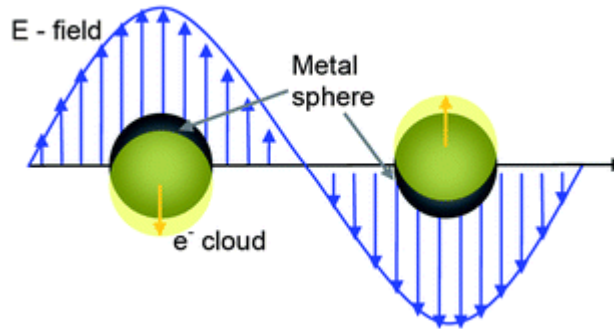


Figure 1.2: Illustration of light interacting with metallic nanoparticles [20].

The optical extinction cross section σ_{ext} of a metal particle was derived by Gustav Mie [21]. For spherical particles, much smaller than the wavelength of light (in the electrostatic dipole limit) the Mie theory is reduced to [12],

$$\sigma_{ext}(\omega) = \frac{12\pi a^3 \omega}{c} n^3 \frac{\varepsilon_m''(\omega)}{[\varepsilon_m'(\omega) + 2n]^2 + \varepsilon_m''(\omega)^2} \quad (1.9)$$

The extinction will be highest at the resonance condition (equation 1.8). The width of the peak is determined by ε_m'' and this explains why noble metals such as gold and silver (with a small ε_m'') have sharp peaks and bright colours.

1.2.2.2 Gold nanoparticles for label-free sensing applications

Although gold nanoparticles have been used for years (in stained glass) it was only in 1998 that LSP was used for sensing. Englebienne et al monitored changes in the plasmon resonance of gold nanoparticles suspended in solution to probe antigen-antibody binding [22]. All sorts of sizes and shapes of particles are now being investigated for their use in biosensing [20, 23-25]. The decay length for nanoparticles is typically on the order of 10's of nanometers [26] meaning the surrounding dielectric of the nanoparticle can be altered by the binding of small biomolecules. Figure 1.3 shows a schematic representation of how the LSP resonance can be used to detect DNA

binding. The yellow peak is the LSP resonance of a single nanoparticle. When for example, capture DNA is bound to the nanoparticle the peak red shifts to the right (the blue peak in Figure 1.3). Upon binding of the complementary target DNA to the capture DNA the peaks shifts further to the right (the red peak). This is caused by the increase in refractive index due to the addition of the biomolecules to the nanoparticle surface displacing solvent molecules, which have a lower refractive index.

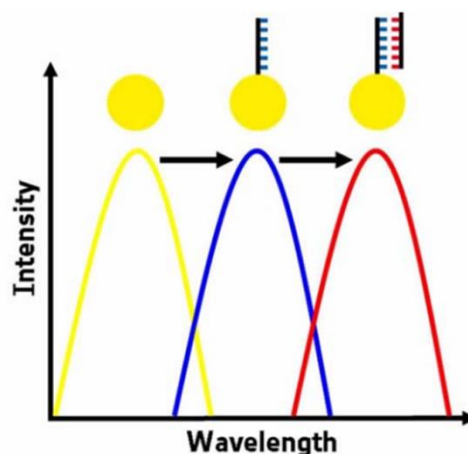


Figure 1.3: Schematic of the LSP resonance of a single nanoparticle (in yellow). There is a red shift when a capture DNA is attached to the particle (blue) and a further shift as the complementary target DNA binds (red) [27].

1.2.2.3 LSP in nanoholes

LSPs can also be sustained by dielectric nanostructures surrounded by metal (the inverse of a metal particle). The induced electric fields of a void and a particle have opposite directions with respect to the applied field [28]. This is illustrated in Figure 1.4.

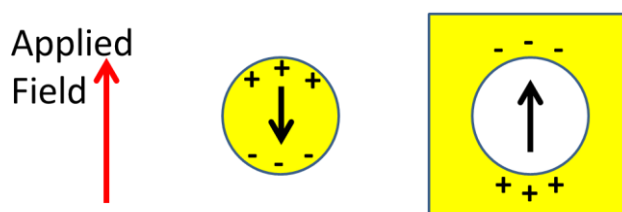


Figure 1.4: Schematic of the plasmon resonances of a particle (on the left) and a void (on the right). The red arrow shows the direction of the applied field and the black arrows show the induced electric field direction.

Similar to a spherical void in metal, single holes also sustain dipolar optical resonances [29, 30]. These single holes have a LSP resonance very similar to the inverse structure (a nanodisk), but with a shorter decay time, as the LSP can decay non-radiatively to SPPs [28]. The sensing capabilities of single nanoholes are similar to that of typical LSPR structures with sensitivity and electric field decay lengths of the same order of magnitude [31].

1.2.2.4 Surface plasmon polaritons (SPP)

Unlike LSP, SPPs are oscillations of the conduction electrons that propagate at the metal-dielectric interface, illustrated in Figure 1.5. When excited by an electromagnetic source, the oscillation of the magnetic field of the SPP is in the plane of the interface, while the electric fields of the SPPs have components in both the direction of the propagation and perpendicular to the interface. The decay length of the field into the dielectric medium depends on both the wavelength of the incident light and the dielectric functions of the metal and dielectric. This length is typically hundreds of nanometers [32]. As the response that is measured in sensing applications is caused by refractive index changes due to biomolecular binding onto the metal, the decay length is important as only molecules within this distance from the surface will alter the dielectric RI and consequently induce change in the SPP.

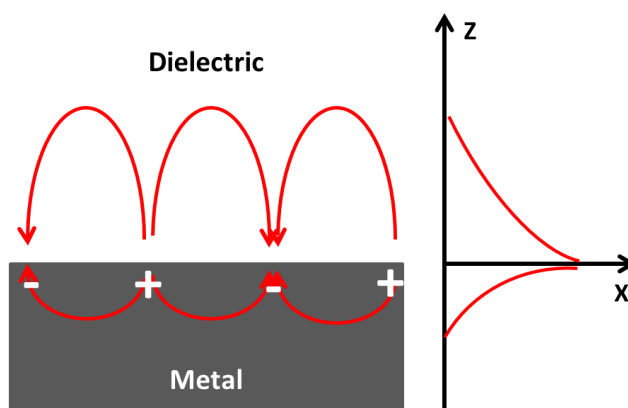


Figure 1.5: Schematic diagram of an SPP propagating on a surface defined by the x-y plane along the x direction. Exponentially decaying electric field as a function of z shown in the x-z coordinate.

1.2.2.5 Wave vectors

The wave vector k_{SPP} describes the momentum carried by the SPP. This is given by the dispersion relation:

$$k_{SPP} = \frac{\omega}{c} \sqrt{\frac{\epsilon_m(\omega) \cdot n^2}{\epsilon_m(\omega) + n^2}} \quad (1.10)$$

where c is the speed of light and n is the refractive index of the dielectric medium. It can be proven, based on this equation, that SPPs are only supported if the real components of the dielectric functions of the interface materials have opposite signs [33]. The interface between a metal (below its plasma frequency, $\epsilon'_m < 0$) and a dielectric (where $\epsilon = n^2$ is real and positive) fulfil these criteria, and thus SPPs are supported.

For a metal with a complex dielectric function, there is also a complex wave vector. The imaginary part gives the losses in the system and determines how far the SPP can propagate on the surface. When the imaginary part is small (such as for gold, $\epsilon_m'' \ll |\epsilon_m'|$, in the visible region) the real part can be approximated by neglecting the imaginary component. With $\epsilon'_m < 0$ and $|\epsilon'_m| > n^2$ we get,

$$k_{SPP} > \frac{\omega}{c} n \quad (1.11)$$

The right hand side of this equation is equal to the wave number for light travelling in the same dielectric medium at frequency ω . The momentum of the SPP is parallel to the interface and therefore it is the parallel component of the photons momentum that is relevant to the excitation of SPPs. For light travelling to the interface at an angle θ , the parallel wave number component is,

$$k_{photon} = \frac{\omega}{c} n \cdot \sin\theta \quad (1.12)$$

From equations 1.11 and 1.12 we get the following relationship,

$$k_{photon} < k_{SPP} \quad (1.13)$$

As the frequency (energy) and the wave vector (momentum) must be conserved in the conversion of photons to SPPs and vice versa, this means that light incident onto the surface in this way cannot excite SPPs. Figure 1.6 shows that the dispersion relations

for light in air and SPPs at a metal/air interface do not overlap. The dispersion relation for light is linear but for SPPs the curve approaches $\omega_p\sqrt{1+n^2}$ for large k_{SPP} .

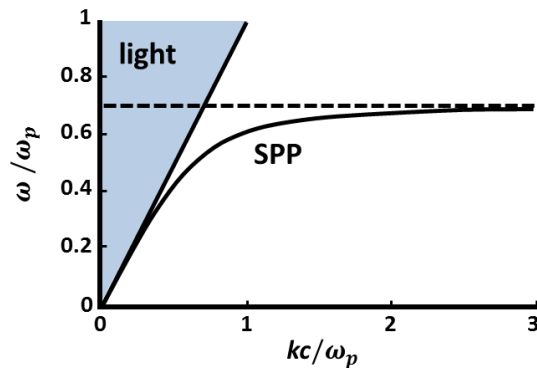


Figure 1.6: Dispersion relations for SPPs at a gold/air interface and light in air. The filled area is the possible angles of incidence of light, the dashed line indicates the frequency of the SPP as it approaches $\omega_p\sqrt{1+n^2}$ for large wave vectors.

1.2.2.6 Methods to excite SPPs

(i) Kretschmann Configuration

To excite SPPs the wave vector of the light has to be adjusted (increased) to match that of the wave vector of the SPP. One method, discovered by Kretschmann and Raether [34], is commonly used in commercial SPR devices. A glass prism with a high refractive index is used to reflect the light at the glass-metal interface by means of total internal reflection. It cannot excite SPPs at this interface (Figure 1.7 solid red trace), but for certain frequencies, if the metal layer is thin enough, the evanescent wave can couple to the other side of the metal layer and provide the momentum needed to match the wave vector of the SPPs on the metal-air (dielectric) interface. To excite the SPPs, k_{photon} must equal k_{SPP} which implies,

$$n_{prism} \cdot \sin(\theta) = \sqrt{\frac{\epsilon_m(\omega) \cdot n^2}{\epsilon_m(\omega) + n^2}} \quad (1.14)$$

This equation can be solved by tuning either the frequency/wavelength or the angle of incidence. The darker shaded area in Figure 1.7 shows the region where solutions lie.

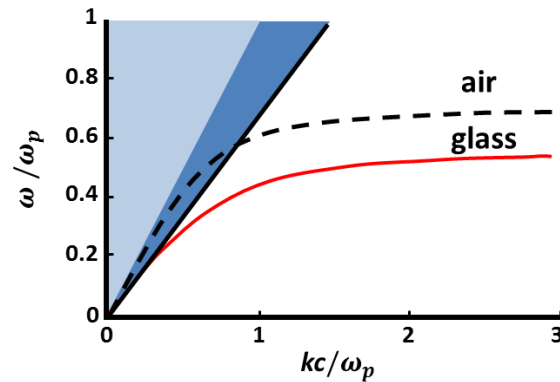


Figure 1.7: Dashed trace shows dispersion relations for SPPs at a gold/air interface. Solid red trace is for gold/glass. Straight line is the dispersion of light in glass and the darker shaded area represents the angles of incidence that will excite SPPs on the gold/air interface.

When light is coupled to the SPPs some of the lights parameters such as amplitude, phase and polarisation can be altered. Equation 1.14 shows that changes in the dielectric medium near the air-metal interface will change the resonance condition. Hence, a change in refractive index (RI), due to molecular binding for example, will produce a change in the light being emitted from the prism. The measurement of the reflected light is used to track RI changes in many commercial SPR systems, such as Sierra Sensors SPR-2 [35]. Figure 1.8(a) shows a schematic of the Kretschman configuration and how it is used for sensing. The angular scan seen in Figure 1.8(b) shows the intensity vs the excitation angle (θ). As the refractive index on the gold surface is changed, the location of the dip in intensity changes (from the black line to the yellow line). Figure 1.8(c) shows this change over time so that the binding event can be monitored in real time.

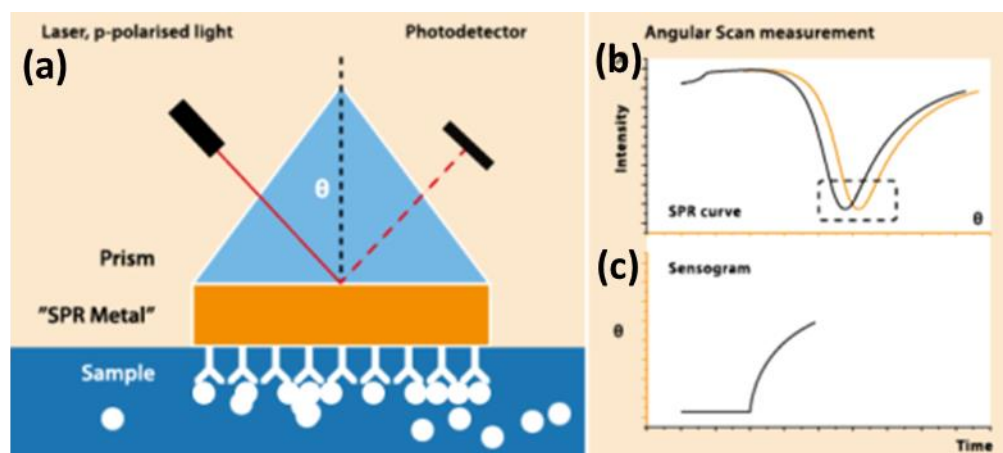


Figure 1.8: (a) Kretschmann configuration illustrating how SPPs are excited on a gold surface and how the reflected light is altered by biomolecular binding. (b) angular scan of the intensity vs excitation (θ) for both a blank surface (black) and a modified surface (yellow). (c) shows the sensogram for this binding event [36].

(ii) Nanohole array

Another approach to excite SPPs optically on a metal-dielectric interface is to use a grating (periodic structure). When light is incident on a grating, the light is scattered and diffracted. The surface component of this light gets additional ‘momentum’ from the periodic structure and increases the wave vector enough to excite the surface plasmon on the metal surface. This principle holds for both one and two dimensional gratings, such as periodic nanohole arrays. If a nanohole array is on flat metal film, it can support both SPPs and LSPs. As discussed previously an individual nanohole can sustain localised resonances and the metal film allows propagation of surface plasmons. The hole mediates a coupling between an incident electromagnetic wave and plasmons in the metal film [27].

As shown in Figure 1.9, this additional wave vector shifts the dispersion line of the incident light to the dispersion line of the diffracted photon. This light line crosses the dispersion curve of the surface plasmon. This crossing means that the incident light couples with the surface plasmon on the metal grating surface.

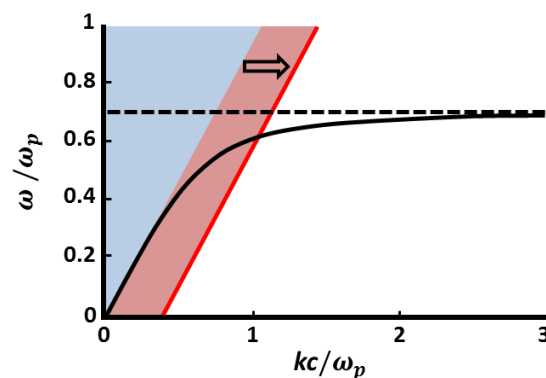


Figure 1.9: Dispersion relations for SPPs at a gold/air interface. The additional wave vector due to the grating shifts the dispersion line (red line) meaning the light can couple with the SPPs on the metal surface.

The additional momentum provided by the scattered light can be described with the components $\mathbf{i}k_x$ and $\mathbf{j}k_y$, where x and y denote the hole orientation and \mathbf{i} and \mathbf{j} are vectors along the coordinate axis. The phase matching condition for exciting SPPs under the above conditions becomes [37],

$$k_{SPP} = |\mathbf{k}_{photon} \cdot \sin(\theta) + \mathbf{i}k_x + \mathbf{j}k_y| \quad (1.15)$$

The additional momentum provided by the grating makes it possible to excite SPPs even at a normal incidence i.e. $\theta = 0$. This gives,

$$k_{SPP} = |\mathbf{i}k_x + \mathbf{j}k_y| \quad (1.16)$$

As seen in equation 1.10,

$$k_{SPP} = \frac{\omega}{c} \sqrt{\frac{\epsilon_m(\omega) \cdot n^2}{\epsilon_m(\omega) + n^2}} = \frac{2\pi}{\lambda} \sqrt{\frac{\epsilon_m \epsilon_d}{\epsilon_m + \epsilon_d}} \quad (1.17)$$

Where $\omega/c = 2\pi/\lambda$ and $\epsilon_d = n^2$. Combining equations 1.16 and 1.17, and noting that for a square array $k_x = k_y = 2\pi/P$ (where P is the lattice constant) gives,

$$k_{SPP} = |(\mathbf{i} + \mathbf{j})| \frac{2\pi}{P} \Leftrightarrow \frac{2\pi}{\lambda} \sqrt{\frac{\epsilon_m \epsilon_d}{\epsilon_m + \epsilon_d}} = \sqrt{i^2 + j^2} \frac{2\pi}{P} \quad (1.18)$$

Re-arranging this equation and solving for λ_{SPP} (the wavelength for the transmission peak) gives,

$$\lambda_{SPP} = \frac{P}{\sqrt{i^2 + j^2}} \sqrt{\frac{\epsilon_m \epsilon_d}{\epsilon_m + \epsilon_d}} \quad (1.19)$$

This equation gives a good first approximation [38] for the transmission peak at normal incidence for light interacting with a periodic array of nanoholes. It is the equation that is used to predict where the peaks in the transmission spectrum will occur in nanohole arrays. As λ_{SPP} depends on the period of the holes, the spectral peak position can be tailored. Also, a change in the dielectric causes a change in the transmission peak. It is this property that is exploited for sensing applications and will be discussed in detail in Sections 1.2 and 1.3.

1.3 Plasmonic array of nanoholes

As introduced in the previous section, the interaction of light with thin nanopatterned metal films has become an exciting area of study. The discovery of Enhanced Optical Transmission (EOT) through these films [39] led to this new field of research, as the optical properties of these structures differ from the classical electromagnetic theory. The understanding from the classical aperture theory is that when light falls on a subwavelength aperture, it is diffracted in all directions evenly with minimal transmission [40]. However, in EOT, the periodic structures enable a much higher transmission efficiency to occur, several orders of magnitude greater than expected. The phenomenon is mediated by plasmons (both SPPs and LSPs), that are excited when light is transmitted through a nanohole array.

1.3.1 Optical properties

There are many factors that influence the transmission spectrum of light passing through a nanohole array. The transmission spectrum is an interplay of the following factors,

- SPPs
- LSPs
- Rayleigh woods anomalies
- Direct transmission through a thin film and through the nanohole
- Angle of the incident light
- Polarisation

Furthermore, all of these effects will vary based on the metal and geometry of the nanohole array. These include the spacing between holes (pitch), the size and shape of the holes, the size of the array, the thickness of the metal film and of course the dielectric medium on each side of the metal, some of which are shown in Figure 1.10.

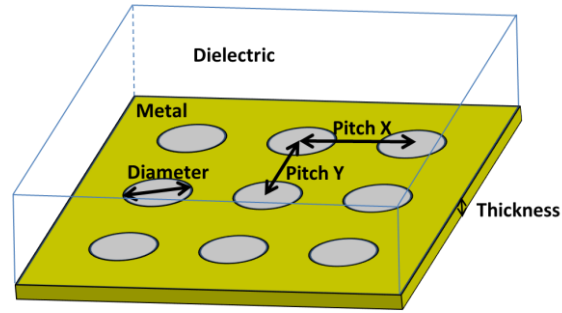


Figure 1.10: Schematic of a section of a nanohole array showing the pitch, hole diameter and film thickness

(i) *Transmission through bulk gold*

Light impinging on a thin gold film can be absorbed by electrons from the uppermost ‘d’ band which are then promoted to the ‘sp’ conduction band. These electrons then come back to their initial state by releasing a photon. For gold, this radiative interband transition occurs around 520nm [41]. This explains why thin gold films appear green in transmission.

(ii) *Direct transmission through the nanoholes*

Light impinging on a nanohole array can also be transmitted directly through the nanohole. Hans Bethe found that (at first approximation) the normalised to area transmission through a circular hole perforating a conductor is [40],

$$T \approx \frac{64}{27\pi^2} \left(\frac{r}{\lambda}\right)^4 \quad (1.20)$$

Where r is the radius of the hole and λ the wavelength of the incident light. This is extremely inefficient for holes of small diameter for light in the visible range. For example, the normalised transmission of light at 600 nm through a 120 nm hole is 2.4×10^{-5} .

(iii) *SPPs*

When both sides of the metal structure have the same periodic structures (i.e. nanoholes), the surface plasmon modes on both sides couple, and energy is transferred from the input side (the incident light) to the other side. This is a tunnelling process through the sub-wavelength holes (depicted in Figure 1.11) and the intensity of the transmitted light decreases as the film thickness increases [42], due to the exponential decay of plasmons. As shown in equation 1.19, the transmission peak (λ_{SPP}) that is due

to the SPPs propagating between the nanoholes, can be calculated. The periodicity and the dielectrics of both the metal and the dielectric are the only factors that influence this equation. The most common way to tune the transmission spectrum of an array is to alter the period of the nanoholes.

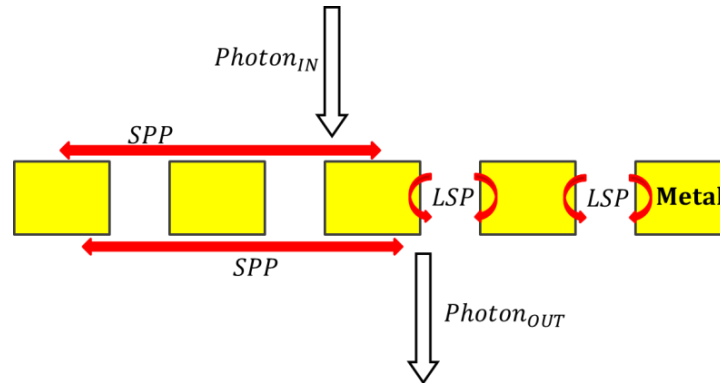


Figure 1.11: Schematic of the transmission mechanism in a nanohole array. The surface plasmon is excited by the incident photon and coupled by the holes to the other side of the metal. The photon is emitted from the surface plasmon on the back surface.

(iv) *LSPs*

The LSPs that are present around the edges of each nanohole also contribute to the enhanced transmission [43]. By changing the size or shape of the nanoholes, the frequencies of the LSPs are also changed. For example, when the diameter of the nanoholes is increased, the wavelength of the LSP is also increased. A red shift in the transmission spectra is observed [44]. Similarly, when the height of the nanoholes is changed (i.e. the film thickness) the peak position blue-shifts as the thickness (hole depth) is increased (~ 10 nm/nm [45]). It is this factor that alters the transmission spectrum when just the hole shape/size is changed, and all other factors remain constant.

(v) *Rayleigh woods anomalies*

Rayleigh anomalies (RAs), also referred to as Wood anomalies are sometimes evident in the transmission spectrum. For normal incident light, the wavelength at which the Raleigh anomaly occurs is,

$$\lambda_{RA} = \frac{P}{\sqrt{i^2 + j^2}} \sqrt{\epsilon} \quad (1.21)$$

They can play an important role in the shape the spectral peaks [46]. The RA represents light being diffracted parallel to the metal surface [47]. At the RA wavelength the intensity of the transmission is greatly reduced (almost to zero).

(vi) Angle of incident light

It has been reported that spectra from EOT can be affected by the angle of the incident light [39, 48]. Even with small changes in angle, the transmission spectra changes, with peaks changing in intensity and even moving and splitting. This is because as the incident angle is changed different SPP modes are excited [49].

A benefit of changing the angle of incidence is that it is possible to decrease the direct transmission (of background) light, leading to a greater signal to noise ratio [50], as the direction of the EOT is perpendicular to the nanohole array and the directly transmitted light follows the angle of the incident light. The equations in Section 1.2.2.6 only deal with the transmission, where the light is normal to the surface and the effects of the angle of incidence are beyond the scope of this thesis and hard to implement.

(vii) Polarisation

(a) Nanohole Shape

The shape anisotropy of elliptical or rectangular nanoholes induces polarisation sensitive transmission spectra in both individual nanoholes and nanohole arrays [28, 51-54]. Very recently, it was shown that this polarisation could be used to tune the optical response in the visible spectral region when using arrays of crossed shaped nanoantennas, and that these devices had potential as encrypted tags for security application [55]. In elliptical nanoholes, a very strong spectral anisotropy is observed for spectra acquired using polarised excitation light along both the short and long axis of the ellipses, showing distinct features, such as sharp peaks and spectral minima, in the 600-1200 nm regions. Simulations suggest that the observed peaks were related to Fano resonances between the spectrally broad Localized Surface Plasmon (LSP) of the nanopore array and a sharp Rayleigh Anomaly (RA) on the Au/glass interface [53].

(b) Periodicity

As shown in Figure 1.10, the pitch of the nanohole array can be different in the x and y directions. When light is polarised along the x axis the SPPs are excited at that

periodicity and the same for the y axis. This results in two very different transmission spectra.

(viii) *Fano Resonance*

Although the peaks and troughs in the transmission spectrum through a nanohole array can be assigned to the SPPs, LSPs, RAs and how they interact there are important characteristics of the actual spectrum (such as red shifted resonances and asymmetric peaks [56]) that cannot be addressed using the above theory. It is put forward [57] that Fano resonance accounts for some of these characteristics. Fano resonances are encountered in various fields of physics and describe interference of two transmission pathways, one resonant and another one non-resonant. Depending on the relative phase and amplitude of these two pathways different line shapes occur, see Figure 1.12, parameterized by a constant q called the asymmetry parameter. q describes the ratio of probability of taking the first over the second path.

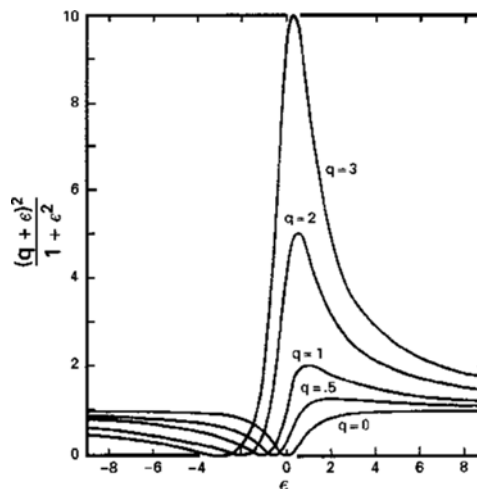


Figure 1.12: Spectral profiles of Fano Resonance with different values of q [58].

In the case of nanohole arrays, it identifies two interfering contributions to the transmission process, a resonant contribution from the SPP excitation and a non-resonant contribution from the scattering of light from the periodic structure. The total transmission is then decided from the interference of the two contributions. Near the resonant energy, the background scattering amplitude typically varies slowly with energy while the resonant scattering amplitude changes both in magnitude and phase quickly. It is this variation that creates the asymmetric profile.

1.3.2 Simulations

In theory the optical behaviour of metallic nanostructures is determined by Maxwell's equations. These can only be solved analytically for simple geometries like spherical particles, flat films or simple SPP waveguides [59]. For more complicated geometries however, the equations can only be solved numerically. The most commonly method used is finite-difference time-domain (FDTD) algorithms [60], which calculate the distribution and propagation of electromagnetic fields through materials with any geometry, with direct solutions to Maxwell's equations. The electric and magnetic fields are solved at a given instant in time, and then at the next instant in time. This is repeated over and over again until steady state behaviour is reached.

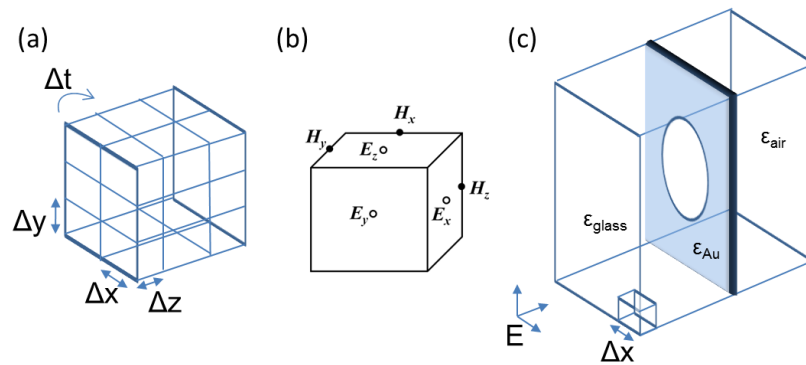


Figure 1.13(a) example of a simple grid, (b) the Yee-cell, (c) defined structure; one nanohole in a metal film with glass on one side and air on the other.

The computational domain of the simulation must be discrete and is defined by a mesh structure. Uniform grids are often used (as shown in Figure 1.13(a)) to define the structure in step sizes of Δx , Δy and Δz . Care must be taken to ensure the structure is well defined by the grid and for plasmonic applications the grid must also resolve the wavelength of light and SPP. There is a trade-off between the grid size and the time the simulation requires to run. Non-uniform grids can be used to help balance the simulation accuracy and efficiency by having many grid points around the smallest structures and less elsewhere.

The Yee-cell [61] (Figure 1.13(b)) is often used as the unit cell of the grid. The vector components of the E-field and H-field are spatially staggered about the rectangular cell. Each H-field vector component is located midway between two E-field vector components and vice versa. Furthermore, a leapfrog method is used in time, where the

E-fields are calculated midway between successive H-field updates. This time stepping scheme avoids the need to solve simultaneous equations but requires a short step time.

For periodic structures, instead of defining the whole array of nanoholes, perfectly matched layers are often used [53, 62, 63] as the absorbing boundary conditions. Only one nanohole and the surrounding metal and dielectrics is defined and the x and y directions are setup as being identical to give an infinite array of nanoholes. Even with this setup the FDTD algorithm is very computationally intensive but it is suitable for parallel computation, on multiple cores, multiprocessors and clusters.

1.3.3 Fabrication of nanoplasmonic structures

Fabrication of nanostructures can be broken down into two main methods; top down and bottom up approaches. The top down approach to fabrication involves patterning techniques (such as lithography) to build the structures in place, whereas bottom-up, or self-assembly, approaches to nanofabrication, use chemical or physical forces operating at the nanoscale to assemble basic units into larger structures.

1.3.3.1 Top down approaches

Top down approaches are generally used to make ordered arrays. There are a range of fabrication methods that can be used to make arrays of nanoholes in metal. These include Electron Beam Lithography (E-beam) [64], Focused Ion Beam (FIB) lithography [65], nanoimprint lithography [66], phase shift lithography [67], interference lithography [68] and template stripping [69]. There are pros and cons to each of these methods and this section will cover some of these methods.

(i) Focused Ion Beam

FIB lithography is a direct-write, maskless, high-resolution nanofabrication tool commonly used to fabricate nanohole arrays [70, 71], shown in Figure 1.14. A beam of low energy ions (typically gallium) is used to mill the surface. As the ions bombard the surface they remove the metal ions with about 1 to 5 atoms removed for each ion depending on the substrate and ion energies [59]. The diameter and the current of the

ion beam can be finely tuned allowing various depths, sizes and shapes of the nanoholes. The resolution is $\sim 10\text{nm}$. FIB is extremely useful for rapid prototyping but not suitable for mass production.

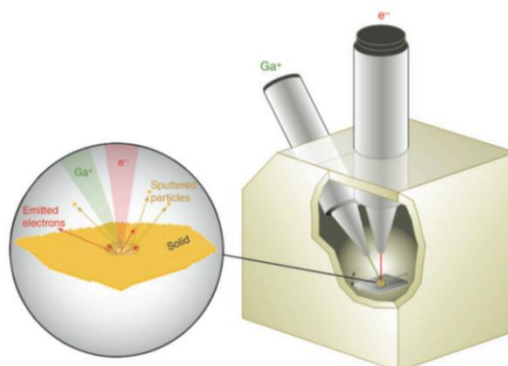


Figure 1.14: Schematic of a dual-beam FIB-SEM instrument. Expanded view shows the ion beam sample interaction [72].

(ii) Electron Beam Lithography

In e-beam lithography, a focused beam of electrons is used to pattern shapes onto a resist. The electrons interact with the resist, depicted in Figure 1.15, changing the solubility to allow selective removal by etching of either the exposed or non-exposed regions [70]. The remaining resist is then used as a mask and the process is continued as in traditional lithography. A method to fabricate nanopores would be to expose the resist where the holes are, remove the unexposed resist to leave pillars of resist. Metal could then be deposited and finally the remaining resist etched away to leave a thin metal film with nanoholes. The main advantage to e-beam is the sub-10nm resolution and the ability to write any type of shape [73]. It is however slow to use (serial writing) and quite expensive.

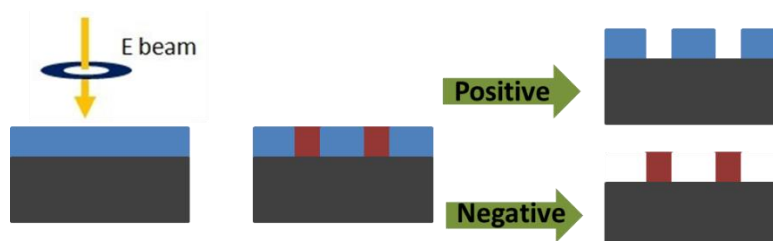


Figure 1.15: Schematic representation of the E-beam process. Resist is patterned, then depending on the resist type the exposed/non-exposed regions are removed.

(iii) Nanoimprint lithography

Nanoimprint lithography creates patterns by mechanical deformation of an imprint resist and this is subsequently processed [74]. A negative mold of the nanostructures (often PDMS) is brought in contact with the resist (a photo (UV) curable liquid) and the resist is cured under UV light [73] (procedure shown in Figure 1.16). After separation the structured resist can be processed similarly to the example given for e-beam. The major advantages to the process are the large area and high uniformity that can be achieved for a relatively low cost. A drawback is the necessity to still use another process (such as e-beam) to make the initial structure the mold is fabricated from. Nanoimprint lithography uses costly procedures/equipment to create the molds, but the stamp can be repeatedly used [75].

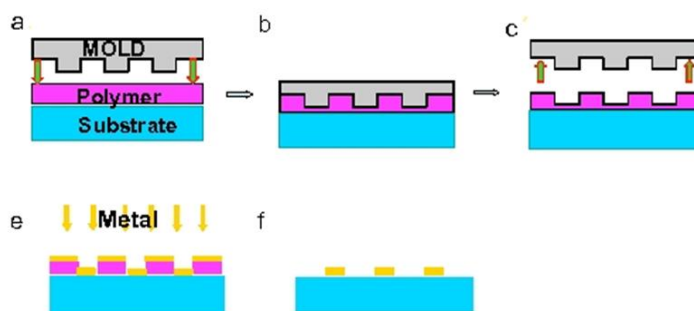


Figure 1.16: Illustration of the nanoimprint lithography process. The glass substrate is coated with a polymer and printed with the mold (a-c). The mold is removed, metal is deposited and finally the remaining polymer is washed off [66].

(iv) Template Stripping

Template stripping from smooth unpatterned surfaces is a well-known technique [76]. It has recently been used to fabricate ultrasmooth nanohole arrays [77]. The method, shown in Figure 1.17, utilises a nanoimprint stamp, reactive ion etching and then the template stripping. A nanoimprint mold is used to pattern resist, reactive ion etching is used to generate deep nanoholes in the substrate and metal is deposited to form the nanohole array. The metal is attached to glass using an epoxy and peeled from the substrate. The resulting surface then has a similar roughness to that of the original substrate and of high optical quality for plasmonic sensing [78]. Similar to nanoimprint lithography a high cost template is needed for the initial mold.

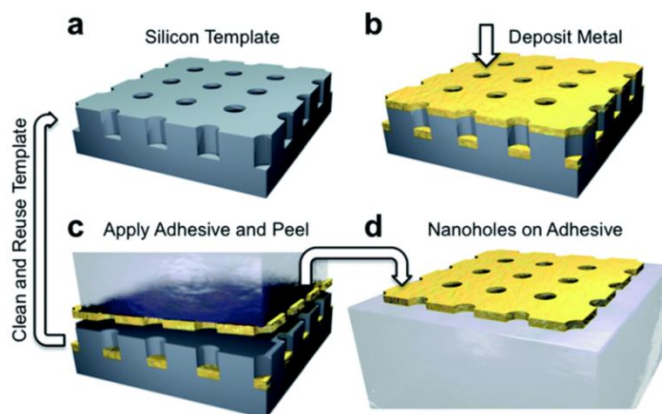


Figure 1.17: Schematic of the template stripping process. Metal is deposited onto a silicon template (b), an adhesive backing layer is used to peel the metal layer from the template (c) to leave the nanohole array (d) [69].

(v) *Interference Lithography*

Interference lithography (IL) consists of exposing a photosensitive material to a fringe pattern generated by the interference of two plane waves. Upon post exposure processing the pattern corresponding to the periodic intensity pattern emerges in the photoresist. To achieve pillars of resist two exposure process are used, rotating the sample 90° between the exposures [68]. Thus, only periodic patterns can be recorded. This is a cost effective, high throughput method of making large arrays of nanopores, shown in Figure 1.18. However, it was found that the plasmonic peaks were not as well defined at lower wavelengths as those made using FIB [79].

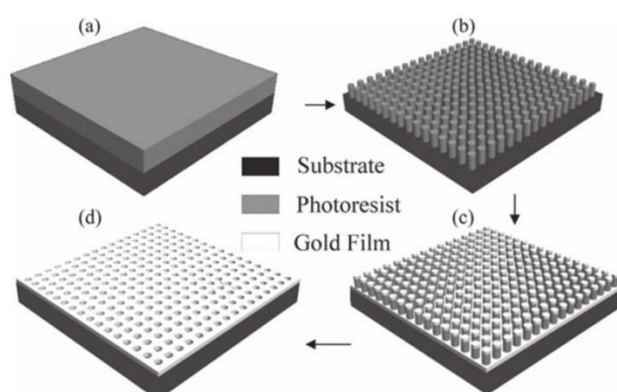


Figure 1.18: Fabrication using interference lithography. (a) photoresist coated on substrate, (b) IL patterned photoresist, (c) photoresist coated with gold, (d) Au film after photoresist lift-off [68].

(vi) Phase shift lithography

Phase shifting photolithography (PSP) is an edge photolithography technique that produces narrow features in the photoresist at the edges of the patterns in a PDMS mask [80]. Destructive interference patterns caused by the mask cause the regions at the edges of the structure to be non-exposed, leaving structures of 30-50 nm in size as shown in Figure 1.19. After development these areas remain. Similarly to IL, two exposures carried out with a 90° rotation between them can be used to create pillars of resist.

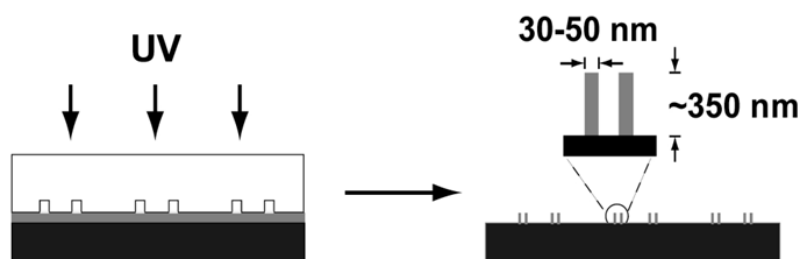


Figure 1.19: PSP schematic. A PDMS mask with features down to 100nm is used to expose the photoresist to UV light. The resulting features are in the order of 30-50 nm [67].

There are pros and cons to each method of fabrication. In general, the methods that give large areas require an expensive mask/master, the parameters of which cannot be changed, requiring the fabrication of a new mask/master, if refinements are required. With FIB and E-beam lithography, the design can easily be changed, but they are only suitable for smaller areas. In current work, FIB was chosen due to its suitability for rapid prototyping and its relatively low cost.

1.3.3.2 Self-assembly methods

Self-organizing functional systems and devices are the ultimate aim of bottom-up fabrication. Bottom-up nanofabrication approaches are related to the construction of materials and devices by the self-assembly of particles or molecules. This methodology has the potential of generating functional multi-component devices by the controlled assembly of atoms and molecules [81]. Some of the most prominent self-assembly approaches are described in this section.

(i) Langmuir–Blodgett

The Langmuir–Blodgett technique is commonly used to self-assemble nanorods and nanoparticles. As shown in Figure 1.20, a monolayer is formed at the surface of the liquid. There is electrostatic attraction between the molecules in the monolayer and this is sufficient to prevent the monolayer from falling apart during the transfer process. A solid film is immersed into the solution of the nanoparticles and a monolayer is adsorbed with each immersion or emersion step. Arrays of nanowires can be aligned in this way, with the pitch, nanowire orientation, array size, array orientation, and array pitch controlled independently for sequential depositions [82].

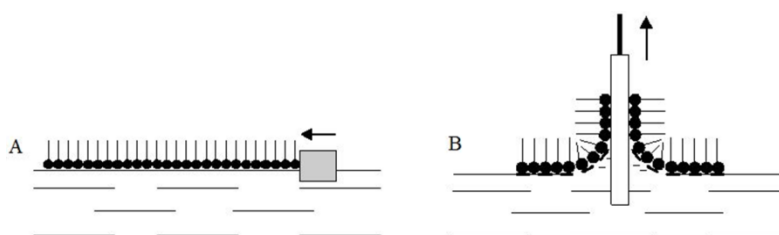


Figure 1.20: A monolayer of nanoparticles is aligned onto a substrate using the Langmuir–Blodgett technique [83]

(ii) Drop evaporation

Another method to create self-assembled monolayers of nanoparticles is the drop evaporation method. A solution of the nanoparticles is left to evaporate under controlled conditions, and as it does the particles are deposited in an ordered manner [84], as shown in Figure 1.21. The ordering of particles can be tuned by altering the droplet surface tension, particle concentration, and the size and shape of the particles [85]. During the evaporation process, forces such as capillary flow align the particles before they are deposited, when the solvent evaporates from the edges.

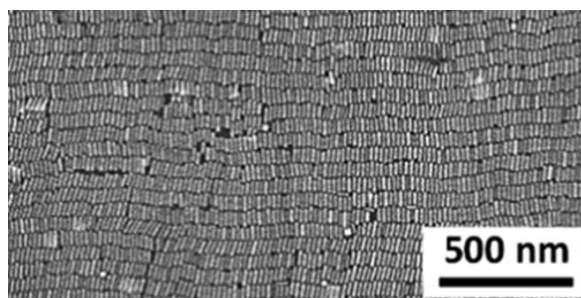


Figure 1.21: SEM image of gold nanorods (with dimensions of 12 nm x 45 nm) aligned by droplet evaporation [86].

(iii) Nanosphere lithography

Disordered or ordered nanohole arrays can be fabricated using nanosphere lithography [87]. Polystyrene (PS) beads are arranged on the surface, by spin coating or drop coating to form a hexagonal pattern. They are then etched and used as a mask for a lithography step to make nanoholes or nanopillars [88]. Figure 1.22 shows the process used to fabricate a nanohole array in a gold film using this technique.

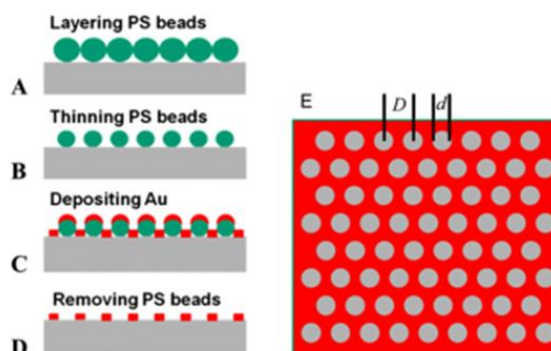


Figure 1.22: Outline of the process for fabricating Au nanostructures using polystyrene beads. (A–D) Side views of the steps for fabricating the Au nanoholes. (E) A top view of the final Au nanostructures [89].

(iv) Electric/Magnetic fields

Electric and magnetic fields are also used to align nanoparticles. Electric-field assisted assembly technique can be used to position individual nanowires suspended in a dielectric medium between two electrodes. During the assembly process, the forces that induce alignment are a result of nanowire polarisation in the applied alternating electric field [90]. Figure 1.23 shows aligned nanowires between electrodes. The application of external electric fields leads to great control over the alignment direction over micron size areas of oriented nanoparticle arrays [91, 92].

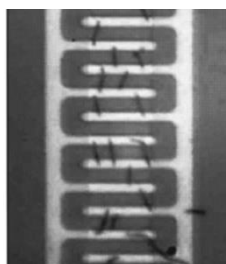


Figure 1.23: Image of 5 mm long, 200-nm-diameter Au nanowires aligned by applying a voltage to the structure [90].

1.4 Nanohole arrays: applications to biosensing

A sensor is a device that is used to monitor and provide information on a physical quantity. Biosensors are a subgroup that provide information on biological processes, often interactions between biomolecules. They can be used to measure the concentration of a target biomolecule, and increased or lowered levels of specific biomolecules characterise many diseases [93-95]. Biosensors are widely used in hospitals, but there are currently very few that can be used outside of the laboratory setting. This is due to the complexity, size and/or cost of the current techniques. There are a few point of care biosensors presently on the market, such as pregnancy tests and blood glucose sensors, and there is a lot of effort being expended to make similar sensors to measure other conditions [96-99].

1.4.1 Applications

(i) *The Immune system*

The human defence system is a complex system, which includes many components. Each part plays a role in defending the body against foreign pathogens. In general, the human immune system can be divided into two parts; a) the innate immune system, which a human is born with; and b) the adaptive or acquired immune system, which develops over a lifespan. The main role of the innate immune system is to attach non-specifically and engulf foreign bodies to dispose of them *via* phagocytosis [100].

White blood cells that are part of the adaptive immune system are referred to as lymphocytes and are composed of T- and B cells. T cells have several subsets, amongst which is the T- helper cell, which present surface antigen to macrophages [100]. B cells are memory cells and will produce antigen specific antibodies, when exposed to a certain pathogen. When stimulated, B cells are turned into plasma cells, which will produce antibodies specific to a certain site on a pathogen. This results in natural immunity against certain diseases, once exposed, and lends itself to the practice of vaccinations [101].

(ii) *Antibodies*

Antibodies are proteins that are produced by B- plasma cells in response to foreign pathogens entering the human system. Antibodies, or immunoglobulin, come in five subclasses (M, A, D, G and E), with Immunoglobulin G (or IgG) being the most

prolific. Antibody production is stimulated by a specific antigenic presence, and very specific to a certain target site on the pathogen (a bacteria, virus, etc.). The general role of the antibody is to tag the foreign object for disposal by macrophages [100]. The specificity of antibody/antigen interactions makes it a perfect candidate for diagnostic assays in relation to diseases. An antibody has a 'Y' shape as shown in Figure 1.24 with two distinct regions.

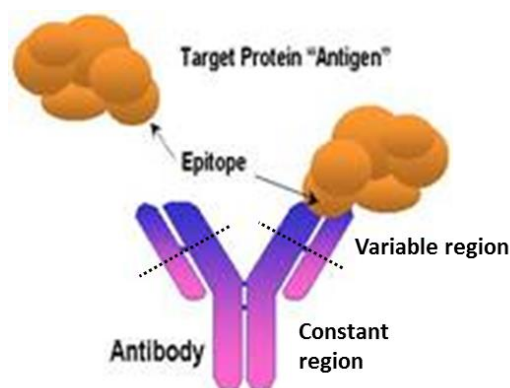


Figure 1.24: Schematic of an antibody and antigen. The constant and variable regions of the antibody are shown.

It consists of two distinct regions; the Fc region, or constant region, which is the same in all antibody classes; and the Fab region, or variable region, which differs between the five antibody subclasses. Within the variable region lies the hypervariable region, which is unique to each antibody produced, and generated by a specific antigenic stimulus. The whole antibody is used in the work presented in chapter 2 of this thesis.

(iii) Single chain variable fragment

A single-chain variable fragment (scFv) is a fusion protein of the variable regions of the heavy and light chains of immunoglobulins, connected with a short linker peptide of ten to about 25 amino acids. The scFv can be produced by generating them recombinantly in mammalian cell lines, or more often in bacterial cultures, such as *E.coli*. The advantages of using scFv for research and diagnosis include greater availability of binding sites, due to the smaller size compared to a full antibody, as more molecules are available per unit area; directionality, as steric hindrance is much less of a problem; and Antibody fragments that are without the Fc region have the advantage of reduced non-specific binding [102]. These scFv are used in the work presented in chapter 3.

(iv) Antigen

Antigens are proteins that, when introduced into a human body, elicits a specific response from a normal functioning immune system. They serve as target for antibodies. They are found on the surface of pathogens, like bacteria or viruses, and are usually specific sequences of proteins or polysaccharides. B-plasma cells will produce antibodies to a certain antigen, once exposed to it. Immunity in a healthy human after exposure would generally be lifelong.

In general, every foreign pathogen will induce a specific response in the immune system. By measuring the quantity and type of antibodies or antigens present in the blood, urine or saliva, it is possible to get a medical diagnosis for the cause of the symptoms a patient has. A biosensor will interact specifically with the target analyte and the result of the biochemical reaction is transformed through a transducer to a measurable signal.

1.4.2 Existing Biosensing Technologies

Current biosensing technologies can be classified in two categories, labelled or label-free. Although labelled technologies such as ELISA [103], Fluorescence [104] and Western blotting [105] are currently the most widely used there is a push towards label-free technologies due to the potential benefits they offer, such as real time monitoring of binding, time to run, cost and ease of use [106-109]. For these reasons surface plasmon resonance technologies have already captured a significant portion of this market [110].

(i) ELISA

ELISA stands for Enzyme Linked Immunosorbent Assay and is one of the most widely used immunoassay, due to its user friendly format and high throughput, particularly in a clinical environment. It is a method of antibody/antigen interaction detection, by coupling either the antigen or the antibody to a well plate. The corresponding antibody (or antigen, depending on the coating of the well) will give a readable output of the antibody/antigen interaction that may be semi quantitative data. The final detection of the interaction may be completed by a variety of techniques, but most commonly ELISA assays are chromogenic. A typical ELISA (Sandwich format) assay is shown in Figure 1.25. A plate is treated with a solution of antibodies, the sample is added and the antigen binds to the capture antibodies. The detection antibody is added and enzyme

linked secondary antibody is bound to the detecting antibody. The substrate is added and the signal produced by the enzyme substrate reaction is measured.

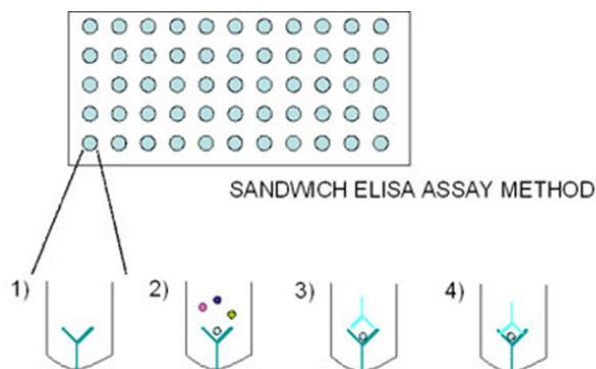


Figure 1.25: ELISA assay. 1) Capture antibody on plate. 2) Sample added. Antigen binds to capture antibody. 3) Detection antibody added. 4) Enzyme-linked secondary antibody added and binds to detecting antibody. 5) Substrate is converted by enzyme to detectable form (light/colour)

ELISA is one of the most established laboratory technique but there are a number of key disadvantages to ELISA: the need to label individual antibodies or antigens, depending on format, expensive in cost and complexity, requirement for trained personnel and long assay times (3-5 hours).

(ii) Fluorescence

Fluorescence detection is one of the most sensitive detection methods, with the reported detection limit down to a single molecule [111]. Most commonly, the assay platform is a well plate or an array. The fluorophore tag is a dye that is excited at a specific shorter wavelength and emits at a certain longer wavelength. The tag can be conjugated to either the antibody or the antigen, depending on the assay format. A successful antibody/antigen binding event would result in a fluorescent response, and can give both qualitative and quantitative information about the assay.

The drawbacks of fluorescence detection are: that there may be background noise from the natural fluorescence of some proteins; as well as photobleaching of the fluorophore when exposed to light, which reduces the signal. These factors, in addition to the long detection time (~4 hours) and the necessity of trained personnel, make it unsuitable for point of care applications.

(iii) *Western blotting*

Western blotting is a technique that involves the transfer of biological samples from a gel to a membrane and their subsequent detection on the surface of the membrane. The detection of the protein in question is done by an antibody *via* antibody/antigen interaction. The specificity of the antibody/antigen interaction enables a target protein to be identified in the midst of a complex protein mixture. Western blotting can produce qualitative and semiquantitative data about the protein in question.

The main drawbacks of Western blotting are that the technique requires highly trained personnel, it is time consuming compared to most other techniques (running time on the gel and subsequent incubation), as well as the requirement for optimisation of the experimental conditions (i.e. protein isolation, buffers, type of separation, gel concentration, etc.).

(iv) *QCM – quartz crystal microbalance*

Used for label free biosensing. Quartz is a piezoelectric material that deforms when an electric field is applied to it. At a certain frequency (the resonant frequency) the quartz oscillates with greater amplitude. This frequency depends on the thickness of the quartz crystal, and changes when mass is absorbed onto the crystal, as the effective thickness is changed, see Figure 1.26.

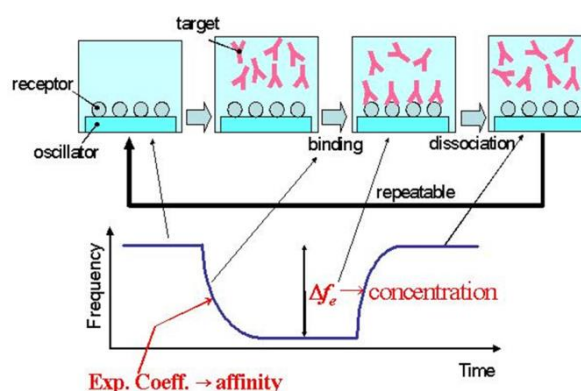


Figure 1.26: Schematic of a Quartz crystal microbalance used for sensing [112].

Major challenges include identification of low-abundant proteins and resolution of the dynamic range when dealing with proteins in varying pH and molecular weight extremes, low throughput, lack of effective immobilisation protocols, requirement for large active areas (up to 20 mm² for QCM), low sensitivity and limit of detection, e.g.

1–5 μM (label free) for DNA detection and poor potential for integration hindered widespread application and take-up of two approaches [113, 114].

(v) *Electrochemical*

Another label free detection method. The basic components of an electrochemical sensor are a working (or sensing) electrode, a counter electrode and usually a reference electrode as well. The working electrode is where the electrochemical reaction takes place and is the interface to the solution. The reference electrode provides a well defined potential to compare the working electrode to. The counter electrode acts as a supply or sink of electrons. The current measured at the working electrode will change depending on the charge at the solution interface. This can be used to tell if there are certain ions/antibodies/antigens in the solution, as shown in Figure 1.27.

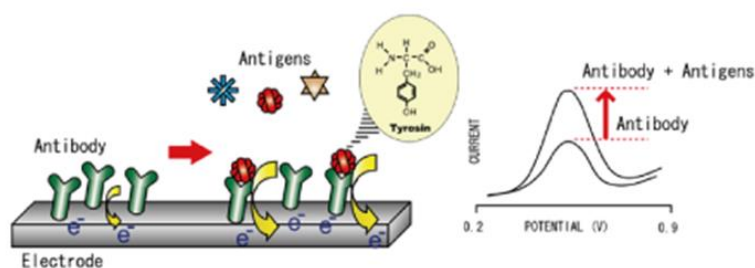


Figure 1.27: Label free electrochemical detection for sensing.

(i), (ii) and (iii) are all lab based techniques that require trained personnel and expensive equipment making them unsuitable for point of care diagnostics. Table 1.3 shows the current state of the art in biosensors.

Table 1.3: State of the art POC devices

System	Manufacturer	Industry	Benchtop	Test/hour	Analysis time	Sample Vol.	Targets
AIA-360	Tosoh Bio. Inc.	DIA	Yes	36	> 1 min	>200ul	Biomarkers
ABL90 FLEX	Radiometer America, Inc.	DIA	Yes	30+	> 1 min	>65ul	Biomarkers
SQiDman	SQI Diagnostics	DIA	Yes	200+	>30 sec	>200l	Biomarkers
IMMULITE 1000	SIEMENS	DIA	Yes	120	>30 sec	>200ul	Biomarkers
Triage MeterPro	Aleris	DIA	Yes	<10	15 min	>50ul	Biomarkers
Spotchem EZ	ARKRAY	DIA	Yes	60	8 min	>200ul	Biomarkers
BLItz	PALL Corp	LS	Yes	20	1 min	>100ul	Biomarker & protein
sam@x	Saw Instruments	LS	Yes	12	1 min	>200ul	Biomarker, protein & cell

DIA = Diagnostics, LS = Life Science

1.4.3 Kretchman vs Nanohole

SPR sensors using Kretchman configuration are the most widely used label-free optical biosensor [115]. Despite this, they suffer from several limitations which are due to the fundamental nature of surface plasmons. When detecting low concentrations or small targets, the molecules only occupy a fraction of the field that acts as the sensing probe. The resolution of the system is not sufficient to detect binding in these cases. Another disadvantage to the SPR sensor is the necessity to use a prism to couple the light onto the metal surface. The prism in addition to the optical components, microfluidics and other hardware make the device quite bulky. Despite being portable the size, weight and cost of the devices make them far from optimal for use as point of care devices. The sensing area for SPR is determined by the size of the illumination spot. This limits the minimum sensing area as the off axis excitation spreads the light.

A nanohole array used as a biosensor has the potential to overcome all of these limitations. Due to the LSPs at each hole which have very short decay lengths (10's of nm) they are more sensitive to smaller molecules or lower concentrations. The size can also be much smaller, both the sensing area and the entire platform. There is no prism needed and the required optics are much simpler. Instead of needing to align the light through the prism onto the sensor and align the reflected light onto the detector all that is needed is a light source (such as a LED), some microfluidics and a detector (photo detector or CCD) all in a straight line. This greatly reduces the complexity, size and cost. Arrays can also be placed very close to each other and they do not need to be very big (<20 μm in width [116]) showing the high promise for multiplex screening.

1.4.4 General challenges to point of care diagnostics

Point of care (POC) is the largest market for biosensors (over 40% of the total biosensor market in 2013) and it is predicted to dominate for the foreseeable future. A gradual shift is likely to be experienced from lab tests to in-line biosensors for new diagnostic tests to ensure real-time analysis. The market size for the global biosensors market is estimated to be over 21 billion USD in 2020, see Figure 1.28, with POC being approximately half of the market.

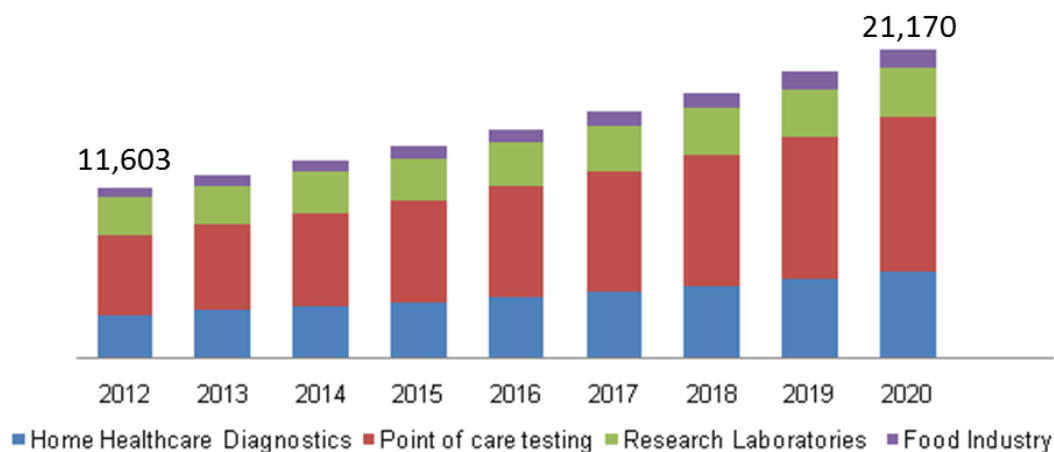


Figure 1.28: Global Biosensors Market, by End-use (USD Million) [117].

POC test devices must provide results that are as accurate and reliable as those obtained from laboratories while also demonstrating their cost-effectiveness to physicians and patients. A key element for the creation of a commercially successful point-of-care analysis system is simplicity. Simplicity in performing the analysis and in setting up/maintaining the equipment. A historic hurdle to the expansion of label-free analysis in routine testing has been both the real and perceived lack of simplicity. The complexity of label-free analysis is based on the traditional operational requirements of integrating a sensor element, a fluidic element, and a detector element, to perform an analysis. By design, sensors will vary slightly, so their calibration upon being interfaced with the detection unit will be a requirement. At the same time the sensor must also be interfaced with a sample delivery system, and this process introduces a variety of sensor handling and system maintenance issues. This has been achieved with devices such as blood glucose monitors for people with diabetes, and pregnancy tests which measure a hormone in urine or blood. At this time, there are no commercially available point-of-care systems that allow detection of disease protein biomarkers.

1.5 Scope of Thesis

The scope of this thesis is to explore the fabrication and characterisation of nanohole arrays in thin gold films and subsequently incorporate them into a benchtop setup for use as a label free real time biosensor.

In Chapter 2, the fabrication of the nanopore arrays using focused ion beam and a lift off technique is explored. Simulations (FDTD) are first carried out to design the array and view the theoretical electric fields and transmission spectrum of the arrays. The fabricated samples are then characterised and their suitability for use as a biosensor is confirmed by measuring the transmission spectrum changes caused by small bulk refractive index changes (using salt solutions). The attachment chemistry necessary to attach the biomolecules to the gold surface is explored, first using planar gold surfaces and AFMs to confirm attachment before then performing a full bioassay on the nanohole arrays and measuring a shift in the transmission spectrum.

In Chapter 3, the challenges of integrating a nanopore array into a benchtop setup are explored. The optics are designed and implemented and the gold samples (developed in chapter 2) integrated into a microfluidic system. The software (LabVIEW) to monitor the assay in real time is developed to take the light illuminating a low cost CCD camera and extract the transmission spectra from multiple arrays concurrently. Finally, an assay using pancreatic biomarkers is developed and carried out, where detection of the antigen in diluted serum is observed.

In Chapter 4, the effects of anisotropic nanoholes are analysed using both simulations and fabricated samples. A very strong spectral anisotropy is observed for spectra acquired using polarised excitation light along both the short and long axis of the elliptical nanoholes showing distinct features, such as sharp peaks and spectral minima. A novel application of using these anisotropic arrays as anti-counterfeiting tags is explored.

Chapter 5 contains the summary and potential future work.

1.6 References

- [1] T. Lutz, C. Große, C. Dette, A. Kabakchiev, F. Schramm, M. Ruben, *et al.*, "Molecular orbital gates for plasmon excitation," *Nano letters*, vol. 13, pp. 2846-2850, 2013.
- [2] L. Pan, Y. Park, Y. Xiong, E. Ulin-Avila, Y. Wang, L. Zeng, *et al.*, "Maskless plasmonic lithography at 22 nm resolution," *Scientific reports*, vol. 1, 2011.
- [3] J. Vuckovic, M. Loncar, and A. Scherer, "Surface plasmon enhanced light-emitting diode," *Quantum Electronics, IEEE Journal of*, vol. 36, pp. 1131-1144, 2000.
- [4] D.-M. Yeh, C.-F. Huang, C.-Y. Chen, Y.-C. Lu, and C. Yang, "Localized surface plasmon-induced emission enhancement of a green light-emitting diode," *Nanotechnology*, vol. 19, p. 345201, 2008.
- [5] U. Guler, A. Boltasseva, and V. M. Shalaev, "Refractory Plasmonics," *Science*, vol. 344, pp. 263-264, 2014.
- [6] M. Ozaki, J.-i. Kato, and S. Kawata, "Surface-plasmon holography with white-light illumination," *Science*, vol. 332, pp. 218-220, 2011.
- [7] A. Alù and N. Engheta, "Multifrequency optical invisibility cloak with layered plasmonic shells," *Physical review letters*, vol. 100, p. 113901, 2008.
- [8] Y. B. Zheng, B. Kiraly, P. S. Weiss, and T. J. Huang, "Molecular plasmonics for biology and nanomedicine," *Nanomedicine*, vol. 7, pp. 751-770, 2012.
- [9] X. Huang and M. A. El-Sayed, "Plasmonic photo-thermal therapy (PPTT)," *Alexandria Journal of Medicine*, vol. 47, pp. 1-9, 2011.
- [10] J. N. Anker, W. P. Hall, O. Lyandres, N. C. Shah, J. Zhao, and R. P. Van Duyne, "Biosensing with plasmonic nanosensors," *Nature materials*, vol. 7, pp. 442-453, 2008.
- [11] A. G. Brolo, "Plasmonics for future biosensors," *Nature Photonics*, vol. 6, pp. 709-713, 2012.
- [12] S. A. Maier, *Plasmonics: Fundamentals and Applications: Fundamentals and Applications*: Springer, 2007.

- [13] S. Linden, C. Enkrich, M. Wegener, J. Zhou, T. Koschny, and C. M. Soukoulis, "Magnetic response of metamaterials at 100 terahertz," *Science*, vol. 306, pp. 1351-1353, 2004.
- [14] K.-S. Lee and M. A. El-Sayed, "Gold and silver nanoparticles in sensing and imaging: sensitivity of plasmon response to size, shape, and metal composition," *The Journal of Physical Chemistry B*, vol. 110, pp. 19220-19225, 2006.
- [15] P. R. West, S. Ishii, G. V. Naik, N. K. Emani, V. M. Shalaev, and A. Boltasseva, "Searching for better plasmonic materials," *Laser & Photonics Reviews*, vol. 4, pp. 795-808, 2010.
- [16] R. Ritchie, "Plasma losses by fast electrons in thin films," *Physical Review*, vol. 106, p. 874, 1957.
- [17] E. Petryayeva and U. J. Krull, "Localized surface plasmon resonance: nanostructures, bioassays and biosensing—a review," *Analytica chimica acta*, vol. 706, pp. 8-24, 2011.
- [18] X. Liu, M. Atwater, J. Wang, and Q. Huo, "Extinction coefficient of gold nanoparticles with different sizes and different capping ligands," *Colloids and Surfaces B: Biointerfaces*, vol. 58, pp. 3-7, 2007.
- [19] M. Van Dijk, A. Tchegotareva, M. Orrit, M. Lippitz, S. Berciaud, D. Lasne, *et al.*, "Absorption and scattering microscopy of single metal nanoparticles," *Physical Chemistry Chemical Physics*, vol. 8, pp. 3486-3495, 2006.
- [20] A. Biswas, T. Wang, and A. S. Biris, "Single metal nanoparticle spectroscopy: optical characterization of individual nanosystems for biomedical applications," *Nanoscale*, vol. 2, pp. 1560-1572, 2010.
- [21] G. Mie, "Contributions to the optics of turbid media, particularly of colloidal metal solutions," *Contributions to the optics of turbid media, particularly of colloidal metal solutions Transl. into ENGLISH from Ann. Phys.(Leipzig)*, v. 25, no. 3, 1908 p 377-445, vol. 1, pp. 377-445, 1976.

- [22] P. Englebienne, "Use of colloidal gold surface plasmon resonance peak shift to infer affinity constants from the interactions between protein antigens and antibodies specific for single or multiple epitopes," *Analyst*, vol. 123, pp. 1599-1603, 1998.
- [23] S. Enoch, R. Quidant, and G. Badenes, "Optical sensing based on plasmon coupling in nanoparticle arrays," *Optics express*, vol. 12, pp. 3422-3427, 2004.
- [24] M. Piliarik, H. Šípová, P. Kvasnička, N. Galler, J. R. Krenn, and J. Homola, "High-resolution biosensor based on localized surface plasmons," *Optics express*, vol. 20, pp. 672-680, 2012.
- [25] T. Endo, S. Yamamura, N. Nagatani, Y. Morita, Y. Takamura, and E. Tamiya, "Localized surface plasmon resonance based optical biosensor using surface modified nanoparticle layer for label-free monitoring of antigen–antibody reaction," *Science and Technology of Advanced Materials*, vol. 6, pp. 491-500, 2005.
- [26] P. K. Jain, W. Huang, and M. A. El-Sayed, "On the universal scaling behavior of the distance decay of plasmon coupling in metal nanoparticle pairs: a plasmon ruler equation," *Nano Letters*, vol. 7, pp. 2080-2088, 2007.
- [27] T. Schneider, O. Stranik, N. Jahr, A. Csaki, and W. Fritzsche, "Nanoparticles and DNA on Chips–Realization of a Nanobiotechnology Toolbox for Single Particle Bioanalytics."
- [28] Y. Alaverdyan, J. Alegret, M. Káll, and P. Johansson, "Shape effects in the localized surface plasmon resonance of single nanoholes in thin metal films," *Optics express*, vol. 16, pp. 5609-5616, 2008.
- [29] T. Rindzevicius, Y. Alaverdyan, B. Sepulveda, T. Pakizeh, M. Käll, R. Hillenbrand, *et al.*, "Nanohole plasmons in optically thin gold films," *The Journal of Physical Chemistry C*, vol. 111, pp. 1207-1212, 2007.
- [30] A. Degiron, H. Lezec, N. Yamamoto, and T. Ebbesen, "Optical transmission properties of a single subwavelength aperture in a real metal," *Optics Communications*, vol. 239, pp. 61-66, 2004.

- [31] T. Rindzevicius, Y. Alaverdyan, A. Dahlin, F. Höök, D. S. Sutherland, and M. Käll, "Plasmonic sensing characteristics of single nanometric holes," *Nano letters*, vol. 5, pp. 2335-2339, 2005.
- [32] J. Homola, "Surface plasmon resonance sensors for detection of chemical and biological species," *Chemical reviews*, vol. 108, pp. 462-493, 2008.
- [33] A. V. Zayats, I. I. Smolyaninov, and A. A. Maradudin, "Nano-optics of surface plasmon polaritons," *Physics reports*, vol. 408, pp. 131-314, 2005.
- [34] E. Kretschmann and H. Raether, "Radiative decay of non radiative surface plasmons excited by light(Surface plasma waves excitation by light and decay into photons applied to nonradiative modes)," *Zeitschrift Fuer Naturforschung, Teil A*, vol. 23, p. 2135, 1968.
- [35] <http://www.sierrasensors.com/>.
- [36] <http://www.bionavis.com/technology/spr/>.
- [37] H. Gao, J. McMahon, M. Lee, J. Henzie, S. Gray, G. Schatz, *et al.*, "Rayleigh anomaly-surface plasmon polariton resonances in palladium and gold subwavelength hole arrays," *Optics express*, vol. 17, pp. 2334-2340, 2009.
- [38] A. Degiron and T. Ebbesen, "The role of localized surface plasmon modes in the enhanced transmission of periodic subwavelength apertures," *Journal of Optics A: Pure and Applied Optics*, vol. 7, p. S90, 2005.
- [39] T. W. Ebbesen, H. Lezec, H. Ghaemi, T. Thio, and P. Wolff, "Extraordinary optical transmission through sub-wavelength hole arrays," *Nature*, vol. 391, pp. 667-669, 1998.
- [40] H. Bethe, "Theory of diffraction by small holes," *Physical Review*, vol. 66, p. 163, 1944.
- [41] M. R. Beversluis, A. Bouhelier, and L. Novotny, "Continuum generation from single gold nanostructures through near-field mediated intraband transitions," *Physical Review B*, vol. 68, p. 115433, 2003.

- [42] W. Dickson, G. A. Wurtz, P. R. Evans, R. J. Pollard, and A. V. Zayats, "Electronically controlled surface plasmon dispersion and optical transmission through metallic hole arrays using liquid crystal," *Nano letters*, vol. 8, pp. 281-286, 2008.
- [43] B. Brian, B. Sepúlveda, Y. Alaverdyan, L. M. Lechuga, and M. Käll, "Sensitivity enhancement of nanoplasmonic sensors in low refractive index substrates," *Optics express*, vol. 17, pp. 2015-2023, 2009.
- [44] T.-H. Park, N. Mirin, J. B. Lassiter, C. L. Nehl, N. J. Halas, and P. Nordlander, "Optical properties of a nanosized hole in a thin metallic film," *Acs Nano*, vol. 2, pp. 25-32, 2008.
- [45] A. B. Dahlin, J. O. Tegenfeldt, and F. Höök, "Improving the Instrumental Resolution of Sensors Based on Localized Surface Plasmon Resonance," *Analytical Chemistry*, vol. 78, pp. 4416-4423, 2006/07/01 2006.
- [46] Y.-W. Jiang, L. D. Tzuang, Y.-H. Ye, Y.-T. Wu, M.-W. Tsai, C.-Y. Chen, *et al.*, "Effect of Wood's anomalies on the profile of extraordinary transmission spectra through metal periodic arrays of rectangular subwavelength holes with different aspect ratio," *Optics express*, vol. 17, pp. 2631-2637, 2009.
- [47] S. K. Gray, "Theory and Modeling of Plasmonic Structures," *The Journal of Physical Chemistry C*, vol. 117, pp. 1983-1994, 2012.
- [48] J.-Y. Laluet, E. Devaux, C. Genet, T. W. Ebbesen, J.-C. Weeber, and A. Dereux, "Optimization of surface plasmons launching from subwavelength hole arrays: modelling and experiments," *Optics express*, vol. 15, pp. 3488-3495, 2007.
- [49] G. Ctistis, E. Papaioannou, P. Patoka, J. Gutek, P. Fumagalli, and M. Giersig, "Optical and magnetic properties of hexagonal arrays of subwavelength holes in optically thin cobalt films," *Nano letters*, vol. 9, pp. 1-6, 2008.
- [50] J. Ji, J. G. O'Connell, D. J. Carter, and D. N. Larson, "High-throughput nanohole array based system to monitor multiple binding events in real time," *Analytical chemistry*, vol. 80, pp. 2491-2498, 2008.

- [51] J. Elliott, I. I. Smolyaninov, N. I. Zheludev, and A. V. Zayats, "Polarization control of optical transmission of a periodic array of elliptical nanoholes in a metal film," *Optics letters*, vol. 29, pp. 1414-1416, 2004.
- [52] R. Gordon, A. Brolo, A. McKinnon, A. Rajora, B. Leathem, and K. Kavanagh, "Strong polarization in the optical transmission through elliptical nanohole arrays," *Physical review letters*, vol. 92, p. 037401, 2004.
- [53] P. Lovera, D. Jones, B. Corbett, and A. O'Riordan, "Polarization tunable transmission through plasmonic arrays of elliptical nanopores," *Optics express*, vol. 20, pp. 25325-25332, 2012.
- [54] J. Li, H. Iu, D. Lei, J. Wan, J. Xu, H. Ho, *et al.*, "Dependence of surface plasmon lifetimes on the hole size in two-dimensional metallic arrays," *Applied Physics Letters*, vol. 94, p. 183112, 2009.
- [55] T. Ellenbogen, K. Seo, and K. B. Crozier, "Chromatic plasmonic polarizers for active visible color filtering and polarimetry," *Nano letters*, vol. 12, pp. 1026-1031, 2012.
- [56] H. Ghaemi, T. Thio, D. e. a. Grupp, T. W. Ebbesen, and H. Lezec, "Surface plasmons enhance optical transmission through subwavelength holes," *Physical Review B*, vol. 58, p. 6779, 1998.
- [57] C. Genet, M. P. van Exter, and J. Woerdman, "Fano-type interpretation of red shifts and red tails in hole array transmission spectra," *Optics Communications*, vol. 225, pp. 331-336, 2003.
- [58] A. Gabriel, J.-P. Connerade, S. Thiery, and P. Boumier, "Application of Fano profiles to asymmetric resonances in helioseismology," *Astronomy & Astrophysics*, vol. 380, pp. 745-749, 2001.
- [59] N. C. Lindquist, P. Nagpal, K. M. McPeak, D. J. Norris, and S.-H. Oh, "Engineering metallic nanostructures for plasmonics and nanophotonics," *Reports on progress in physics. Physical Society (Great Britain)*, vol. 75, p. 036501, 2012.

- [60] J. M. McMahon, J. Henzie, T. W. Odom, G. C. Schatz, and S. K. Gray, "Tailoring the sensing capabilities of nanohole arrays in gold films with Rayleigh anomaly-surface plasmon polaritons," *Optics express*, vol. 15, pp. 18119-18129, 2007.
- [61] K. S. Yee, "Numerical solution of initial boundary value problems involving Maxwell's equations in isotropic media," *IEEE Trans. Antennas Propag*, vol. 14, pp. 302-307, 1966.
- [62] H. Bao, X. Ruan, and T. S. Fisher, "Optical properties of ordered vertical arrays of multi-walled carbon nanotubes from FDTD simulations," *Optics express*, vol. 18, pp. 6347-6359, 2010.
- [63] V. Canpean and S. Astilean, "Multifunctional plasmonic sensors on low-cost subwavelength metallic nanoholes arrays," *Lab on a Chip*, vol. 9, pp. 3574-3579, 2009.
- [64] M. J. Kim, B. McNally, K. Murata, and A. Meller, "Characteristics of solid-state nanometre pores fabricated using a transmission electron microscope," *Nanotechnology*, vol. 18, p. 205302, 2007.
- [65] Y. H. Lanyon, G. De Marzi, Y. E. Watson, A. J. Quinn, J. P. Gleeson, G. Redmond, *et al.*, "Fabrication of nanopore array electrodes by focused ion beam milling," *Analytical chemistry*, vol. 79, pp. 3048-3055, 2007.
- [66] C. Chin, "Fabrication of metallic nanoparticle arrays," *Journal of Young Investigators*, vol. 16, p. 1, 2007.
- [67] T. W. Odom, V. R. Thalladi, J. C. Love, and G. M. Whitesides, "Generation of 30-50 nm structures using easily fabricated, composite PDMS masks," *Journal of the American Chemical Society*, vol. 124, pp. 12112-12113, 2002.
- [68] J. W. Menezes, J. Ferreira, M. J. Santos, L. Cescato, and A. G. Brolo, "Large-Area Fabrication of Periodic Arrays of Nanoholes in Metal Films and Their Application in Biosensing and Plasmonic-Enhanced Photovoltaics," *Advanced Functional Materials*, vol. 20, pp. 3918-3924, 2010.
- [69] N. C. Lindquist, M. A. Turner, and B. P. Heppner, "Template fabricated plasmonic nanoholes on analyte-sensitive substrates for real-time vapor sensing," *RSC Advances*, vol. 4, pp. 15115-15121, 2014.

- [70] J. Zhou and G. Yang, "Focused ion-beam based nanohole modeling, simulation, fabrication, and application," *Journal of manufacturing science and engineering*, vol. 132, p. 011005, 2010.
- [71] C.-K. Chang, D.-Z. Lin, C.-S. Yeh, C.-K. Lee, Y.-C. Chang, M.-W. Lin, *et al.*, "Experimental analysis of surface plasmon behavior in metallic circular slits," *Applied physics letters*, vol. 90, p. 061113, 2007.
- [72] C. Volkert and A. Minor, "Focused ion beam microscopy and micromachining," *MRS bulletin*, vol. 32, pp. 389-399, 2007.
- [73] M. E. Stewart, C. R. Anderton, L. B. Thompson, J. Maria, S. K. Gray, J. A. Rogers, *et al.*, "Nanostructured plasmonic sensors," *Chemical reviews*, vol. 108, pp. 494-521, 2008.
- [74] Q. Yu, P. Guan, D. Qin, G. Golden, and P. M. Wallace, "Inverted size-dependence of surface-enhanced Raman scattering on gold nanohole and nanodisk arrays," *Nano letters*, vol. 8, pp. 1923-1928, 2008.
- [75] L. J. Guo, "Nanoimprint lithography: methods and material requirements," *Advanced Materials*, vol. 19, pp. 495-513, 2007.
- [76] M. Hegner, P. Wagner, and G. Semenza, "Ultralarge atomically flat template-stripped Au surfaces for scanning probe microscopy," *Surface Science*, vol. 291, pp. 39-46, 1993.
- [77] H. Im, S. H. Lee, N. J. Wittenberg, T. W. Johnson, N. C. Lindquist, P. Nagpal, *et al.*, "Template-stripped smooth Ag nanohole arrays with silica shells for surface plasmon resonance biosensing," *ACS nano*, vol. 5, pp. 6244-6253, 2011.
- [78] H. Liu, B. Wang, E. S. Leong, P. Yang, Y. Zong, G. Si, *et al.*, "Enhanced surface plasmon resonance on a smooth silver film with a seed growth layer," *ACS nano*, vol. 4, pp. 3139-3146, 2010.
- [79] J. Menezes, L. Barea, E. Chillcce, N. Frateschi, and L. Cescato, "Comparison of plasmonic arrays of holes recorded by interference lithography and focused ion beam," *Photonics Journal, IEEE*, vol. 4, pp. 544-551, 2012.

- [80] J. Henzie, J. Lee, M. H. Lee, W. Hasan, and T. W. Odom, "Nanofabrication of plasmonic structures*," *Annual review of physical chemistry*, vol. 60, pp. 147-165, 2009.
- [81] A. Biswas, I. S. Bayer, A. S. Biris, T. Wang, E. Dervishi, and F. Faupel, "Advances in top-down and bottom-up surface nanofabrication: Techniques, applications & future prospects," *Advances in colloid and interface science*, vol. 170, pp. 2-27, 2012.
- [82] D. Whang, S. Jin, Y. Wu, and C. M. Lieber, "Large-scale hierarchical organization of nanowire arrays for integrated nanosystems," *Nano Letters*, vol. 3, pp. 1255-1259, 2003.
- [83] J. Cabaj and J. Sołoducho, "Layered biosensor construction," 2013.
- [84] T. P. Bigioni, X.-M. Lin, T. T. Nguyen, E. I. Corwin, T. A. Witten, and H. M. Jaeger, "Kinetically driven self assembly of highly ordered nanoparticle monolayers," *Nature materials*, vol. 5, pp. 265-270, 2006.
- [85] L. Chen, X. Zeng, T. Ren, and W. Briscoe, "Self-Assembly in an Evaporating Nanofluid Droplet: Rapid Transformation of Nanorods into 3D Fibre Network Structures," *Soft Matter*, 2014.
- [86] C. Schopf, A. Martín, M. Burke, D. Jones, A. Pescaglini, A. O'Riordan, *et al.*, "Au nanorod plasmonic superstructures obtained by a combined droplet evaporation and stamping method," *Journal of Materials Chemistry C*, vol. 2, pp. 3536-3541, 2014.
- [87] J.-F. Masson, M.-P. Murray-Méthot, and L. S. Live, "Nanohole arrays in chemical analysis: manufacturing methods and applications," *Analyst*, vol. 135, pp. 1483-1489, 2010.
- [88] W. Wu, D. Dey, O. G. Memis, A. Katsnelson, and H. Mohseni, "A novel self-aligned and maskless process for formation of highly uniform arrays of nanoholes and nanopillars," *Nanoscale Research Letters*, vol. 3, pp. 123-127, 2008.
- [89] B. Wang, H. Gao, J. Y. Lau, and S. J. Chua, "Investigation of transmission of Au films with nanohole arrays created by nanosphere lithography," *Applied Physics A*, vol. 107, pp. 139-143, 2012.

- [90] P. A. Smith, C. D. Nordquist, T. N. Jackson, T. S. Mayer, B. R. Martin, J. Mbindyo, *et al.*, "Electric-field assisted assembly and alignment of metallic nanowires," *Applied Physics Letters*, vol. 77, pp. 1399-1401, 2000.
- [91] O. Harnack, C. Pacholski, H. Weller, A. Yasuda, and J. M. Wessels, "Rectifying behavior of electrically aligned ZnO nanorods," *Nano Letters*, vol. 3, pp. 1097-1101, 2003.
- [92] J. L. Baker, A. Widmer-Cooper, M. F. Toney, P. L. Geissler, and A. P. Alivisatos, "Device-scale perpendicular alignment of colloidal nanorods," *Nano letters*, vol. 10, pp. 195-201, 2009.
- [93] S. Hanash, "Disease proteomics," *Nature*, vol. 422, pp. 226-232, 2003.
- [94] C. M. Perou, T. Sørli, M. B. Eisen, M. van de Rijn, S. S. Jeffrey, C. A. Rees, *et al.*, "Molecular portraits of human breast tumours," *Nature*, vol. 406, pp. 747-752, 2000.
- [95] A. A. Sinha, M. T. Lopez, and H. O. McDevitt, "Autoimmune diseases: the failure of self tolerance," *Science*, vol. 248, pp. 1380-1388, 1990.
- [96] S. Choi, M. Goryll, L. Y. M. Sin, P. K. Wong, and J. Chae, "Microfluidic-based biosensors toward point-of-care detection of nucleic acids and proteins," *Microfluidics and Nanofluidics*, vol. 10, pp. 231-247, 2011.
- [97] K. A. Erickson and P. Wilding, "Evaluation of a novel point-of-care system, the i-STAT portable clinical analyzer," *Clinical Chemistry*, vol. 39, pp. 283-287, 1993.
- [98] J. Wang, "Electrochemical biosensors: towards point-of-care cancer diagnostics," *Biosensors and Bioelectronics*, vol. 21, pp. 1887-1892, 2006.
- [99] A. J. Tüdös, G. A. Besselink, and R. B. Schasfoort, "Trends in miniaturized total analysis systems for point-of-care testing in clinical chemistry," *Lab on a Chip*, vol. 1, pp. 83-95, 2001.
- [100] E. C. Breen, "An Overview of the Immune System, Part One: The Cells and Cell Surface Molecules," 2007.

- [101] T. Storni, T. M. Kündig, G. Senti, and P. Johansen, "Immunity in response to particulate antigen-delivery systems," *Advanced drug delivery reviews*, vol. 57, pp. 333-355, 2005.
- [102] Z. A. Ahmad, S. K. Yeap, A. M. Ali, W. Y. Ho, N. B. M. Alitheen, and M. Hamid, "scFv antibody: principles and clinical application," *Journal of Immunology Research*, vol. 2012, 2012.
- [103] E. Engvall and P. Perlmann, "Enzyme-linked immunosorbent assay (ELISA) quantitative assay of immunoglobulin G," *Immunochemistry*, vol. 8, pp. 871-874, 1971.
- [104] S. H. Snyder, J. Axelrod, and M. Zweig, "A sensitive and specific fluorescence assay for tissue serotonin," *Biochemical pharmacology*, vol. 14, pp. 831-835, 1965.
- [105] W. N. Burnette, "'Western blotting': electrophoretic transfer of proteins from sodium dodecyl sulfate-polyacrylamide gels to unmodified nitrocellulose and radiographic detection with antibody and radioiodinated protein A," *Analytical biochemistry*, vol. 112, pp. 195-203, 1981.
- [106] B. Xi, N. Yu, X. Wang, X. Xu, and Y. Abassi, "The application of cell-based label-free technology in drug discovery," *Biotechnology journal*, vol. 3, pp. 484-495, 2008.
- [107] Y. Fang, "Label-free cell-based assays with optical biosensors in drug discovery," *Assay and drug development technologies*, vol. 4, pp. 583-595, 2006.
- [108] M. A. Cooper, "Non-optical screening platforms: the next wave in label-free screening?," *Drug discovery today*, vol. 11, pp. 1068-1074, 2006.
- [109] M. Nirschl, F. Reuter, and J. Vörös, "Review of transducer principles for label-free biomolecular interaction analysis," *Biosensors*, vol. 1, pp. 70-92, 2011.
- [110] C. Boozer, G. Kim, S. Cong, H. Guan, and T. Londergan, "Looking towards label-free biomolecular interaction analysis in a high-throughput format: a review of new surface plasmon resonance technologies," *Current opinion in biotechnology*, vol. 17, pp. 400-405, 2006.
- [111] W. Moerner, "New directions in single-molecule imaging and analysis," *Proceedings of the National Academy of Sciences*, vol. 104, pp. 12596-12602, 2007.

- [112] L. RUS, "Wireless-Electrodeless High-Sensitive Immunosensor."
- [113] R. J. Chen, H. C. Choi, S. Bangsaruntip, E. Yenilmez, X. Tang, Q. Wang, *et al.*, "An investigation of the mechanisms of electronic sensing of protein adsorption on carbon nanotube devices," *Journal of the American Chemical Society*, vol. 126, pp. 1563-1568, 2004.
- [114] S. Evoy, N. DiLello, V. Deshpande, A. Narayanan, H. Liu, M. Riegelman, *et al.*, "Dielectrophoretic assembly and integration of nanowire devices with functional CMOS operating circuitry," *Microelectronic Engineering*, vol. 75, pp. 31-42, 2004.
- [115] M. Estevez, M. A. Otte, B. Sepulveda, and L. M. Lechuga, "Trends and challenges of refractometric nanoplasmonic biosensors: A review," *Analytica chimica acta*, vol. 806, pp. 55-73, 2014.
- [116] A. Lesuffleur, H. Im, N. C. Lindquist, K. S. Lim, and S.-H. Oh, "Laser-illuminated nanohole arrays for multiplex plasmonic microarray sensing," *Optics express*, vol. 16, pp. 219-224, 2008.
- [117] <http://www.grandviewresearch.com/industry-analysis/biosensors-market>.

Chapter 2

Fabrication of plasmonic nanohole arrays and their use as label free biosensors

2.1 Introduction

In the last decade, Surface Plasmon Resonance (SPR) based devices have proven to be invaluable tools for label-free and real-time analysis of immunoassays. Owing to their extreme sensitivity to surface changes, SPR systems have been successfully used for sensing of a variety of biomaterials such as DNA, protein, bacteria and viruses [1-5]. In currently commercially available devices however, surface plasmons are excited *via* a prism coupling method - known as the Kretschmann configuration. While effective and robust, this excitation method suffers from a few drawbacks. Indeed, the angled excitation used in this setup limits multiplexing capabilities as well as miniaturisation of the instrument. Also, the need for a coupling prism does not allow for low cost consumables.

Nanotechnology has been shown to open up numerous possibilities and opportunities for sensing based on optical, electrical or electrochemical phenomena [6-11]. Interestingly, it was found that using a nanotechnology approach to surface plasmon sensing could overcome the limitations currently faced by commercial SPR equipment. Indeed, Ebbesen et al [12] showed in 1998 that nanostructuring a thin metallic film with a periodic arrangement of nanoholes allowed for the excitation of surface plasmons, using a collimated light at normal incidence. This nanostructuring could be done in an array format to allow for multiplexing. Also, constant advances in nanotechnology fabrication methods such as nano-imprinting, offer interesting prospects for high-throughput, low-cost manufacturing of consumables.

Furthermore, this nanostructuring could be done in an array format to allow for multiplexing. Also, constant advances in nanotechnology fabrication methods such as nano-imprinting, offer interesting prospects for high-throughput, low-cost manufacturing of consumables. Brolo et al [13] were the first to report on label-free biosensing using such arrays of nanoholes. Since then, a number of groups have reported detection of various biomaterials such as antigens, viruses or bacteria [14-16] using similar samples. Many fabrication methods, including Focused Ion Beam (FIB) milling, nano-imprinting, electron beam lithography and template stripping have been investigated and reported [17-22]. Although elegant, these approaches have some limitations. FIB techniques can damage the underlying substrate, increasing scattering and reducing optical coupling to the sensor, while lithography approaches can also leave

residual material in the nanoholes, again reducing coupling efficiency. Finally the chrome or titanium adhesion layer (for gold) is known to dampen plasmons.

In this chapter, I look to surmount these problems by nanopatterning a thin gold film (50 nm thick) on a donor substrate followed by lift-off and self-assembly of these sensors onto a pristine host substrate. I use a FIB approach to rapidly prototype the sensor arrays and use a combination of capillary and fluidic forces to self-assemble the sensors. A combination of scanning electron microscopy (SEM), atomic force microscopy (AFM) and optical microscopy was used to characterize the fabricated samples. Prior to fabrication, 3D Finite Difference Time Domain (FDTD) simulations were carried out to tailor the periodicity and size of the nanoholes. This numerical study also allowed the profile of the electric fields around the holes to be examined and permitted the identification of the spectral features of interest for sensing applications. The bulk refractive index sensing capabilities of the fabricated sample was assessed by monitoring the spectral changes of the far-field transmission spectra in the presence of solutions with varying refractive index. To demonstrate label-free sensing, a bioassay was developed using a commercial SPR system, along with the clean and attachment chemistry needed to transfer the assay to the nanohole array. The bio-sensing potential of the fabricated samples is examined by observing the spectral shifts in the transmission spectra upon attachment of a monolayer of Mercaptododecanoic acid (MDA), followed by attachment of antibodies and then antigen.

This work has been submitted for publication as “Fabrication of plasmonic nanohole arrays and their use as label-free immuno-biosensors”, *Biosensors & Bioelectronics*

2.2 Experimental

2.2.1 Metal evaporation

To fabricate nanohole arrays, a 5 nm Cr film was first deposited on a clean Si substrate by metal evaporation (Temescal FC-2000 E-beam evaporator), followed by evaporation of 50 nm thick Au layer.

2.2.2 FIB milling

The sample was then loaded into the Quanta™ 3D 200i DualBeam™ Focused Ion Beam (FIB). The ion beam was focused on an area near to where the arrays will be milled, as when focusing the beam the gold surface is damaged by the ions. Individual $60\ \mu\text{m} \times 60\ \mu\text{m}$ periodic nanohole arrays with a pitch of 450 nm were fabricated on the sample (30 kV beam voltage, 300 pA beam current, 1 pass, a defocus of 14 μm and dwell time of 14 ms). As the beam current controls the quantity of Ga^+ ions, lower currents produce a smaller spot size but mill at a much slower rate while higher currents make a bigger hole, faster. 300 pA was found to give holes of about 80 nm in diameter in a reasonable time. At higher currents the hole size was too large and irregular; unsuitable for sensing applications. To make 110 nm holes the 300 pA beam was defocused slightly to increase the size of the nanohole.

2.2.3 Lift off

The 50 nm films were then freed from the underlying Si substrate by wet etching the underlying chromium layer (Chrome Etchant Lodyne, Grower Chemicals Ltd.) for 10 minutes. The chip was then removed and immersed into deionised water where the Au film floated on the surface (due to surface tension of the water meniscus) while the Si substrate sank to the bottom. Using this approach the highly fragile gold films were easily freed from the silicon substrate in a contactless manner that prevented any damage occurring to the film. Finally, a glass microscope slide was immersed under the gold nanostructured film and used to lift the film from the water and dried for 24 hours.

2.2.4 Simulations

Finite Difference Time Domain (FDTD) simulations were performed using JFDTD3D (version 2.0) program [13] available under the General Public License (GPL). The program is based on a 3-D, parallel FDTD implementation using the Message Passing

Interface library. The code was run on 8 nodes, each node having 2 Opteron CPUs (2.6 GHz, 4 GB RAM).

2.2.4.1 Computational volume

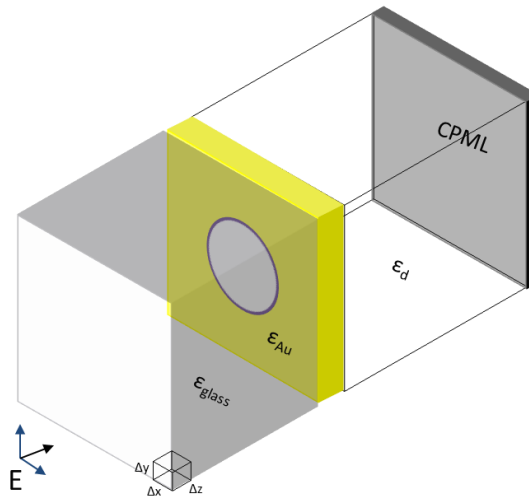


Figure 2.1: Schematic of the simulation setup

The grid spacing in each spatial dimension was 5 nm. The computational grid was chosen to be 450 nm × 450 nm × 1600 nm. The extra lengths in the z directions allowed the resolution of Raleigh-Wood's anomalies, if present. Periodic boundary conditions (450 nm) in the x and y directions were applied to simulate an infinite square array. Perfectly Matching Layers (PML) boundary conditions were imposed in the z direction in order to avoid reflections from the edges of the computational window. The setup was modelled (Figure 2.1) by a 50 nm Au film with a 650 nm thick glass substrate ($\epsilon_{Glass} = 2.31 \epsilon_0$) and a 900 nm dielectric (air/water) (ϵ_d) superstrate. In the plane of the film, the nanohole was centered in the middle of the square ($x_0 = y_0 = 225 \times 10^{-9}$) and the equation used to define the circle is,

$$\frac{(x_{pos} - x_0)^2 + (y_{pos} - y_0)^2}{(55 \times 10^{-9})^2} = 1 \quad (2.1)$$

2.2.4.2 Permittivity of gold

The permittivity of gold was modelled using a Drude plus two-pole Lorentz model,

$$\epsilon_{Au}(\omega) = \epsilon_0 + \sum_{1,2} \frac{\omega_{Ln}^2 \Delta \epsilon_{Ln}}{\omega(\omega + i2\delta_{Ln}) - \omega_{Ln}^2} - \frac{\omega_D^2}{\omega^2 + i\gamma_D \omega} \quad (2.2)$$

with Drude parameters; $\epsilon_\infty = 5.40$, $\gamma_D = 0.103 \times 10^{15} \text{ Hz}$ and $\omega_D = 0.14 \times 10^{17} \text{ Hz}$.

And Lorentz parameters,

$$\omega_{L1} = 0.42 \times 10^{16} \text{ Hz}, \omega_{L2} = 0.523 \times 10^{16} \text{ Hz}, \Delta\epsilon_{L1} = 2.542 \times 0.279,$$

$$\Delta\epsilon_{L2} = 2.542 \times 0.721, \delta_{L1} = 0.435 \times 10^{15} \text{ Hz}, \delta_{L2} = 0.661 \times 10^{15} \text{ Hz}.$$

2.2.4.3 Transmission spectra

In order to simulate the excitation source, a Gaussian damped sinusoidal pulse (having a frequency content of 1 to 6 eV) was launched from the glass side and simulation run (for 200×10^{-15} sec) in the time domain. Total transmission spectra were obtained by Fourier transforming the simulated electric and magnetic fields on a surface above the holes and constructing the surface integral of the outward Poynting vector.

2.2.5 Optical images

Optical micrographs were acquired using a calibrated microscope (Axioskop II, Carl Zeiss Ltd.) equipped with a charge-coupled detector camera (CCD; CoolSNAP cf, Photometrics).

2.2.6 Transmission spectra

Transmission spectra of samples were collected using a combination of an Olympus IX71 inverted microscope and an Acton SP2300i spectrograph equipped with a 300 gr/mm grating and a 20 μm slit (resolution of ~ 0.1 nm), see Figure 2.2.

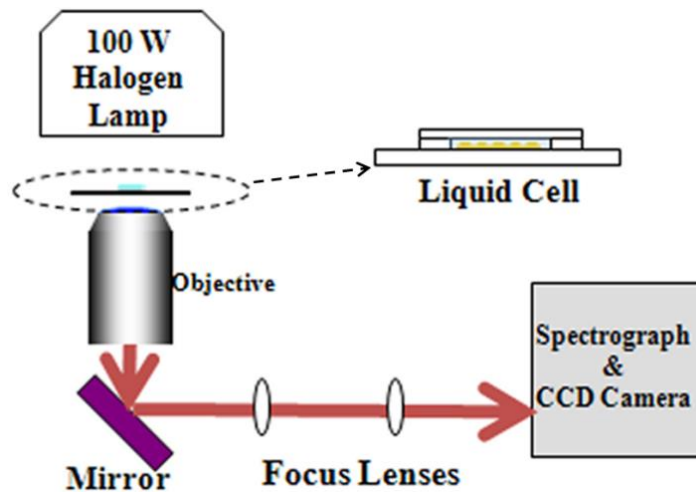


Figure 2.2: Schematic diagram of the setup used to collect transmission spectra.

A 100 W Halogen white light source was used to illuminate the sample, with the incident angle of light within 10 degrees with respect to the normal of sample. All

recorded transmission spectra were normalized with respect to a glass substrate. A simple microfluidic cell was constructed by gluing two pieces of 0.15 mm thick cover slip on either side of the adsorbed gold film (using UV curable glue) on a microscope slide. A third cover slip was bridged over these pieces of cover to form a lid of the cell. Surface tension forces from the fluid under investigation were sufficient to hold the lid in place during experiments.

2.2.7 SEM

Scanning electron microscopy (SEM) images of self-assembled nanohole arrays were acquired using a field emission SEM (JSM-6700F, JEOL UK Ltd.) operating at beam voltages between 5 and 10 kV.

2.2.8 AFM

The topography of both pristine and biologically modified gold films were characterized using a calibrated atomic force microscope (AFM; Dimension 3100, Veeco Instruments Inc.) in tapping mode with commercial tapping mode probes (MP-11100, Veeco Instruments Inc; typical radius of curvature ~ 10 nm and front/side cone angles of 15°/17.5°, respectively). No processing was applied to data apart from the usual background plane subtraction.

2.2.9 Bulk refractive index sensing

NaCl solutions (99.5%, Sigma Aldrich) were prepared by dissolving 0, 8, 12, 16, and 21g in 100 ml of deionized water to form solutions with refractive indices of 1.333, 1.347, 1.354, 1.361 and 1.370; respectively.

2.2.10 Attachment chemistry

2.2.10.1 Gold cleans

Before attaching biomolecules to the gold surface it must be cleaned to remove any organic or inorganic material. A variety of cleans were examined, including polishing, solvent, acid and ozone. AFM images and contact angle measurements were taken before and after each clean to examine the surface. In general, acid cleans (such as Piranha clean) are used but these proved too harsh for the thin film as the reaction damaged the nanohole arrays. Similarly, polishing left trenches in the gold. A combination of a solvent clean followed by UV ozone was used as this left a smooth

film and cleaned it sufficiently. The AFM and contact angle measurements after this clean can be seen in Figure 2.3.

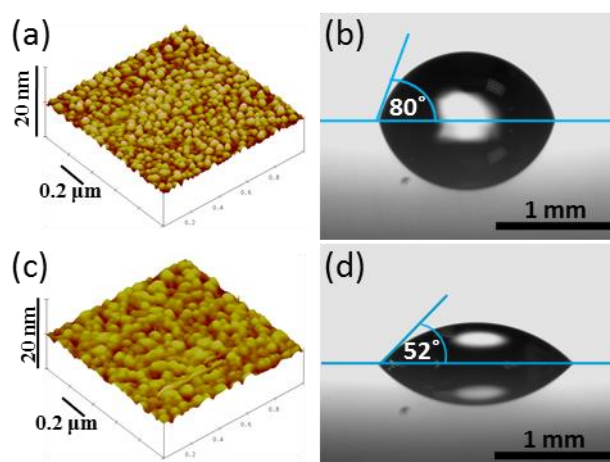


Figure 2.3: (a) AFM image of a 1 μm by 1 μm section of a gold film prior to any fabrication/clean. RMS \sim 1.59 (b) contact angle for the measurement from a 0.5 μl drop of water on the gold surface. Angle is 80 degrees showing the surface is almost hydrophobic. (c) AFM image of the gold film after a solvent/UV ozone clean. RMS \sim 1.67. (d) Contact angle image after the clean, 52 degrees, showing increased hydrophilicity.

The clean procedure was to first solvent clean by immersing the chip in acetone, trichloroethylene, acetone, IPA and DI water, respectively, each for 10 min. The film was then dried in a stream of N₂ and placed in a UV ozone cleaner (AFM Tip Cleaner, Bioforce Laboratory) for 20 min at both ambient temperature and oxygen concentrations.

2.2.10.2 Sensor biomodification

Following the cleaning of the self-assembled gold film, the chip was immersed in a 5 mM Mercaptododecanoic acid solution (MDA in 99% Ethanol, Sigma Aldrich) for 24 hours to assemble an ordered monolayer of MDA on the gold surface. After 24 hours, the chip was removed from the MDA solution, carefully rinsed with ethanol and dried under a nitrogen stream. The gold surface was then activated by immersing in 200 mM ethyl-(N',N'-dimethylamino)propylcarbodiimide hydrochloride (EDC) and 25 mM N-hydroxysulfosuccinimide (NHS) for 30 min. A 200 μl aliquot of biological

probe content, murine monoclonal (mAb) anti human IgG antibody (whole molecule, 14 µg/ml, Sigma Aldrich) in sodium acetate buffer, pH 4.5 (Sierra sensors) was then deposited on the gold surface and allowed to covalently couple for two hours at room temperature. This was followed by a blocking step, ethanolamine-HCl, pH 8.5 (Sierra Sensors), 1 M for 30 minutes. The gold film was then subsequently rinsed with 0.1 M PBS (pH 7.2 – Sigma Aldrich) and dried under a nitrogen stream. A 200 µl aliquot of target antigen (4 µg/ml human IgG protein, whole molecule, Sigma Aldrich) in PBS, was dropped on the gold and allowed incubate for 2 hours at ambient temperature. The gold film was then rinsed in 0.1 M PBS to remove excess antigen and dried in a N₂ stream. Transmission spectra were recorded in 0.1 M PBS buffer following each biological addition step.

2.2.11 SPR assay

The above assay was first optimised on a commercial Surface Plasmon Resonance system (SPR-2, Sierra Sensors GmbH). All assay components (antibody, antigen, buffers, etc.) used were identical. Note that in this case however, the commercial gold coated prisms were pre-coated with Mercaptohexadecanoic acid (MHDA), so that this initial step was not required.

The procedure had a 25 µl/min flowrate and all injections were 200 µl (8 minute injections), with PBS as running buffer. The injections were,

- 1) EDC/NHS – for surface activation.
- 2) Ab - murine monoclonal (mAb) anti human IgG antibody, whole molecule.
- 3) Ethanolamine – blocking step.
- 4) Ag - human IgG protein, whole molecule.

2.3 Results and discussion

2.3.1 Structural characterisation

Nanohole arrays with nanoholes ~ 110 nm in diameter and with a lattice period of 450 nm were routinely fabricated. Following FIB milling, the gold film was released by etching the underlying chrome layer and immersion in de-ionized water where the gold film was observed to float at the water – air interface due to surface tension effect as can be seen in Figure 2.4(a).

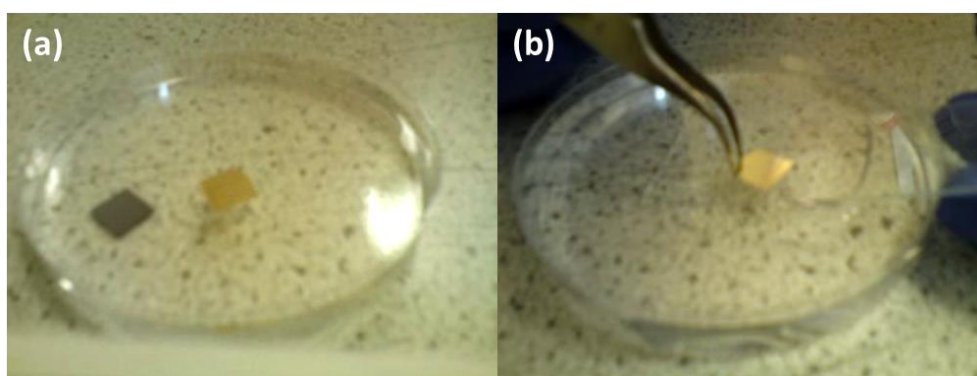


Figure 2.4: (a) Film floating in DI water, silicon has sunk to the bottom. (b) Film being removed onto a glass microscope slide.

Using this approach, illustrated in Figure 2.5, the highly fragile gold films were easily freed from the silicon substrate in a contactless manner. Finally, the nanostructured film was flow assembled onto a glass microscope slide (see Figure 2.4(b)) and allowed to dry for 24 h. After assembly, the film was observed to adhere strongly to the glass substrate *via* Van Der Waals interactions.

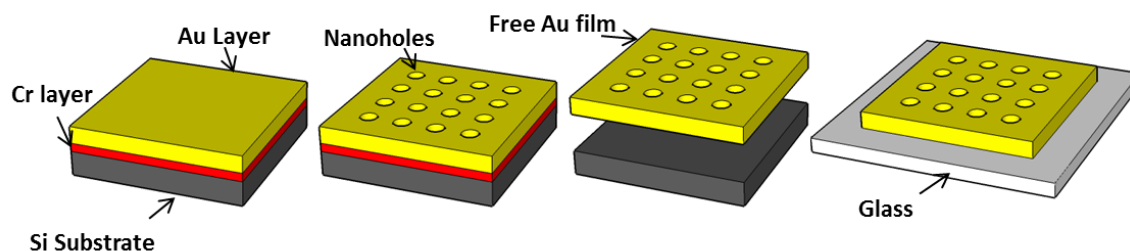


Figure 2.5: The fabrication process depicting the FIB milling and lift-off of a nanohole array.

There are two main benefits from using the fabrication and self-assembly approach described herein: firstly, removal of the chromium adhesion layer prevents dampening of the plasmonic effect on the Au-glass interface [23] that would otherwise in the presence of chromium. Secondly, self-assembly of a film onto a new pristine substrate eliminates any possibility of substrate damage arising during the FIB milling process, i.e., frosting effects causing unwanted light scattering from adversely interfering with optical transmission.

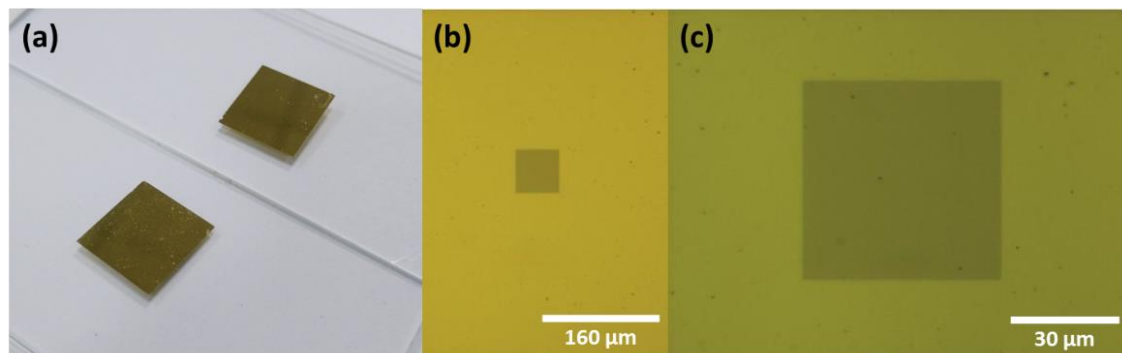


Figure 2.6: (a) Picture of gold films on glass microscope slides. (b) & (c) Optical images of an array at 10x & 50x magnification, respectively.

Figure 2.7 shows a SEM micrograph of a portion of a nanohole array prior to release of the film from the underlying silicon substrate. As can be seen in the inset of Figure 2.7, the surface of the film appears smooth with no debris and the edges of the nanohole sharp and well defined.

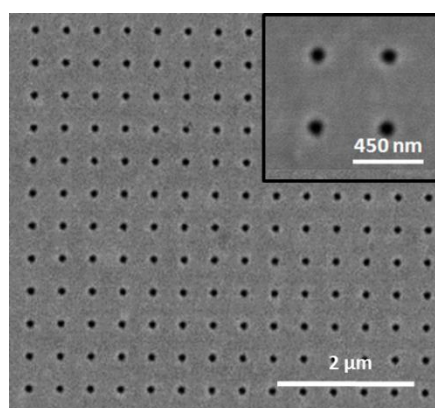


Figure 2.7: SEM image of the array before lift-off. The holes have a diameter of 110 nm and lattice period of 450 nm. Beam voltage of 10 kV, magnification 10,000x.

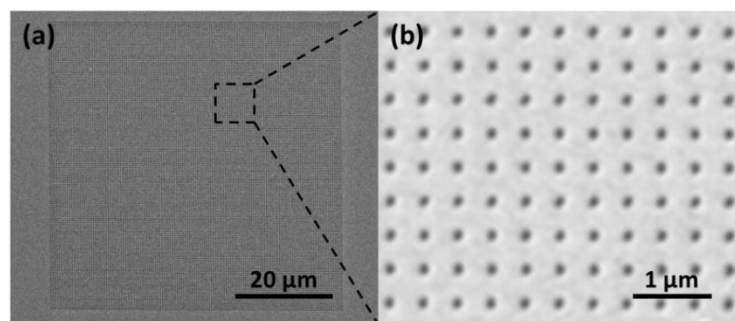


Figure 2.8: (a) SEM image of a nanohole array $60\ \mu\text{m} \times 60\ \mu\text{m}$ in size following assembly onto a transparent substrate. 10 kV, 3000x magnification (b) SEM of a portion of an array (10 kV, 10000x magnification); the lattice period is 450 nm and the nanohole diameter is 110 nm.

To assess the efficacy of the transfer process, Figure 2.8(a) shows a SEM image of a typical gold film bearing a nanohole array following its transfer by self-assembly onto a transparent substrate. Despite being only 50 nm in thickness, the film was sufficiently strong to survive the transfer. No wrinkles, tears or defects are evident in the film. The nanoholes are circular and well defined while the areas around them appear flat and smooth, showing that the etch hasn't widened the holes or roughened the film. Optical microscopy was employed to give a good first indication of whether the transfer process had damaged a gold film or not. Figure 2.9 shows the comparison of both optical and SEM micrographs of two films, one where the film is flat and smooth, and the other that was not successfully flow self-assembled where wrinkles are clearly evident in both micrographs. The fabrication and assembly yield was between 70-80% ($n=100$).

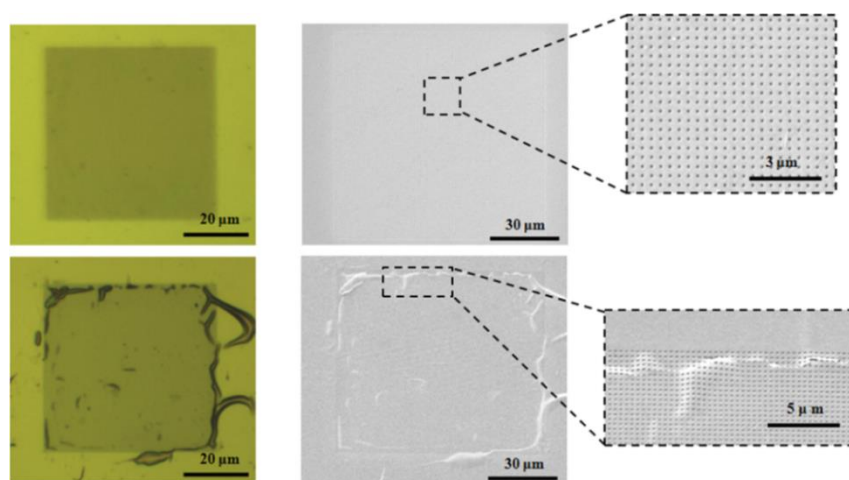


Figure 2.9: Comparison of a flat (top) and wrinkled (bottom) array with both optical and SEM images

2.3.2 Spectroscopic characterisation

Following assembly onto the transparent substrate, far-field transmission spectra were taken for a nanohole array in the presence of water ($n = 1.333$), see Figure 2.10. The spectrum exhibited a broad peak around $\lambda=490$ nm, with a transmission of $\sim 25\%$. This peak can also be found in the spectrum of a plain gold film and corresponds to direct transmission (interband transition) for gold as discussed in chapter 1.

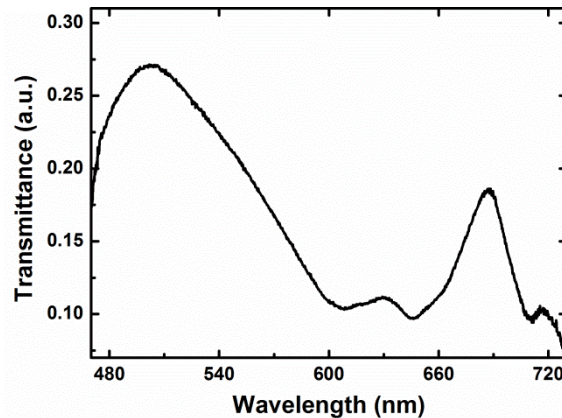


Figure 2.10: Far field transmission spectrum through a nanohole array in the presence of water obtained by illuminating the sample with a 100 W Halogen white light source and collecting the light using an Acton SP2300i spectrograph equipped with a 300 gr/mm grating and a 20 μm slit.

The dips at ~ 635 nm and ~ 720 nm in the spectrum can be explained by extraordinary transmission through sub-wavelength periodic nanohole arrays which is attributed to the excitation of surface plasmon polaritons of specific resonant orders. As discussed in Chapter 1, with incident light normal to the nanohole array the SPP modes (λ_{SPP}) may be approximated by the following equation [24, 25],

$$\lambda_{SPP} = \frac{P}{\sqrt{i^2 + j^2}} \sqrt{\frac{\epsilon_{Au}\epsilon_d}{\epsilon_{Au} + \epsilon_d}} \quad (2.1)$$

where P is the periodicity between nanoholes, i and j define the order of the mode, ϵ_{Au} is the permittivity of gold and ϵ_d the permittivity of the adjacent dielectric material [26]. The dip at 635 nm can be assigned to the $(1,0)_{Au/water}$ SPP. For the $(1,0)_{Au/water}$ SPP, the solution to equation 2.1 is 647 nm, see Table 2.1. One possible explanation for the apparent blue shift in the expected peak location would be the presence of a Rayleigh anomaly (RA) interacting with the SPP. In the case of a 2D grating with a periodicity

of 450 nm, the onset of the $(1,0)_{\text{water}}$ RA occurs at 607 nm, above which free-space light diffraction is forbidden in the order.

$$\lambda_{RA} = \frac{P}{\sqrt{i^2 + j^2}} \sqrt{\epsilon} \quad (2.2)$$

The 720 nm dip can be attributed to the $(1,0)_{\text{Au/glass}}$ SPP. This should theoretically be at 729 nm but like for the $(1,0)_{\text{Au/water}}$ SPP, there is a $(1,0)_{\text{glass}}$ RA at 684 nm that interfere with the SPP mode, see Table 2.1. The peak at ~680 nm is likely a combination of both the $(1,0)_{\text{Au/water}}$ SPP and the $(1,0)_{\text{glass}}$ RA [27].

Table 2.1: SSP and RA predictions. Solutions to equations 2.1 and 2.2.

SPP		RA	
Order	Wavelength (nm)	Order	Wavelength (nm)
$(1,0)_{\text{Au/water}}$	647	$(1,0)_{\text{water}}$	607
$(1,1)_{\text{Au/water}}$	533	$(1,1)_{\text{water}}$	430
$(1,0)_{\text{Au/glass}}$	729	$(1,0)_{\text{glass}}$	684
$(1,1)_{\text{Au/glass}}$	578	$(1,1)_{\text{glass}}$	484

To determine the optimal size of the array a number of different size arrays were fabricated varying in size from 10 μm by 10 μm , to 100 μm by 100 μm .

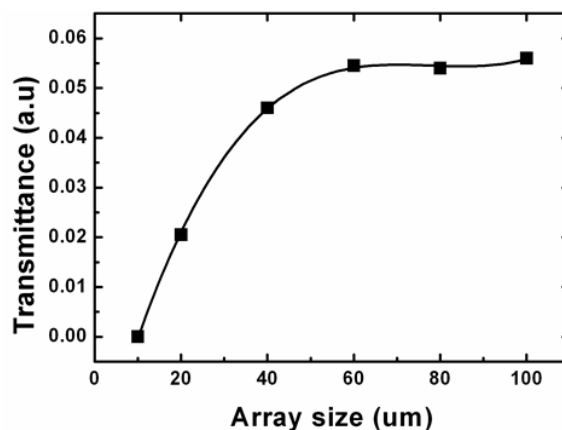


Figure 2.11: The intensity of the transmission spectra (at the 680 nm peak) through arrays which vary in size from 10 x 10 μm to 100 x 100 μm (black line is a guide to the eye).

Spectra were acquired through each of these arrays and the relative peak intensity measured. As is shown in Figure 2.11, it was found that the optimal size of an array for our optical setup was about 60 μm x 60 μm , as intensity of transmitted light reached a maximum at this size.

2.3.3 Simulations

To further understand the origins of the observed peaks and the presence of a RA, frequency-resolved near-field profiles were plotted at the wavelengths of interest. Figure 2.12(a) shows a side elevation view of the electric field distribution at 680 nm distributed symmetrically along both edges of nanohole when irradiated with unpolarized light corresponding to the Localized Surface Plasmon (LSP) resonance of the nanohole. The LSP is observed to be bound and concentrated on the top and bottom surfaces of the nanohole. The side view of an individual nanohole in a gold substrate following illumination by broad band white light field is highest on the surface of the gold film and extends some distance above and to the side of the nanoholes. As is seen in Figure 2.12(b) the field falls off sharply with distance from the film and is strongest at the top circle of the hole. Therefore, the medium directly in contact or very close to the surface of the film has the strongest effect on the relative refractive index of the surrounding medium, and a change occurring above this will have a minimum impact. This suggests that attaching/detaching small bio-molecules the nanohole will have a much larger effect than those free in bulk solution.

Figure 2.12(c) shows the far field transmission spectra for an array with a pitch of 450 nm and nanoholes of 110 nm. The black line shows the simulated spectra of the transmission through a gold film with no holes. The bulk peak for gold is present at ~ 500 nm but there are no peaks at higher wavelengths. The other two spectra are the simulated (in blue) and experimental (in red) of spectra through an array of nanoholes. Very good agreement between the experimental and simulated transmission spectra is observed. The discrepancy in the relative intensity may be attributed to minor imperfections in the nanohole structure such as errors in hole dimensions and sharpness of the hole edges, or to imperfections in the Drude-Lorentz model used in the simulation.

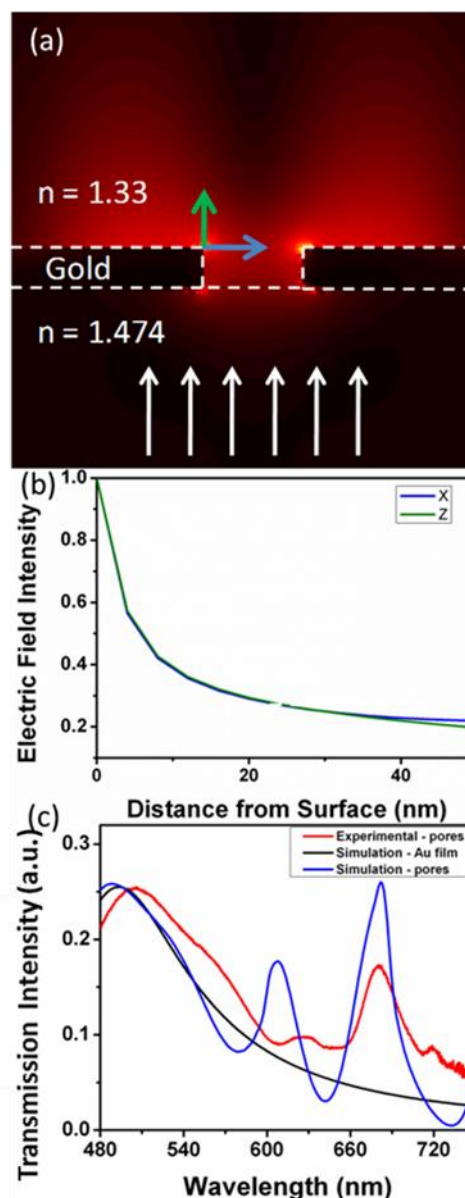


Figure 2.12: (a) Electric Field simulation of a cross section of a nanohole with glass substrate and water above the film. (b) The field intensity falls off sharply with over a 60% loss in the first 10 nm from the gold surface (data point every 5 nm) (c) Shows the simulated and real transmission spectra of the array.

2.3.4 Bulk refractive index measurements

In order to evaluate the refractive index sensing capabilities of these samples, far-field transmission spectra were measured in the presence of solutions with varying refractive index. Figure 2.13(a) shows the transmission spectra measured for a nanohole array in the presence of solutions with varying refractive index ($n = 1.333 \rightarrow n = 1.37$). There

is a redshift of the spectral features (spectral dip) in the 600-660 nm window as the refractive index of the superstrates increases from water ($n=1.333$) to a 21% w/v NaCl solution ($n=1.370$). As discussed previously, these features are related to SPP/RA on the Au-superstrate interface, and are therefore sensitive to its refractive index. It should also be noted that there is no spectral change above 680 nm. This was expected as this spectral range corresponds to plasmon optical effect occurring on the Au/Glass interface. Figure 2.13 (b) plots this red shift versus increasing refractive index, with the slope yielding a sensitivity of 347 nm/refractive index unit (RIU). This value compares favourably with similar samples fabricated using other techniques such as nanoimprint or electron beam lithography [13, 28, 29] and taken together with the fact that the electric field is confined to the surface of the sensors, suggests that these samples could be used for label-free sensing of biomaterial.

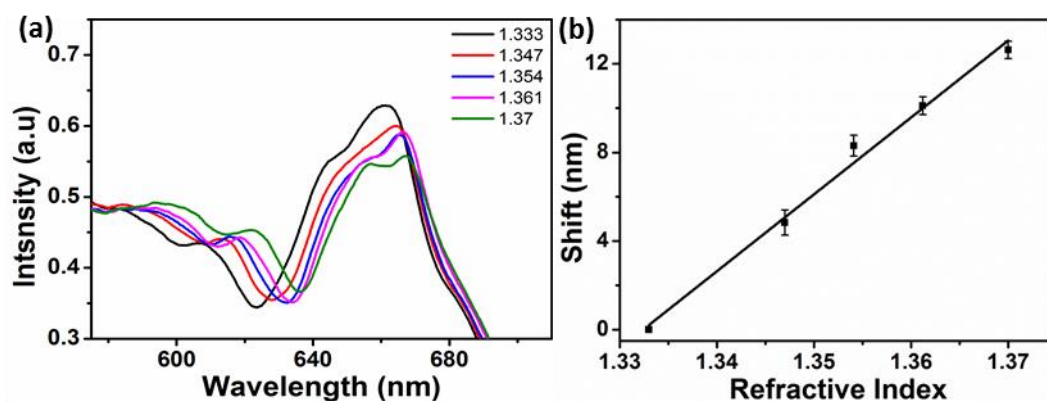


Figure 2.13: (a) Transmission spectra through a nanohole array in the presence of solution of varying refractive index ($n=1.333 \rightarrow n=1.370$). Water, $n=1.333$; 8% NaCl, $n=1.347$; 12% NaCl, $n=1.354$; 16% NaCl, $n=1.361$; 21% NaCl, $n=1.370$. The peaks shift to the right as the refractive index increases showing how the spectral features from the Nanohole arrays can be exploited for highly sensitive refractive sensing. (b) Shows the Peak Shift with varying refractive index with a shift of 347 nm per RIU. Error bars correspond to the standard deviation from 5 replications.

2.3.5 Assay development

Immunoassays were developed and optimised by internal collaborators using a commercial SPR system [30], and were then transferred to the nanohole arrays samples. Prior to transferring the assay, the cleaning procedure of the gold sample was optimised (Section 2.2.10.1) and validated by functionalising a cleaned sample using a biotin/streptavidin assay.

2.3.5.1 Gold attachment

In order to confirm that the cleaning procedure permitted subsequent surface attachment, a Biotin/Streptavidin assay was carried out on a planar film. AFM images were taken after each step to observe the surface after each molecule was attached. The surface roughness increased after each step which indicates molecules are binding to the surface. The topography is visibly altered and the streptavidin is visible in the image, Figure 2.14(d).

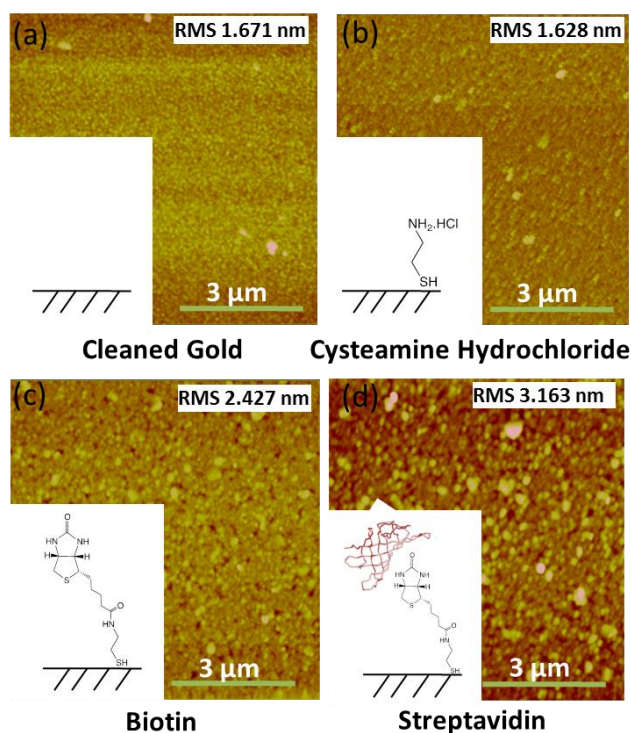


Figure 2.14: (a) AFM image of a clean gold surface, (b) AFM after attaching cysteamine hydrochloride to the gold. (c) AFM of the gold after Biotin is attached. Roughness greatly increased due to the biotin molecules. (d) AFM after Streptavidin is attached.

2.3.5.2 Surface Plasmon Resonance

Prior to immobilisation on gold films assays were first developed and optimised on a commercial SPR-2 using the biomolecules described in the experimental Section 2.2.10.2. The SPR measures a change as each layer of biomolecules is bound to the surface as can be seen in Figure 2.15(a). The different steps of the assay can clearly be distinguished:

- 1) Injection of EDC/NHS (linking chemistry): High increase in the RIU. This is a bulk shift due to the higher refractive index of the EDC/NHS solution (compared to the buffer)
- 2) Injection of antibody. The RIU initially decreases because the refractive index of the solution is lower than the one of the buffer. As the antibodies bind to the surface, the RIU then increases. At the end of the injection, the RIU value increases as the Ab solution is replaced by the buffer, leaving only the bound antibodies that are bound to the surface.
- 3) Injection of ethanolamine (blocking chemistry). Here again a bulk shift is observed, due to the higher RI of the solution ($n=1.454$).
- 4) Injection of antigen solution. Here, the RIU increases as the Ag binds to the Ab coupled to the surface. Note that at the end of the injection, the RIU remains stable, meaning the Ag is strongly bound to the Ab.

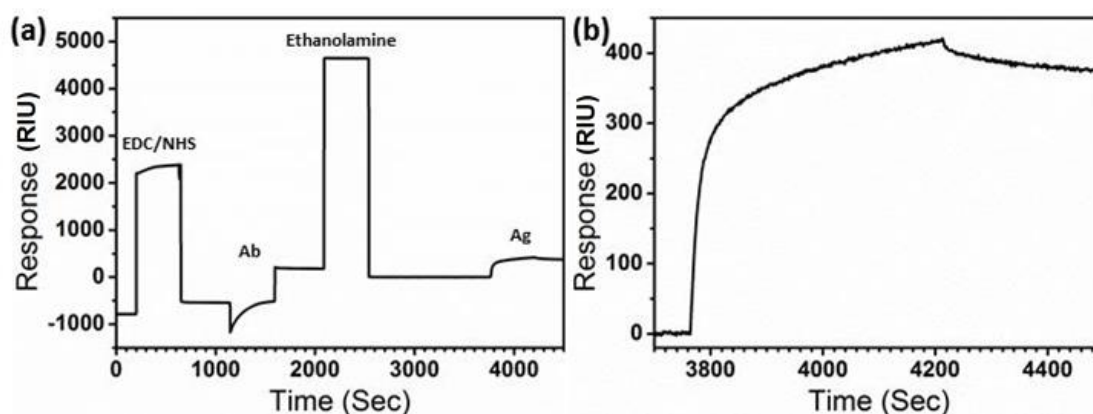


Figure 2.15: (a) Optimised assay carried out on a commercial SPR system. The flowrate was $25 \mu\text{l}/\text{min}$ and all injections were $200 \mu\text{l}$ (8 minute injections), with PBS as running buffer. First injection is 200 mM EDC & 25 nM NHS, second is $14 \mu\text{g}/\text{ml}$, murine monoclonal (mAb) anti human IgG antibody. Ethanolamine-HCl, pH 8.5 is used

to block the surface and finally 4 $\mu\text{g/ml}$ human IgG protein antigen is injected. (b) Close up of the Ag injection step.

Since the material is the same (Au in both cases), this assay can be transferred to the nanohole sample. Note however that, in this case, the sensor was not docked in a microfluidics cell and therefore injections were replaced, by a drop-on method and incubated. The transmission spectra were not recorded in real time but at the end of the different incubation/washing steps. Also, the commercial sensors were pre-coated with Mercaptohexadecanoic acid (MHDA), so an additional step of MDA SAM assembly was required to functionalise the surface for the nanoholes array.

2.3.6 Bio assay on nanohole array

Transmission spectra (acquired in PBS buffer) were taken after immobilization of each layer of biomolecules, and are shown in Figure 2.16(a). As can be seen, the dip redshifts after each step, confirming the binding at the surface of the functionalized sensor. The shifts at the different stages are reported in Table 2.2. There is a shift of 5.9 nm from the MDA monolayer to the primary antibody (14 $\mu\text{g/ml}$ human IgG whole molecule) and a further shift of 3.3 nm going from the antibody to the antigen (4 $\mu\text{g/ml}$ human IgG protein, whole molecule). This correlates with what would be expected based on the simulations and molecule size. Both the antibody and antigen molecules used in this assay are the same size, but as the antigen layer is further from the surface it has less of an effect on the spectral shift.

Table 2.2: Spectral positions of the resonance dip at the different steps of the assay. Also shown are the spectral shift after each step and molecule size

Step	Wavelength (nm)	Wavelength shift (nm)	Molecule Size (nm)
Au & MDA monolayer	633.9	0	1.3
Antibody Layer	639.8	5.9	16
Antigen Layer	643.1	3.3	16

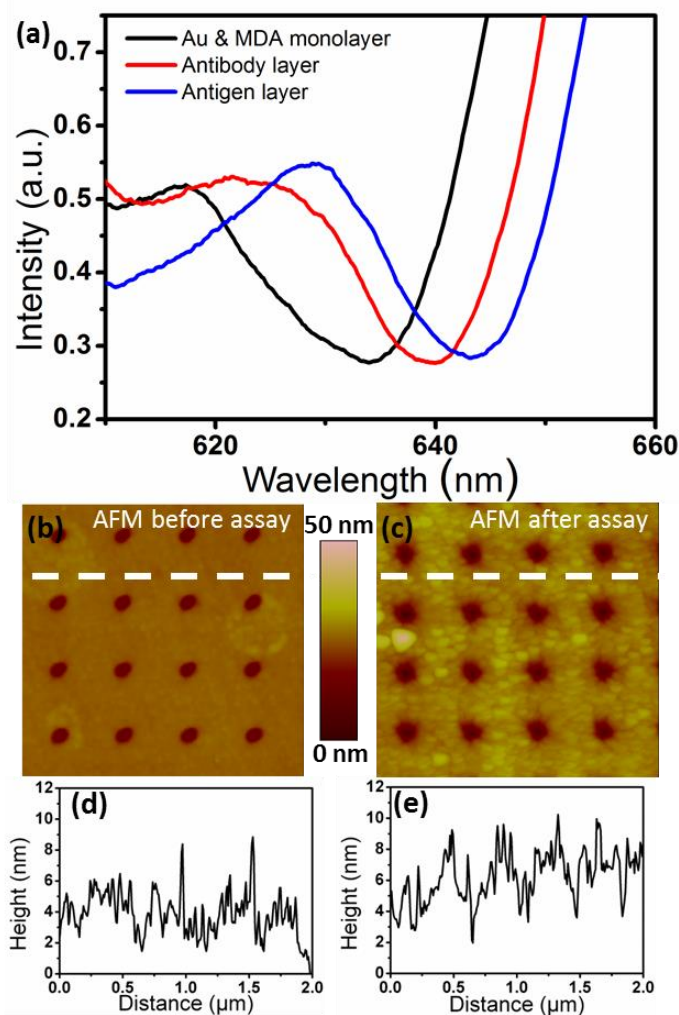


Figure 2.16: (a) shows the shift in spectra from the MDA monolayer (black) to the antibody attachment (red) and finally the Antigen (blue). (b) and (c) are AFM's of the array before and after the bio-assay. The height across the AFMs is shown underneath their respective images in (d) and (e).

In order to confirm the shifts were due to attachment of biomaterial at the surface of the sensors and not to other artefacts such as blocking of the holes by impurities or salts, AFM imaging (in air) was undertaken before and after the bio assay, see Figure 2.16 (b) and (c), respectively. The image before the assay shows a smooth surface. The AFM at the end of the experiment clearly shows the biomaterial was bound at the surface of the sensors, with no blockage of the nanoholes. The surface looks very rough with clumps of average size of 60 nm, suggesting a non-homogeneous coverage. It should be noted however that this AFM images were acquired in the dry where antibody/antigen complexes are known to crystallise [31, 32].

2.4 Summary and Conclusion

Nanohole arrays in thin Au films have been simulated, and then fabricated by FIB milling and assembled onto glass substrates. Following fabrication the nanoholes are characterised first using a Scanning Electron Microscope (SEM) and Optical Microscope to ensure there are no defects present after the lift off step. It was clear under the optical microscope when defects were present.

It was shown how altering the bulk refractive index (using salt water solutions) caused the spectra, in the region of interest, to shift to higher wavelengths. This response agreed with the 3D-FDTD simulations that were carried out.

A bioassay was developed using a commercial SPR system, along with the clean and attachment chemistry needed to transfer the assay to the nanohole array. The bio-sensing potential is examined by attaching a monolayer of MDA, antibody and antigen. There are measurable shifts from step to step showing the suitability of these fabricated nanohole arrays for use as biosensors.

2.5 References

- [1] R. Wang, S. Tombelli, M. Minunni, M. M. Spiriti, and M. Mascini, "Immobilisation of DNA probes for the development of SPR-based sensing," *Biosensors and Bioelectronics*, vol. 20, pp. 967-974, 2004.
- [2] A. N. Naimushin, S. D. Soelberg, D. K. Nguyen, L. Dunlap, D. Bartholomew, J. Elkind, *et al.*, "Detection of Staphylococcus aureus enterotoxin B at femtomolar levels with a miniature integrated two-channel surface plasmon resonance (SPR) sensor," *Biosensors and Bioelectronics*, vol. 17, pp. 573-584, 2002.
- [3] A. D. Taylor, J. Ladd, Q. Yu, S. Chen, J. Homola, and S. Jiang, "Quantitative and simultaneous detection of four foodborne bacterial pathogens with a multi-channel SPR sensor," *Biosensors and Bioelectronics*, vol. 22, pp. 752-758, 2006.
- [4] M. Piliarik, L. Párová, and J. Homola, "High-throughput SPR sensor for food safety," *Biosensors and Bioelectronics*, vol. 24, pp. 1399-1404, 2009.
- [5] H. Bai, R. Wang, B. Hargis, H. Lu, and Y. Li, "A SPR aptasensor for detection of avian influenza virus H5N1," *Sensors*, vol. 12, pp. 12506-12518, 2012.
- [6] C. J. Murphy, "Peer reviewed: optical sensing with quantum dots," *Analytical Chemistry*, vol. 74, pp. 520 A-526 A, 2002.
- [7] A. Yalcin, K. C. Popat, J. C. Aldridge, T. A. Desai, J. Hryniewicz, N. Chbouki, *et al.*, "Optical sensing of biomolecules using microring resonators," *Selected Topics in Quantum Electronics, IEEE Journal of*, vol. 12, pp. 148-155, 2006.
- [8] G. Zheng, F. Patolsky, Y. Cui, W. U. Wang, and C. M. Lieber, "Multiplexed electrical detection of cancer markers with nanowire sensor arrays," *Nature biotechnology*, vol. 23, pp. 1294-1301, 2005.
- [9] P. Xie, Q. Xiong, Y. Fang, Q. Qing, and C. M. Lieber, "Local electrical potential detection of DNA by nanowire-nanopore sensors," *Nature nanotechnology*, vol. 7, pp. 119-125, 2012.
- [10] J. Wang, "Nanomaterial-based electrochemical biosensors," *Analyst*, vol. 130, pp. 421-426, 2005.

- [11] K. Dawson, A. I. Wahl, R. Murphy, and A. O’Riordan, "Electroanalysis at single gold nanowire electrodes," *The Journal of Physical Chemistry C*, vol. 116, pp. 14665-14673, 2012.
- [12] T. W. Ebbesen, H. Lezec, H. Ghaemi, T. Thio, and P. Wolff, "Extraordinary optical transmission through sub-wavelength hole arrays," *Nature*, vol. 391, pp. 667-669, 1998.
- [13] A. G. Brolo, R. Gordon, B. Leathem, and K. L. Kavanagh, "Surface plasmon sensor based on the enhanced light transmission through arrays of nanoholes in gold films," *Langmuir*, vol. 20, pp. 4813-4815, 2004.
- [14] J. N. Anker, W. P. Hall, O. Lyandres, N. C. Shah, J. Zhao, and R. P. Van Duyne, "Biosensing with plasmonic nanosensors," *Nature materials*, vol. 7, pp. 442-453, 2008.
- [15] D. Gao, W. Chen, A. Mulchandani, and J. S. Schultz, "Detection of tumor markers based on extinction spectra of visible light passing through gold nanoholes," *Applied physics letters*, vol. 90, p. 073901, 2007.
- [16] J. S. Kee, S. Y. Lim, A. P. Perera, Y. Zhang, and M. K. Park, "Plasmonic nanohole arrays for monitoring growth of bacteria and antibiotic susceptibility test," *Sensors and Actuators B: Chemical*, vol. 182, pp. 576-583, 2013.
- [17] C. Escobedo, "On-chip nanohole array based sensing: a review," *Lab on a Chip*, vol. 13, pp. 2445-2463, 2013.
- [18] N. C. Lindquist, P. Nagpal, K. M. McPeak, D. J. Norris, and S.-H. Oh, "Engineering metallic nanostructures for plasmonics and nanophotonics," *Reports on progress in physics. Physical Society (Great Britain)*, vol. 75, p. 036501, 2012.
- [19] J. Zhou and G. Yang, "Focused ion-beam based nanohole modeling, simulation, fabrication, and application," *Journal of manufacturing science and engineering*, vol. 132, p. 011005, 2010.
- [20] N. C. Lindquist, M. A. Turner, and B. P. Heppner, "Template fabricated plasmonic nanoholes on analyte-sensitive substrates for real-time vapor sensing," *RSC Advances*, vol. 4, pp. 15115-15121, 2014.

- [21] T. W. Odom, V. R. Thalladi, J. C. Love, and G. M. Whitesides, "Generation of 30-50 nm structures using easily fabricated, composite PDMS masks," *Journal of the American Chemical Society*, vol. 124, pp. 12112-12113, 2002.
- [22] H. Im, S. H. Lee, N. J. Wittenberg, T. W. Johnson, N. C. Lindquist, P. Nagpal, *et al.*, "Template-stripped smooth Ag nanohole arrays with silica shells for surface plasmon resonance biosensing," *ACS nano*, vol. 5, pp. 6244-6253, 2011.
- [23] R. Gordon, M. Hughes, B. Leathem, K. Kavanagh, and A. Brolo, "Basis and lattice polarization mechanisms for light transmission through nanohole arrays in a metal film," *Nano letters*, vol. 5, pp. 1243-1246, 2005.
- [24] H. Ghaemi, T. Thio, D. e. a. Grupp, T. W. Ebbesen, and H. Lezec, "Surface plasmons enhance optical transmission through subwavelength holes," *Physical Review B*, vol. 58, p. 6779, 1998.
- [25] S. A. Maier, *Plasmonics: Fundamentals and Applications: Fundamentals and Applications*: Springer, 2007.
- [26] H. Gao, J. McMahon, M. Lee, J. Henzie, S. Gray, G. Schatz, *et al.*, "Rayleigh anomaly-surface plasmon polariton resonances in palladium and gold subwavelength hole arrays," *Optics express*, vol. 17, pp. 2334-2340, 2009.
- [27] P. Lovera, D. Jones, B. Corbett, and A. O'Riordan, "Polarization tunable transmission through plasmonic arrays of elliptical nanopores," *Optics express*, vol. 20, pp. 25325-25332, 2012.
- [28] E. M. Hicks, X. Zhang, S. Zou, O. Lyandres, K. G. Spears, G. C. Schatz, *et al.*, "Plasmonic properties of film over nanowell surfaces fabricated by nanosphere lithography," *The Journal of Physical Chemistry B*, vol. 109, pp. 22351-22358, 2005.
- [29] K.-L. Lee, W.-S. Wang, and P.-K. Wei, "Comparisons of surface plasmon sensitivities in periodic gold nanostructures," *Plasmonics*, vol. 3, pp. 119-125, 2008.
- [30] http://www.sierrasensors.com/index.php?option=com_content&task=view&id=68&Itemid=102.

[31] O. Ouerghi, A. Touhami, A. Othmane, H. Ben Ouada, C. Martelet, C. Fretigny, *et al.*, "Investigating specific antigen/antibody binding with the atomic force microscope," *Biomolecular engineering*, vol. 19, pp. 183-188, 2002.

[32] A. Raab, W. Han, D. Badt, S. J. Smith-Gill, S. M. Lindsay, H. Schindler, *et al.*, "Antibody recognition imaging by force microscopy," *Nature biotechnology*, vol. 17, pp. 901-905, 1999.

Chapter 3

Development of a point of care platform for label-free, multiplexed, real-time detection of cancer biomarkers

3.1 Introduction

Plasmonic arrays of nanoholes have recently emerged as promising diagnostic tools, for example, to detect infectious diseases and cancer [1, 2]. Their small footprint, multiplexing capabilities, ease of integration and potential low-cost fabrication make them extremely attractive for point of care, label-free sensing. For these reasons, nanohole array sensors have been extensively studied in the recent years. However, most of the work reported has focused on new fabrication methods [3-6], novel or improved functionalities [6-8] and/or detection of new biologically relevant molecules [9-11]. Less work has been devoted to their integration into dedicated optofluidic platform, which is essential for their commercial uptake. Also, most of the work reported so far has dealt with ideal and simple matrixes, i.e. pure antigen in buffer. For a diagnostics tool to be useful and validated, it has to provide reliable results with realistic, complex media, such as human serum.

In this chapter, we report on the integration of the nanohole array sensors developed in Chapter 2 into a custom built optofluidic platform and successfully demonstrate real-time detection, in serum, of pancreatic cancer biomarkers*. The different aspects of the diagnostic instrument - microfluidic delivery, optical readout, attachment chemistry and bioprobes - have been combined together and optimised in an iterative manner. The functionality of the C1q and C3 bioprobes (provided by external partners), together with their attachment chemistries, were assessed and optimised using a commercial SPR system. The optimised assays were transferred onto nanohole arrays and validated using a commercial microscope setup. In parallel, an integrated optofluidic platform was designed and implemented. The custom system allowed for individual addressing of the plasmonic arrays as well as real-time, multiplexed optical readout. The optimised assays were then transferred, and selective, real-time multiplexed detection of C1q and C3 antigens demonstrated in buffer. Finally, detection of C1q antibody in diluted human serum is successfully reported. This represents the first demonstration of real-time detection of cancer biomarkers in serum using nanohole array based sensors.

*This work has been prepared for publication as “A point of care platform for label-free, multiplexed, real-time detection of pancreatic cancer biomarkers”, *Biosensors & Bioelectronics*, in preparation

3.2 Experimental

Figure 3.1 shows 4 of the main aspects that have to be considered for a label-free platform. These include the microfluidic delivery to bring reagents and bio fluids at the surface of the sensor, the sensor chip itself for sensitive detection of target analyte, the bioprobes that have to exhibit high selectivity and sensitivity towards the target analyte as well as the optical readout system. Each of these has to be compatible with each other to be integrated successfully to achieve a working biosensor. Within the scope of this project, the different sub-components of the point of care system were developed and optimised in parallel. Multiple iterations of all these sub-parts were necessary to have a fully functional integrated platform.

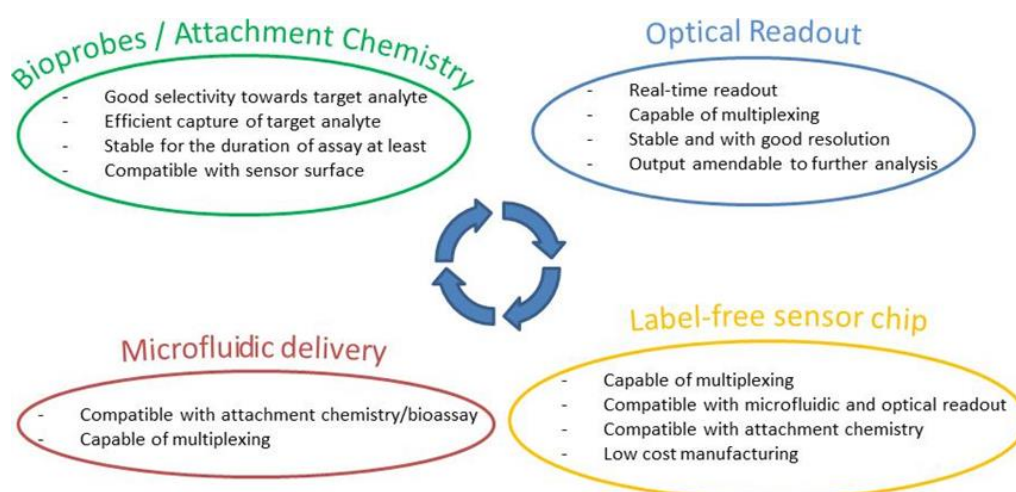


Figure 3.1: The main aspects for label free biosensing.

3.2.1 Fabrication of nanohole arrays

The nanohole arrays were fabricated using dual beam FIB as reported in Chapter 2. The same parameters and techniques were used to make identical nanohole sensors, which are used in this chapter.

3.2.2 Optical setups

3.2.2.1 Measuring intensity from direct transmission

In this system, shown in Figure 3.2, a light source was shone onto the sensors chip. The light from a 630nm LED (Roithner) or a 637 nm laser diode (L637P5, Oclaro), was collimated by a lens towards the sensors. The transmitted light was collected and

collimated by a 10 X objective (UPlanFL, 0.3 NA, Olympus) and then focused onto a CMOS colour camera (DCC1645C, Thorlabs). This allowed the recording of the intensity of the light transmitted through the arrays, using either a powermeter or CCD camera (and integrating the intensity over the array).

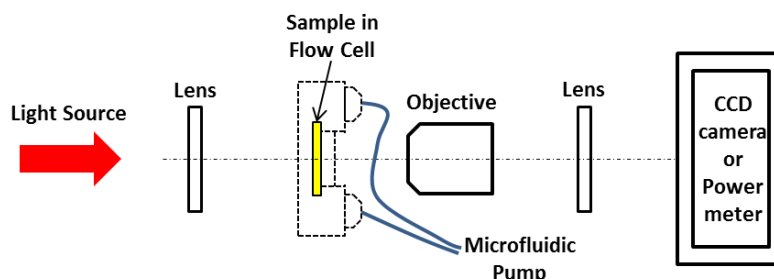


Figure 3.2: Schematic of the system to measure direct transmission

By using a LED or VCSEL light source where the wavelengths are at the location of the peak/dip in the nanohole array spectrum, it is possible to view only the intensity at the region where the shift occurs. This is illustrated in Figure 3.3, where it can be seen that the intensity where the light is being transmitted (the black peak), drops as the RI above the sensor changes from water (1.333) to 21% NaCl (1.37).

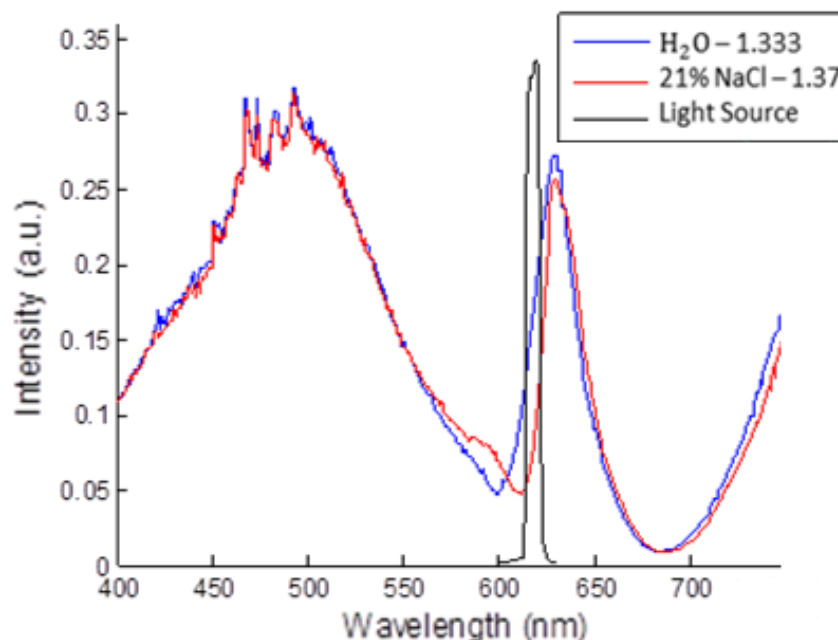


Figure 3.3: Transmission spectrum through a nanohole array in water (blue) and 21% salt solution (red). The intensity drops at the wavelengths being measured.

3.2.2.2 Measuring the spectrum from direct transmission

In this system, shown in Figure 3.4, a broadband source was guided into a guidewire (FOI-150-220, Schott) and passed through a ca 200 μm diameter pinhole to limit spatial coherence. Light from the pinhole passed through a frosted tape (Scotch) for homogenisation, and was collimated by a lens.

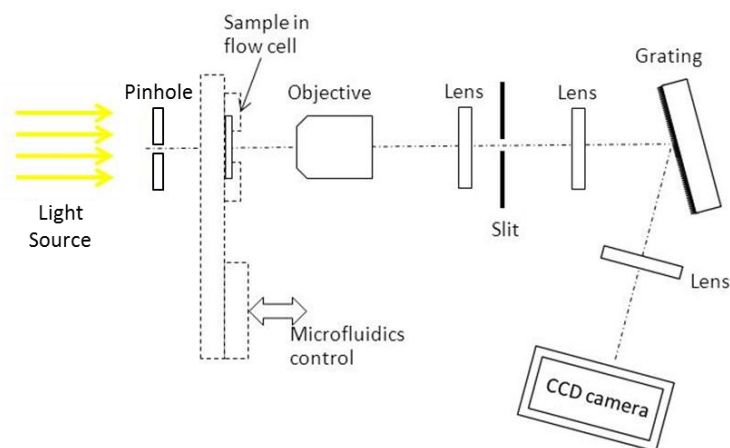


Figure 3.4: Schematic of the system to measure transmission spectra.

The visible part of the light could be passed through the microfluidics, see Figure 3.5 for the absorption spectrum of the material used to manufacture the microfluidic holder. The light transmitted through the sensors was collected and collimated by a 4X objective (UPlanFL, 0.13 NA, Olympus) and then focused onto a ca. 50 μm slit (Optosigma). The image through the slit was collimated by a lens, impinging onto a 1200 gr/mm grating (ER50-1208, Thorlabs) and the dispersed light, i.e. the transmission spectrum, was focused onto a CMOS camera (DCC1645C, Thorlabs).

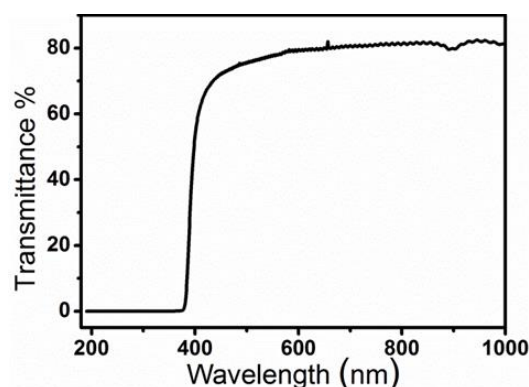


Figure 3.5: Transmittance through the microfluidic holder taken using a UV spectrometer. Approximately 80% of light above 400 nm passes through the holder.

3.2.3 Microfluidic delivery

3.2.3.1 Microfluidic setup

Figure 3.6(a) shows a photograph of the assembled setup provided by Sierra Sensors to Tyndall. Conventional syringe pumps and low pressure selection valves were used to drive the liquids. Software was developed to control the different components. It was designed to be able to address 4 sensor spots, on a sensor substrate, separately (or in combination). The technology is based on Sierra's Hydrodynamic isolation [9]. Briefly, a buffer solution runs from the top (main) inlet to the bottom outlet, with smaller inlets and outlets located above and below each sensor, see Figure 3.6(b). When a solution is injected through these inlets, it displaces the buffer so that only the solution injected flows above the targeted sensor.

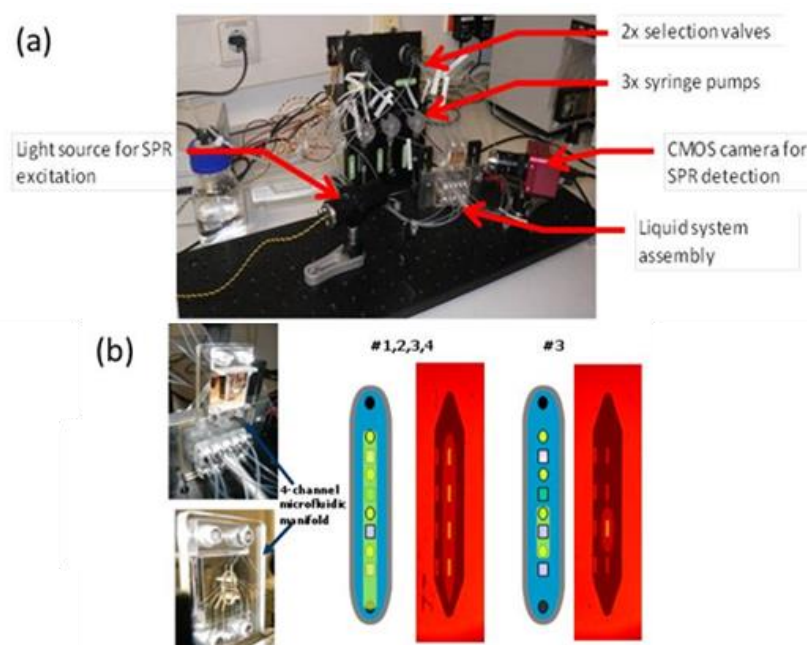


Figure 3.6: (a) Photograph of the assembled setup to evaluate the fluidics design, (b) Close-up photograph of flow cell / manifold assembly (left). SPR-images showing 2 different addressing schemes (spots 1,2,3&4 middle, spot 3 right)

Microfluidics function was first verified using SPR as an enabling technology by injecting solutions of different refractive indices. The running buffer used in Figure 3.6(b) was water with a refractive index of ~ 1.3 . To visualize the sample injection, a 2% NaCl solution was used which had a refractive index of about 0.02 higher. Through the SPR setup it has been possible to capture images showing the

injection pattern, and how both individual sensor spots and multiple sensors spots can be addressed.

3.2.3.2 Integration of microfluidics with nanohole sensors

The fabrication and use of a nanohole array as label-free sensor was successfully demonstrated and reported in Chapter 2. The same fabrication method was used to make sensor chips bearing 4 nanohole arrays sensors, with one array at each addressing spot. These sensors chips could be readily docked inside the microfluidics element provided by Sierra Sensors (amid slight modifications), see Figure 3.7. The microfluidic delivery system shown in this picture was able to address multiple arrays independently.

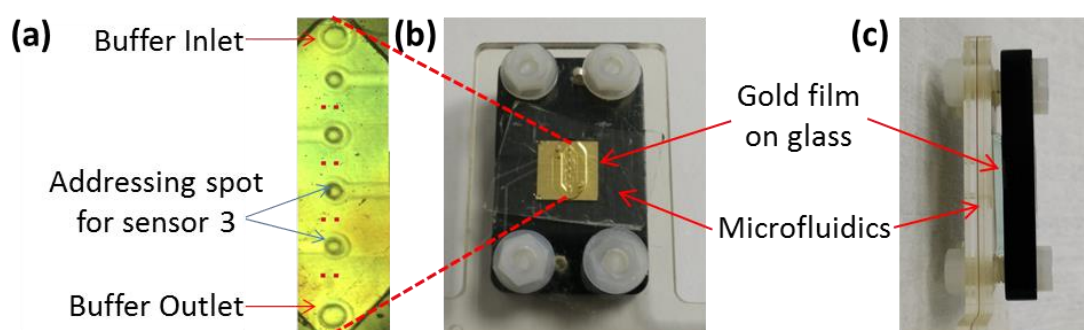


Figure 3.7: Gold film with nanohole arrays, loaded into the microfluidics holder, (a) shows the addressing spots/inlets/outlets. (b) and (c) the gold film with nanohole arrays in the microfluidic holder.

3.2.4 Assay procedures

The assays used in this chapter were performed on three differing platforms. The SPR 2 assays are carried out on the commercial SPR system, illustrated in Figure 3.8(a), where there is a real time measurement as the attachment steps are performed on the gold surface. The commercial SPR 2 was used to characterise the bioprobes and to optimise the assay parameters. Once developed, the assays were transferred to the nanohole array sensors. Assays undertaken using the microscope setup (described in Chapter 2, Section 2.2.6) are the microscope assays as the sample is measured using a simple cell, shown in Figure 3.8(b), and the bio attachments are performed using a drop-on method where the solution containing the biomolecules is placed on the nanohole array and left to incubate. These assays were carried out to check that the nanohole array sensors gave a

measurable shift in the spectrum when antibodies and antigen were bound to the gold surface. Finally, the third platform is the custom built setup, Figure 3.8(c), where the shifts from multiple nanohole arrays could be measured in real time.

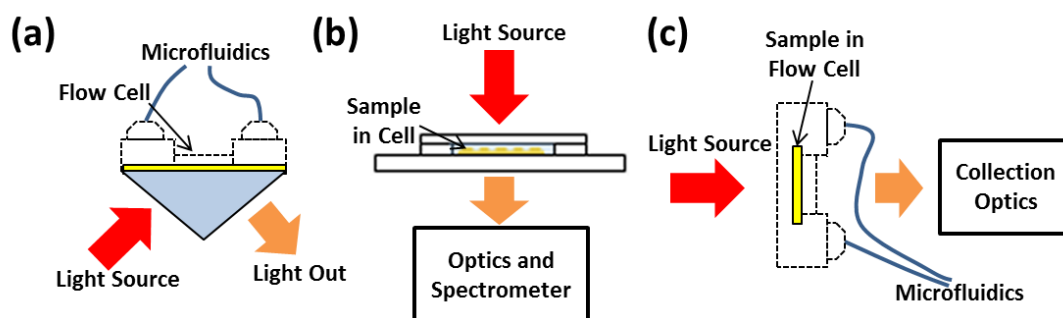


Figure 3.8: (a) SPR-2 schematic. (b) Microscope setup. (c) Custom built setup.

3.2.4.1 SPR-2 assays

The optimum parameters, including pH of the buffer, injection volume, flow rate and concentration of biomaterials were found using the SPR-2.

(i) Buffer assay

The following is the procedure of the optimised C1q assay with 0.1 M PBS (pH 7.2 – Sigma Aldrich) buffer running continuously and a flow rate of 20 $\mu\text{l}/\text{min}$. The commercial sensors (from Sierra) come pre-coated with Mercaptohexadecanoic acid (MHDA).

- a) Injection of 200 μl of 200 mM ethyl-(N',N'-dimethylamino)propylcarbodiimide hydrochloride (EDC) and 25 mM N-hydroxysulfosuccinimide (NHS) supplied by Sierra Sensors, GmbH, Hamburg to activate the carboxyl groups of the MHDA.
- b) Injection of 200 μl of a 20 $\mu\text{g}/\text{ml}$ C1q scFv Ab solution, provided by Lund University. The carboxyl groups react (after activation with EDC/NHS) with the amine group of the Ab to form a covalent (amide) bond.
- c) Injection of 100 μl of ethanolamine (Ethanolamine-HCl, 1 M, pH 8.5, Sierra Sensors) to prevent non-specific binding.
- d) Injection of 100 μl of a 4 $\mu\text{g}/\text{ml}$ C1q Ag solution, provided by Lund University.
- e) Regeneration with 10 μl 0.1M HCl (Sigma Aldrich).
- f) Repeat injection of the C1q Ag.

(ii) Serum assay

Same running buffer and flow rate.

- (a) Injection of 200 μ l EDC/NHS.
- (b) Injection of 200 μ l of a 20 μ g/ml C3 scFv Ab solution over sensor 1.
- (c) Injection of 200 μ l of a 20 μ g/ml C1q scFv Ab solution over sensor 2.
- (d) Injection of 100 μ l of ethanolamine.
- (e) Injection of 200 μ l of 5% human serum in PBS over both sensors.
- (f) Regeneration using 0.1M HCl

3.2.4.2 Assays on the microscope

In these experiments, the biomaterials were attached to the surface of the sensor by (drop on) incubation and not by microfluidic delivery. The duration of the different steps of the assay using this approach are longer than in the “real-time” experiment to allow time for the biomaterial to reach the surface (diffusion effect *vs.* dynamic delivery). Spectra in buffer were acquired after each step of the assay (before, after immobilisation of antibody and after binding of antigen – all after rinsing the sample with buffer solution). Assays were carried out using both biomaterials in pure buffer and in serum.

(i) Assays in buffer

The procedure for the C1q assay in buffer was,

- a) SAM assembly on the nanohole array with Mercaptododecanoic acid (MDA, 5 mM in 99% ethanol, Sigma Aldrich) for twenty four hours to functionalise the surface of the gold with carboxyl groups.
- b) Incubation of the sample in EDC/NHS for 30 minutes in order to activate the carboxyl groups on the surface. (EDC is 200 mM; NHS is 25 mM).
- c) C1q antibodies (Ab) were then attached to the surface of the sensors by incubating the sample with a 20 μ g/ml C1q scFv Ab solution for two hours. The sample was then washed in PBS buffer.
- d) The sample was then blocked for 30 minutes in ethanolamine to prevent nonspecific binding.

- e) The sample was then incubated for one hour and a half in a 4 $\mu\text{g/ml}$ solution of C1q antigen in PBS. The sample was once again washed in PBS.

To check the selectivity of the C1q antibody toward C1q antigen the nanohole arrays were functionalised with C1q antibody as before, steps a to d, with spectra recorded after each step. Following this, the sample was incubated for one hour and a half in a 4 $\mu\text{g/ml}$ solution of C3 protein, rinsed in PBS, and the spectrum recorded. The sample was then incubated in C1q (as in step e), and the spectrum taken.

(ii) Assay in Serum

Detection of C1q in serum was undertaken using the same microscope setup. Steps a to d, the functionalisation of the nanohole array with C1q Ab, is the same as in the previous assay. The sample was then incubated in 5% serum in PBS buffer for 1 hour, rinsed with PBS and the spectrum recorded.

3.2.4.3 Assays on the custom built system

The assays used in the microscope system were transferred to the custom built setup. This gave real time outputs of the spectrums of multiple arrays and measured slopes and intersection points. Assays were performed using both biomaterials in buffer and in serum with results obtained in 15 minutes.

(i) C1q assay in buffer

The sensor was first prepared by immersion in MDA for twenty four hours for SAM assembly. The sample was then loaded into the holder, where C1q antibody was attached to a nanohole array. The chemical and biological molecules used are the same as in the previous assays. The flow rate is 20 $\mu\text{l/min}$, and 0.1M PBS used as running buffer. The injections were,

- a) Injection of 60 μl EDC/NHS
- b) Injection of 60 μl C1q scFv Ab (20 $\mu\text{g/ml}$)
- c) Injection of 60 μl C1q Ag (4 $\mu\text{g/ml}$) over the two sensors

(ii) Assay in Serum

To test the sensing capability of the nanohole arrays to detect C1q antigen in serum the following assay was performed over an array, pre coated with MDA as before. The flow rate was 20 $\mu\text{l}/\text{min}$ and 0.1M PBS the running buffer

- a) Injection of 60 μl of EDC/NHS
- b) Injection of 60 μl of C1q scFv Ab (20 $\mu\text{g}/\text{ml}$)
- c) Injection of 25 μl of Ethanolamine-HCl (blocking step)
- d) Injection of 60 μl of 2% serum in PBS

(iii) Multiplexed assay

The same preparation, buffer and flowrate were used for the multiplexed assay. C1q antibody was attached to one nanohole array and C3 antibody to another. The procedure was,

- a) Injection of 60 μl EDC/NHS over both sensors.
- b) Injection of 60 μl C3 scFv Ab (20 $\mu\text{g}/\text{ml}$) onto sensor 2 only
- c) Injection of 60 μl C1q scFv Ab (20 $\mu\text{g}/\text{ml}$) onto sensor 1 only
- d) Injection of 60 μl C3 Ag (4 $\mu\text{g}/\text{ml}$) over the two sensors
- e) Injection of 60 μl C1q Ag (4 $\mu\text{g}/\text{ml}$) over the two sensors

3.3 Results and discussion

3.3.1 Selection and characterisation of bioprobes and assay development

3.3.1.1 Selection of biomarkers

C1q and C3 antibodies (shown in Figure 3.9), were selected by University of Lund (project partner) as relevant biomarkers for pancreatic cancer. The proteins C1q (complement 1q) and C3 (complement 3) are part of the complement system, which is part of the innate immune system. Disorders of the complement system are commonly associated with deficiencies of one or more of its proteins, which in the case of C3 deficiency can result in severe episodes of pneumonia, meningitis, peritonitis or sepsis [12, 13]. Most patients (>90%) with a C1q deficiency have systemic lupus erythematosus (SLE or lupus) [14, 15], in which the body's immune system attacks normal, healthy tissue.

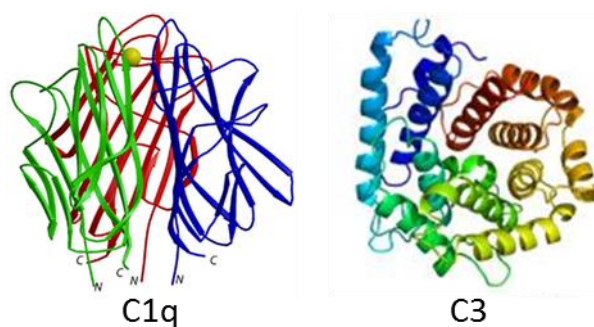


Figure 3.9: C1q and C3 proteins.

In some states of disease, C1q and C3 expression may be elevated [16, 17]. This is true for a number of cancers, for example, lung cancer and pancreatic cancer. Both C1q and C3 have significantly raised serum levels in patients diagnosed with pancreatic cancer, which makes them ideal candidates to be included in a panel of molecular biomarkers [18]. Until quite recent, most diagnostic tests have focused on single biomarkers. However, the use of panels of multiple biomarkers increases diagnosis sensitivity and specificity [19, 20].

3.3.1.2 Assay development on SPR2

Assays were developed and optimised (pH of buffer, injection volume, flow rate, concentration of antibody), using conventional SPR. Figure 3.10 shows the buffer pH optimisation for the C3 antibody clone selected. The first response is using a pH 4.5

buffer and shows the shift in RIU (~750) as it flows over the sensor surface. The decrease in RIU, just after 500 seconds, is the HCl regeneration step to clean the surface. The procedure is repeated with increasing buffer pH.

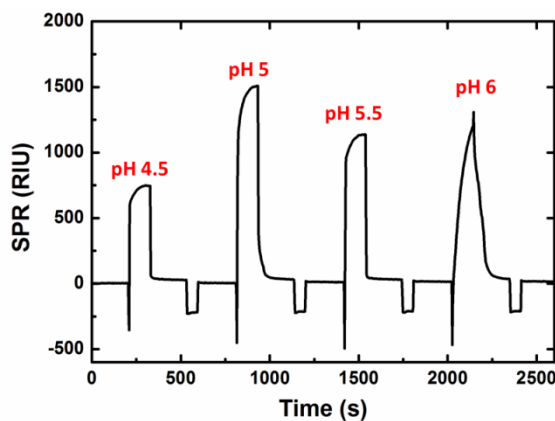


Figure 3.10: Optimisation of buffer pH for C3 Ab. Using buffers with pHs of 4.5, 5, 5.5 and 6 the C3 Ab is run for a minute over the sensor surface. The surface is regenerated using HCl between each injection.

As can be seen in Figure 3.10 the greatest response occurs for pH 5 buffer (~1500 RIU), showing that at this pH there is the greatest concentration of C3 antibodies at the sensor surface. Similar optimisations were performed for the injection volume, flow rate, pH of the C1q buffer and the concentrations of the antibodies and antigens.

3.3.1.3 Characterisation of bioprobes

Different clones of C1q and C3 scFv antibodies were provided by partners in Lund University and characterised (i.e., binding efficiency, selectivity in buffer and in serum, stability) in Tyndall using conventional SPR, and the best clones selected as bioprobes. Figure 3.11 shows the results from the best C1q and C3 clones received, which are the antibodies used in this chapter.

In the assay shown in Figure 3.11(a), C3 antibody was coupled to the sensor and after blocking with ethanolamine, 5% serum was injected. There is a steep curve at the initial injection point, which is caused by the high protein content in the solution (bulk shift), and also by the surface binding of the corresponding antigen to the antibody. At the end of injection, the curve falls sharply, due to the removal of unbound protein from the sensor surface, as well as the bulk solution returning to running buffer. After the

injection is completed, a new baseline is established indicating the level of antibody/antigen interaction.

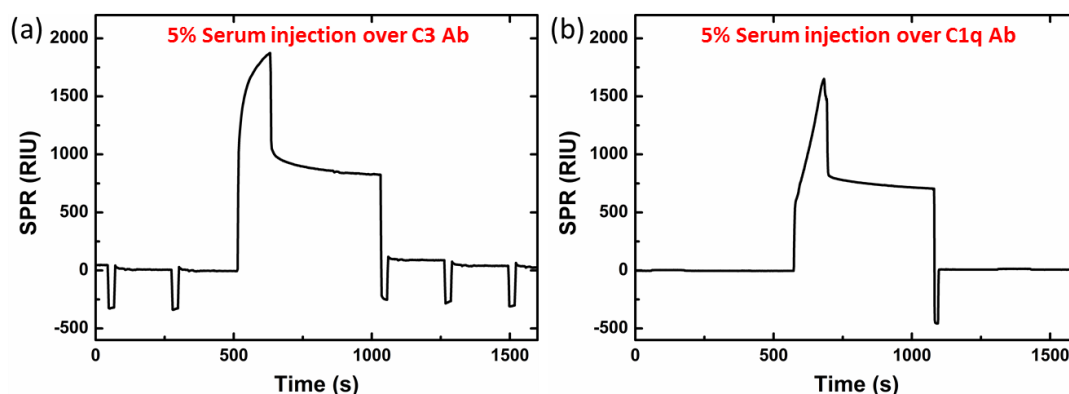


Figure 3.11: Selectivity of C1q and C3 scFv antibodies were tested with a mixed protein sample. 50 μl of 5% serum was run over both sensors for two minutes at 25 $\mu\text{l}/\text{min}$. Serum was diluted in PBS (pH 7) buffer. (a) shows the injection over C3 Ab. (b) Injection over C1q Ab.

Similarly, in Figure 3.11(b) 5% serum is injected over a sensor with C1q antibody and a similar response observed. These results show that the C1q and C3 clones used here have a high affinity for their target proteins, as there is a large RIU shift after the injection which remains over time. The surface is regenerated using HCl on both sensors to remove the bound protein and return the signal to the baseline.

Table 3.1: Molecular mass and size for C1q and C3 antibodies and antigen.

	C1q Ab (scFv)	C3Ab (scFv)	C1q Ag	C3 Ag
Mol. Mass. (kDa)	~27	~27	410	185
Size (nm)	~3	~3	~45	~20

Although in general, there is approximately 10 times the concentration of C3 compared to C1q in serum (C1q: $113 \pm 40 \mu\text{g}/\text{ml}$ [21], C3: 700 – 1800 $\mu\text{g}/\text{ml}$ [22]) the change in RIU observed is similar for the 5% Serum. One reason for this is the size of the molecules, as can be seen in Table 3.1, the C1q antigen is over twice the size of C3 antigen, so there is a greater RI change for each C1q bound. Also, there are a finite amount of available antibody binding sites on the surface, so it will saturate at a certain

point. The serum used was also from just one individual so the actual levels present are unknown.

3.3.1.4 Optimised assay

Figure 3.12(a) shows the optimised C1q assay in buffer, the details of which can be found in the experimental Section 3.2.4.1. From 130 to 610 seconds the EDC/NHS injection can be seen. Here, there is a large bulk increase in the response due to the refractive index of the solution, before a new baseline is established at 450 RIU after the carboxyl groups of the MHDA are activated by the EDC/NHS. The C1q Ab is then injected (840 – 1380 seconds), giving a bulk decrease during the injection due to the lower RI of the solution but rising to 510 RIU after the injection. The increase in the baseline RIU, from 450 to 510, shows the C1q Ab has attached to the carboxyl groups. The large increase that occurs from 1525 to 1645 seconds is the ethanolamine injection, which is the blocking step to prevent non-specific binding, after which there is a new baseline of 375 RIU. C1q Ag in buffer is then injected over the sensor twice with a regeneration step in-between.

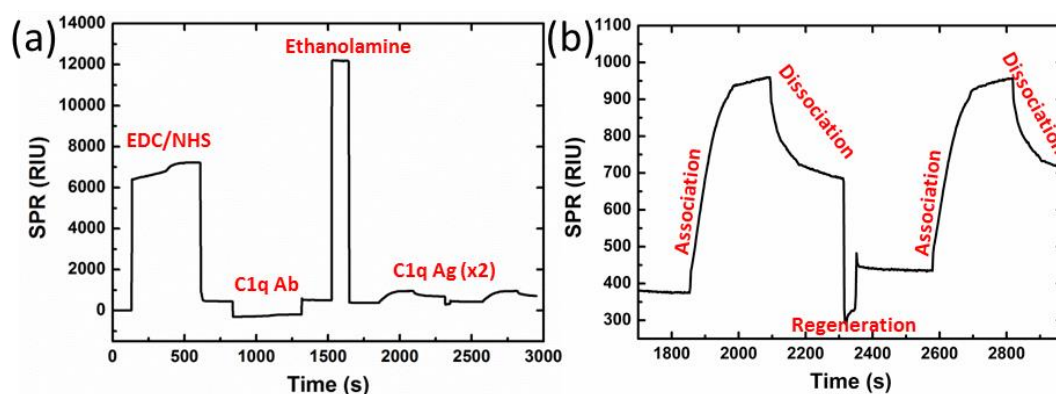


Figure 3.12: (a) Full C1q assay on the SPR2. (b) Zoomed in portion showing the antigen injections with the regeneration step in-between.

Figure 3.12(b) shows these injections. There is a steep curve for the first 130 seconds of the injection, where there is an increase in the RIU from 375 to 930. It tapers off as the antigen become saturated on the surface, reaching a value of 960 RIU at the end of the first injection (time = 2090 seconds). At the end of the injection, the decrease in the RIU (dissociation) shows the removal of unbound Ag from the sensor surface. The dip from 2310 – 2350 seconds is HCl regeneration of the surface to remove the antigen. The baseline after this (~435 RIU) is slightly higher than it was before the first antigen

injection, probably because not all of the antigen were removed. The second injection (starting at 2580 s) gives the same change as the first, with the RIU value again equal to 930 after the first 130 seconds and increasing to 957 by the end of the injection. This high association, and the low dissociation, indicates good affinity between the antibody/antigen interaction. The almost identical curve from the second antigen injection indicates a robust working assay with high repeatability.

3.3.2 Development of the optical readout platform

3.3.2.1 Optical designs

In nanohole array sensors, the binding of the target analyte (antigen) to the surface of the functionalised (i.e., antibody coated) sensor induces a change in the transmission spectrum through the sensor. More specifically, the binding induces a redshift of the transmission dip, located around 633 nm, on our nanohole array sensors. The induced changes can be monitored either by looking at the transmitted intensity at a specific wavelength and record its variation as the spectrum redshifts [23-25], or record the transmission spectrum and track the wavelength of the dip [7, 26-29].

(i) Direct transmission intensity setup

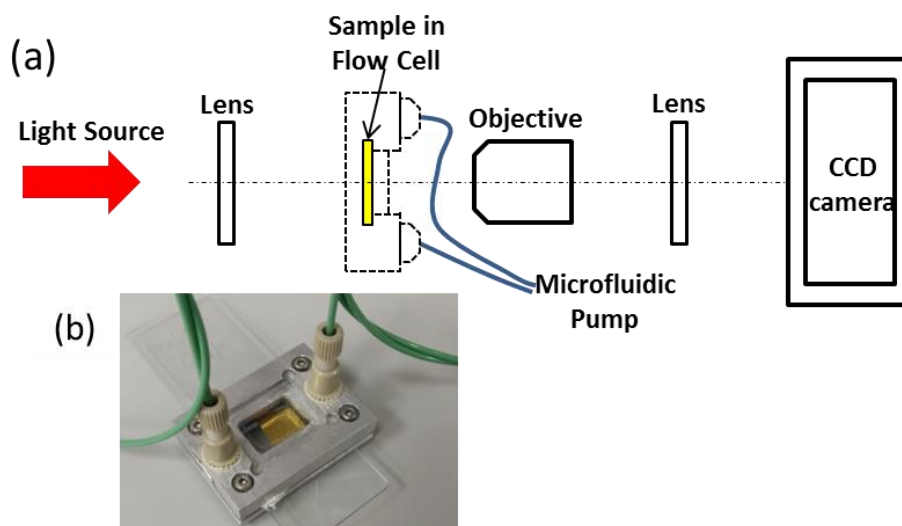


Figure 3.13: (a) Schematic of the setup. (b) The flowcell designed and built.

The first method was initially implemented, see Figure 3.13, (with both LED and laser VCSELS as light sources) due to its simplicity, but the obtained results were not satisfactory, as this method greatly relies upon the (intensity and spectral) stability of

the light source, and is therefore prone to false reading as it cannot distinguish between a change due to the binding of the target analyte or a change in the laser intensity. Figure 3.14(a) shows the results obtained using a powermeter to measure the intensity through a nanohole array, with solution of water and 21% NaCl flown over the sensor. The changes are visible, but only ~ 4 nW.

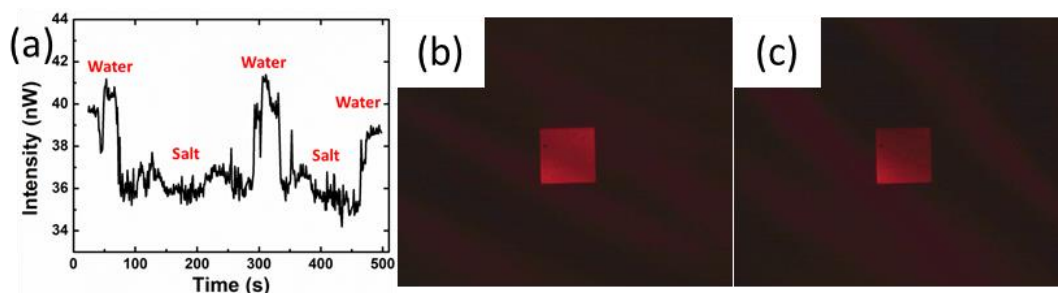


Figure 3.14: (a) Powermeter measurement of the intensity through the nanohole array with water and salt solutions. (b) and (c) CCD images showing the speckling and interference problems.

Also, in the case of VCSELs, this readout mechanism suffers from speckling and interference effects due to the monochromaticity of the laser source. Figure 3.14(b&c) shows the images captured less than 1 second apart, where the intensity measured through the array changes due to the speckling and interference effects. In addition, the large volume in the flowcell (Figure 3.13(b)) allowed mixing of the liquids in the cell making it unsuitable for use with biomolecules. To this end, work was ceased on this approach and a spectral detection method adopted with a microfluidic cell, described in Section 3.2.3.

(ii) Spectral detection setup

Figure 3.15 shows the alternative readout system which was designed (see Section 3.2.2.2) and implemented. In this system, a broadband source (white light or LED) was collimated and impinged onto the sensors chip, which removed the speckling and interference problems. The light passing through the slits was collimated onto a high resolution grating (1200 gr/mm) and focused onto a CMOS chip. This allowed the recording of transmission spectra through the sensors. Also, this design allowed the recording a wider spectral range and was therefore not affected by the intensity stability of the source. The wider spectral range allowed more metrics (minimum, absolute value, slopes before and after the dip) to be recorded, which might be advantageous for

post-processing analysis such as chemometrics. Last but not least, this readout system was fully compatible with the microfluidics subsystem and allowed multiplexing (up to three sensors simultaneously, but this can be readily scaled up). The footprint of the current version of the system is 30 by 10 cm².

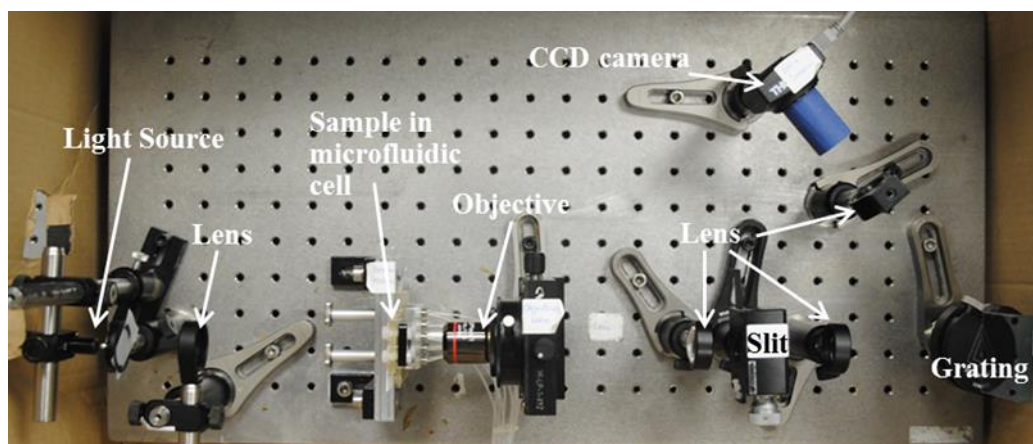


Figure 3.15: Image of the integrated optical/microfluidic system.

3.3.2.2 Spectral acquisition

In order to record the spectra, a LabVIEW program was designed to read the pixel intensity across a line, passing through the area of the image from the camera, corresponding to the sensor. To make sure the spectra were recorded through the sensors, direct imaging was carried out by using the grating in the 0th order, Figure 3.16(a).



Figure 3.16: (a) Direct imaging of the sensors. (b) Image of the dispersed light through the nanohole arrays. (c) Intensity plot of selected line, which is the transmission spectrum through the array.

Once it was ensured the image of the sensors was transmitted through the slits, the grating was rotated to disperse the transmitted light, with narrow band pass filters used

in order to rotate the grating to the required wavelengths. Figure 3.16(b) shows a typical image where the background is dark and the two lighter lines are the diffracted light from the gold nanohole arrays. The spectra through the sensors, shown in Figure 3.16(c), and more specifically the dip/peak could clearly be seen on the CMOS detector.

3.3.2.3 LabVIEW acquisition

The LabVIEW program was designed to take the data from the CMOS camera, captured using the setup described in Section 3.2.2.2, and display the transmission spectra through the sensors. The spatially separated spectra were acquired in real time using a dedicated LabVIEW program; see screenshot in Figure 3.17 and Appendix A5 for block diagram. An image from the CMOS camera was captured every 0.1 of a second.

Initially the local minimum point from the smoothed signal was the parameter used to detect changes in the signal but this proved unreliable as one small drop in intensity (due to noise or a faulty pixel) near the bottom of the dip caused the minimum to be ‘stuck’ at this value.

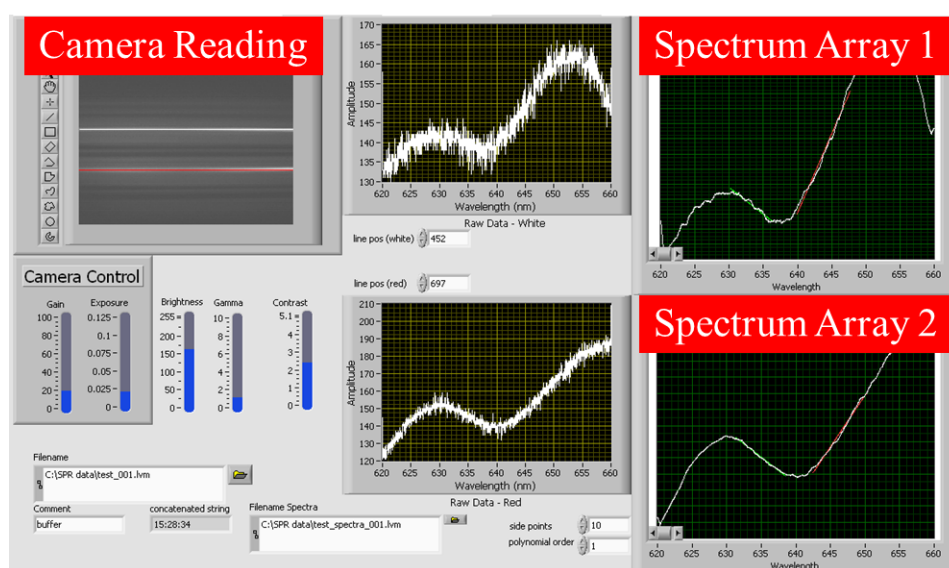


Figure 3.17: Screenshot of the front end of the LabVIEW program

To address the challenge, the slopes of the lines on either side of the dip and the intersection point of these lines were used. To calculate the slope of the line before and after the dip, the data from a certain region of the spectrum was taken and a linear fit performed on these data. The spectral regions before and after the dip were selected from the LabVIEW graphical user interface, and were overlaid on the spectrum to

ensure correct positioning. The intersection point of these two lines could then be calculated by the LabVIEW program and plotted in real time. As the dip in the spectrum shifts (due to a refracting index change) the slopes and intersection also changed. Figure 3.18(b) shows the intersection point plotted against time as the liquid flowing over the surface of a nanohole array is changed from PBS buffer (RI = 1.33) to IPA (RI = 1.377). As the IPA flows over the sensor, the dip, shown in Figure 3.18(a), red shifts do to the higher refractive index. This changes the slopes and therefore the intersection wavelength by approximately 10 nm, which corresponds well with the results obtained in Chapter 2 (Section 2.3.4) using the salt solutions, where there is a shift of ~ 12 nm for a similar change in refractive index.

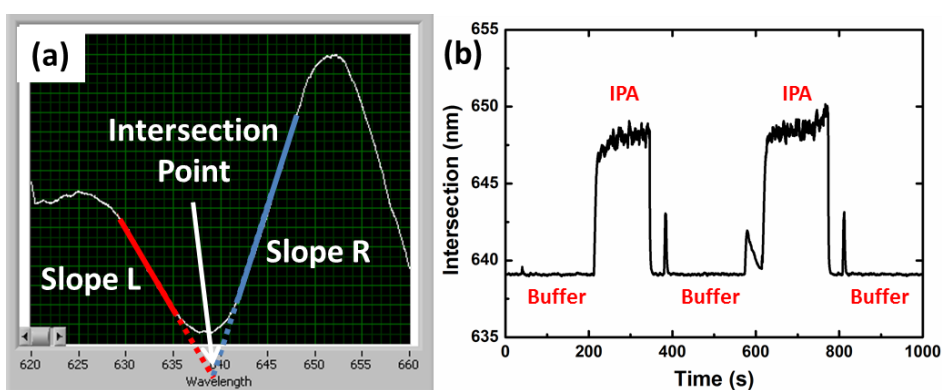


Figure 3.18: (a) spectrum with schematics to show where Slope and Intersection data are taken. (b) Intersection vs. Time for buffer to IPA shifts.

The entire process could be duplicated, taking another line on the CMOS camera to measure the spectra from two sensors simultaneously and can be up scaled to measure many more sensors. The slopes and intersection data were saved to a file with a data point every $1/10^{\text{th}}$ of a second. The spectra were also saved for further analysis. The slopes and intersections were displayed on the computer screen as time trace plots so that any change in the peak/dip caused by binding events could be seen in real time.

3.3.2.4 System resolution

In order to calibrate the system, a spectrum of a calibrated mercury lamp was recorded. Figure 3.19 shows the image recorded by the CMOS detector, as well as the pixel intensity across one line, *i.e.* the spectrum of the mercury lamp. The two peaks correspond to the doublet of the mercury and are located at 576.9 and 579 nm. As can be seen, the system can readily resolve this 2.1 nm gap. This gap corresponds to

65 pixels on the CMOS detector. This suggests a pixel corresponds to 0.03 nm, and the full spectral window of the detector is 41 nm (1280 pixels). The spectral resolution of the system was evaluated by measuring the width of one of the doublet. The full width at half maximum (FWHM) was 5 pixels, corresponding to 0.15 nm. The Rayleigh criterion of instrumental resolution specifies that two spectral features can be resolved provided their separation is as follows [30],

$$d \geq 0.849 \times FWHM \quad (3.1)$$

where d is the distance separating the two features. In the present case, $d = 0.13$ nm.

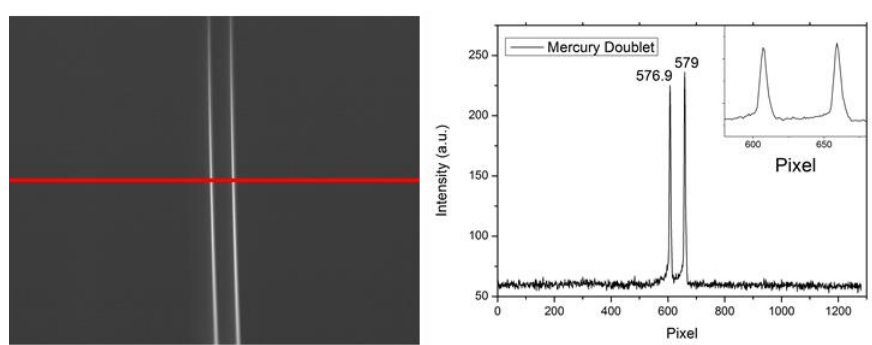


Figure 3.19 CMOS recording of the doublet line from a mercury lamp and right, corresponding intensity across the red line

However, while the designed system allowed real-time acquisition of transmission spectra, the spectra were found to be quite noisy. This was attributed to the inherent noise of the cost effective detector used. Furthermore, better quality spectra without loss of resolution could be obtained using time averaging and software smoothing based on a Savitzky-Golay algorithm [31]. Figure 3.20 shows the spectrum before and after the smoothing algorithms.

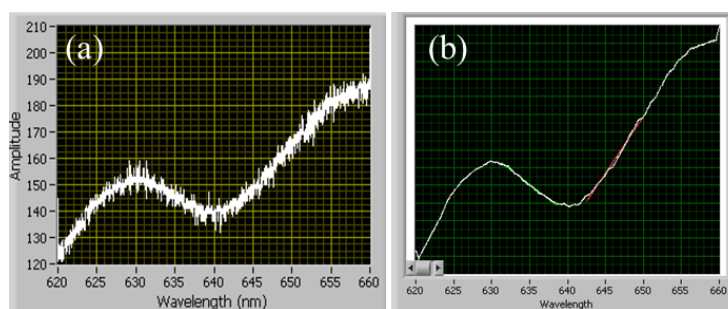


Figure 3.20 (a) before and (b) after time averaging and smoothing using the Savitzky-Golay algorithm, with a first order and 10 side points fit.

3.3.3 Assay experiments

The point of care platform was built and validated for bulk refractive index sensing experiment, see Section 3.3.2.3. Attachment chemistry and bio assays were developed for C1q and C3 biomarkers using the commercial SPR system with gold coated prism, Section 3.3.1. Integrating these two developments together would provide a prototype point of care device for early detection of pancreatic cancer biomarkers.

Since the plasmonic nanohole arrays are also made from gold, the assay and attachment chemistries developed on the commercial SPR system should be transferable to the nanohole array samples. However, in order to verify that the nanostructuring did not impede the label-free sensing capabilities of the nanohole sensors, assays were initially carried out using the same commercial microscope setup as used in Chapter 2.

3.3.3.1 Assays on the commercial microscope

(i) Assay with biomaterials in pure buffer

Figure 3.21(a) shows the C1q antibody and antigen in buffer assay described in Section 3.2.4.2. This demonstrates that label-free detection of C1q Ag is possible on the nanoholes samples.

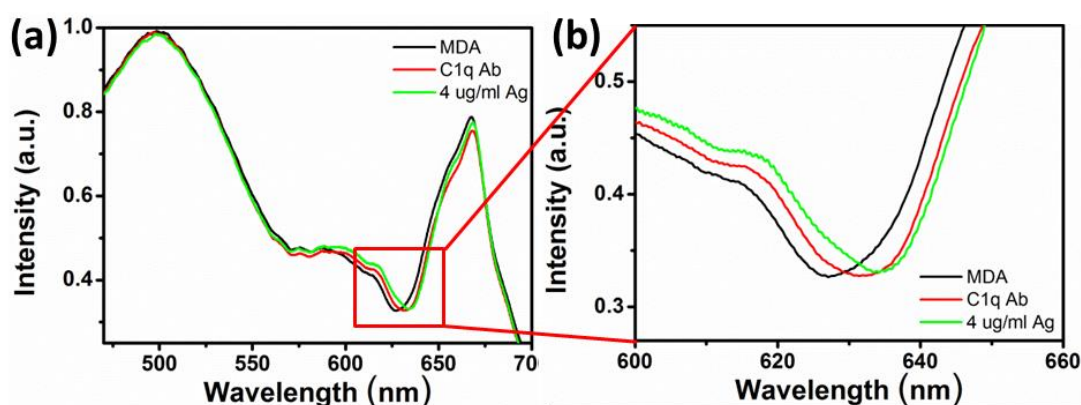


Figure 3.21: (a) Transmission spectra through a plasmonic sensor. The black line is the spectrum after MDA is attached, red is after C1q antibody immobilisation and green is after incubation of C1q antigen. (b) Zoomed in area showing the region of interest.

The sample was functionalised in MDA and the spectrum acquired, shown by the black curve shown in Figure 3.21. After incubation in EDC/NHS, and then in a 20 $\mu\text{g/ml}$

solution of the scFv C1q antibody, the red curve was recorded. The region where the shift is observed is shown in Figure 3.21(b), 600 nm to 660 nm. There is a red-shift of the resonance dip of 3 nm (from 628.2 nm to 631.2 nm), indicating the antibody has bound to the surface. The sample was blocked with ethanolamine to prevent non-specific binding and incubated in the 4 $\mu\text{g}/\text{ml}$ solution of C1q antigen. The recorded spectrum is shown in green in Figure 3.21. The spectral dip red shifted this time by further 2.7 nm (from 631.2 to 633.9 nm). Both the attachment of antibody and of antigen resulted in a spectral red-shift of the transmission dip around 630nm, which indicates successful detection of the molecules.

The selectivity of the sensor coated with C1q antibody toward a C1q target antigen was also assessed using the same setup. In this experiment, the nanohole arrays were functionalised with C1q antibody using the same procedure as reported in the previously. Figure 3.22(b) shows the dip red shifted by 3.2 nm after the C1q Ab immobilisation step. Following this, the sample was incubated in a 4 $\mu\text{g}/\text{ml}$ solution of C3 protein (non-complementary to C1q Ab). A spectrum was then recorded, see blue curve in Figure 3.22. As can be seen, no shift is observed strongly suggesting that C3 antigen did not attach to the surface of C1q antibody functionalised sensor. To verify the selectivity, the sample was then incubated in 4 $\mu\text{g}/\text{ml}$ C1q Ag as before, and the transmission spectrum reveals a redshift of 3 nm as expected, see green curve in Figure 3.22(b).

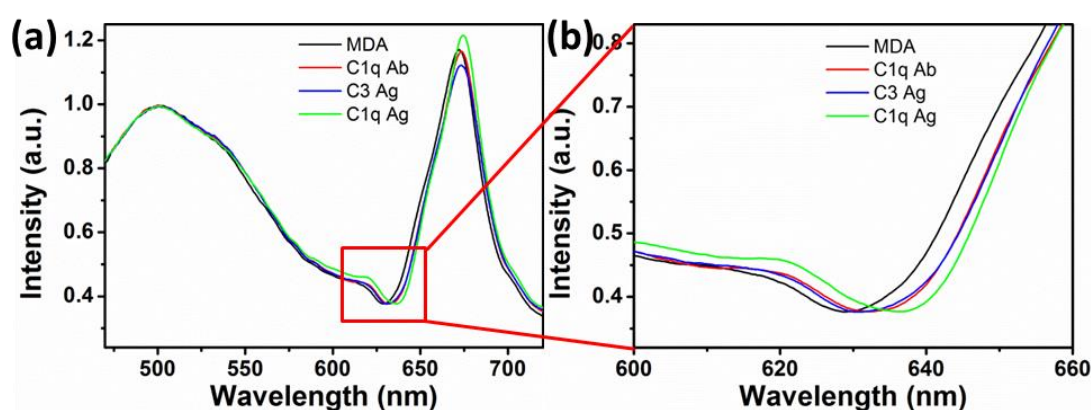


Figure 3.22: (a) Transmission spectra through a nanohole array showing selective detection of C1q antigen. The black line is the spectrum before bio-attachment, red is after antibody binding, blue is after incubation of C3 antigen, and green is after incubation of 4 $\mu\text{g}/\text{ml}$ C1q antigen. (b) Shows the spectra at the measured dip.

The detection of 4 $\mu\text{g/ml}$ solution of the C1q Ag (410 kDa) corresponds to detection of just under 10 nM. This is similar to reported levels of detection of similar biomaterials detected using nanohole array sensors, which range from 5nM to 80 nM [7, 32-34].

(ii) Assay using human serum

Having shown the nanohole sensors were able to detect C1q protein in buffer, the experiment was repeated, but using dilute serum instead of the antigen in buffer. The C1q Ab was attached as before, and the transmission spectra after the MDA attachment, and after the Ab shown in Figure 3.23 (MDA the black curve, C1q Ab the red curve). There is a shift in the dip from 636.7 nm for MDA to 639.2 nm for Ab (a 2.5 nm shift), which can be seen in Figure 3.23(b). The surface was blocked, and then incubated in 5% serum. The recorded transmission spectrum shows a redshift in the spectral dip to 641.7 nm, shown in green in Figure 3.23. This is a shift of 2.5 nm.

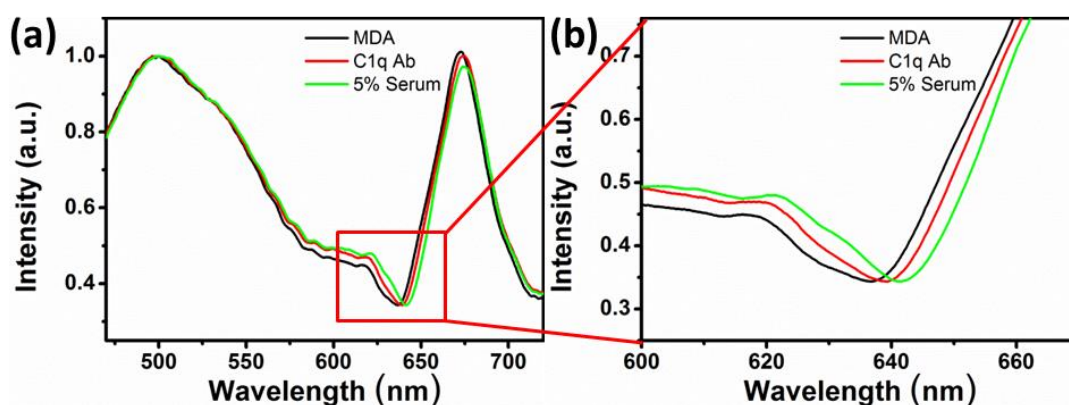


Figure 3.23: (a) Transmission spectra through a nanohole array showing detection of C1q in dilute serum. (b) Zoomed in at region of interest.

In order to confirm that it was indeed the C1q antigens that were binding to the C1q antibodies on the surface of the sensors, and that the spectral shift was not due to other molecules in the serum (i.e. non-specific binding), the assay was repeated, without the step to bind the antibody to the surface. As can be seen in Figure 3.24, no spectral shift was observed during this assay, confirming that C1q antibody was required in order to detect C1q Ag in serum. To our knowledge, detection of virus in calf serum [9] has been the only biomolecule detection reported in serum, using a nanohole array based sensor. We believe this is the first report of antibody/antigen detection in human serum.

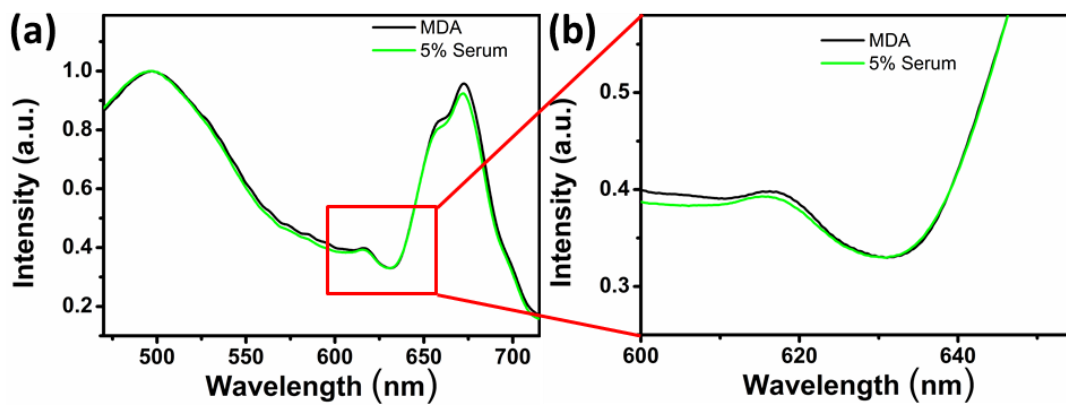


Figure 3.24: Assay showing Clq antibody is required to selectively bind Clq Ag from the serum at the surface of the sensor.

3.3.3.2 Real time assays

The previous section demonstrated that the attachment chemistry and the bioassay could be transferred onto the nanohole array samples. The optical setup used however did not allow real time monitoring nor multiplexing. In this section, we demonstrate that the whole assay can be carried out on multiple sensors and in real time using the developed readout platform. During the following experiments, both slopes on either side of the dip along with the intersection wavelengths were recorded. In different runs of the system, the changes were more visible by viewing one of the slopes and other times the intersection wavelength gave the best results. The parameter that gave the clearest results are plotted in the following assays.

(i) Real-time assay with biomaterials in buffer

The real time assay using C1q antibody and antigen described in Section 3.2.4.3(i) is shown in Figure 3.25. There is a big decrease in the slope as the EDC/NHS flows over the sensor, due to the large RI change. When the C1q Ab is injected there is a slight increase in the slope as the refractive index of the buffer containing the antibodies flows over the sensor. After the injection the Ab solution is replaced with buffer and the slope decreases, with a change before and after the Ab injection indicating the Ab have bound to the surface. C1q antigen in buffer (4 $\mu\text{g}/\text{ml}$) is then injected (at ~ 1700 s) and the slope decreases indicating the antigen has bound to the antibody.

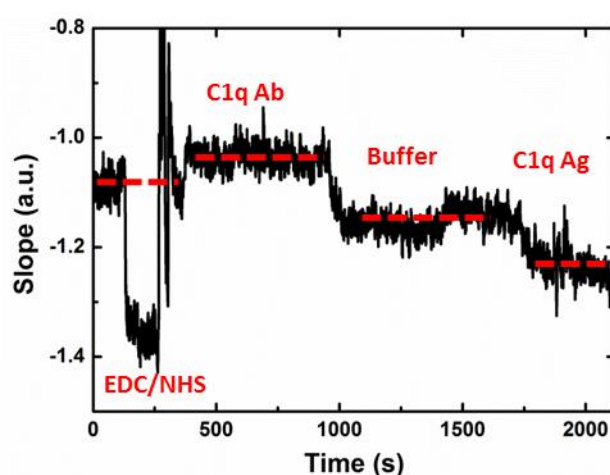


Figure 3.25: C1q antibody and antigen assay in buffer on custom built system. Red dashed lines are a guide only.

(ii) Real-time assay using human serum

Following demonstration of sensing using protein in pure buffer, experiments were carried out to test the sensing capabilities using a single serum sample. Figure 3.26 shows the assay described in Section 3.2.4.3(ii) where C1q Ab was attached to the sensor surface and serum injected over it. The EDC/NHS step can be clearly seen. Also, the value of the slope is slightly more negative after the C1q Ab injection than before it, indicating a successful attachment. The blocking step is a big decrease in the slope due to the bulk change (high RI liquid), and it returns to the previous baseline after. Finally, a clear decrease in the value of the slope can be seen upon injection of the 2% serum. This means the C1q protein in serum were able to bind to the C1q Ab present on the sensor surface. Human serum was used for this experiment, and therefore the detected concentration in C1q was unknown as it is a complex protein mixture.

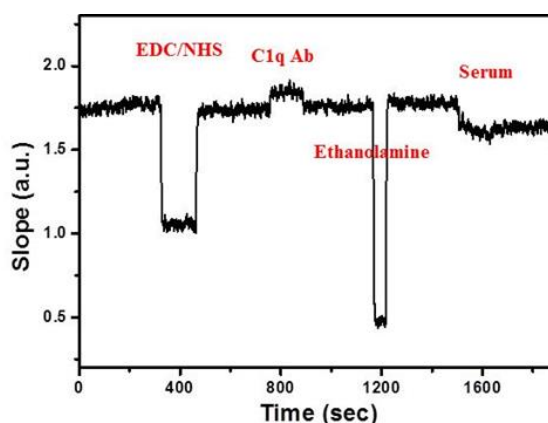


Figure 3.26: Assay on nanohole array sensor showing real time detection of C1q Ag in dilute serum.

To explore if non-specific binding was occurring, a similar assay was carried out without the antibody attachment step. Figure 3.27 shows this, where instead of an Ab injection there is an injection of acetate. A minimal change in the signal can be noticed when serum is injected in this case, showing that the antibody coating is necessary in order to observe a signal change, and also proves that the bioassay is working i.e. there is selective attachment of antigen to antibody. This demonstrates the first real time detection of biomolecules in serum, using nanohole arrays.

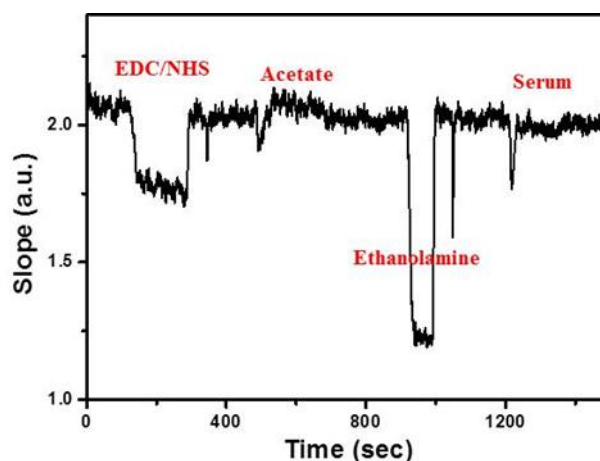


Figure 3.27: Assay without antibody attachment onto the sensor showing no non-specific binding.

(iii) Real time multiplexed assay

The results from the C1q and C3 multiplexed assay, described in the experimental Section 3.2.4.3(iii) are shown in Figure 3.28. It shows the intersection wavelengths from two sensors, measured simultaneously, as C3 and C1q antibodies and antigen are injected over the sensors. The first injection, highlighted with the blue band, is the EDC/NHS injection over both sensors, which shows a red shift in the wavelength due to the larger RI of the solution. The signal returns to the same baseline once the injection is complete. The next injection, at ~1000s, is C3 Ab injected over sensor 1 (the top panel, indicated with the stripped pink band). There is a ca. 0.15 nm redshift seen on this sensor. C1q Ab is then injected over sensor 2 (bottom panel, stripped green band) and a ca 0.1 nm redshift is noted for this sensor only. While this shift is lower than the spectral resolution of the instrument, the fact that a spectral shift is later observed when C1q antigens are introduced suggests that it is not an artefact. When the C3 antigen solution is flown over both sensors (indicated with the red band over both sensors), only sensor 1 shows a (slight) redshift of ~0.05nm. Finally, when C1q antigen is injected over the two sensors (the green band), sensor 2 only, shows a redshift of 0.25 nm. The lower shift observed in the case of C3 can be explained by the degradation of the C3 protein. It was later tested on the SPR-2 to check viability and was found to be degraded.

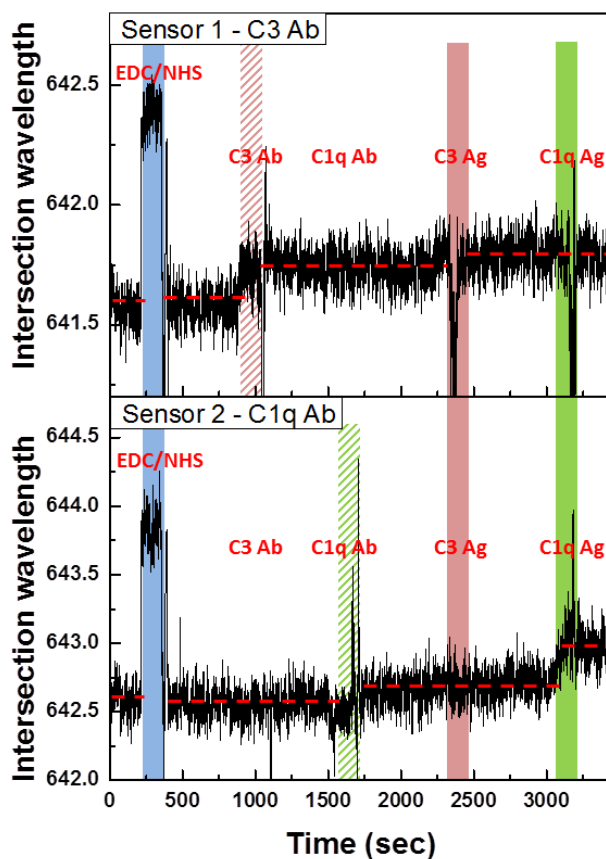


Figure 3.28: Sensorgram of the assay showing multiplexing and selectivity. The top panel relates to the C1q Ab functionalised nanohole array sensor while the bottom panel is for the C3 Ab functionalised sensor. Red dotted lines are guides for the eyes.

Compared to the microscope experiments, the spectral shifts measured were smaller. This could be due to limitations in the microfluidics used that did not allow long injections (i.e, the surface of the sensor was exposed to the antibody solutions for about three minutes which might not be a sufficient amount of time for enough coverage of the surface).

This experiment represents a successful real-time, multiplexed detection of 4 $\mu\text{g/ml}$ solutions of C1q and C3 antigen using the integrated system. It also demonstrates the selectivity of the antibodies towards their complementary antigens.

3.4 Summary and Conclusion

In this chapter, two optical setups to measure the light passing through a nanohole array were explored. The first that measured direct transmission did not give adequate results so the second setup was developed to measure the spectra. Custom software was developed using LabVIEW, to permit real-time data capture and readout. A novel approach was used, whereby both slopes and intercepts are used to measure the spectral shift of the resonant feature of interest, thereby eliminating any effects arising from scattering/absorption by the sample in the optical path.

This was integrated with a microfluidic setup to allow real time, multiplexed measurements. This setup was tested using solutions of buffer and IPA to ensure that changes in RI could be detected, and that individual arrays could be addressed independently.

Assays using two Ab/Ag (C1q and C3) in buffer, important biomarkers for the detection of pancreatic cancer, were developed and optimised using a commercial SPR. To ensure this assay would give measurable results on the nanoholes arrays, it was tested using the microscope setup. Red shifts were seen in the transmission spectrum after each stage of the assay, proving the nanohole arrays could be used to detect the C1q molecules. This was repeated using a serum sample, and this, too was detected. The blocking chemistry used was shown to be sufficient to prevent nonspecific binding of other proteins.

These assays were then carried out on the custom built system. The system permitted label-free detection of C1q antigen both in buffer and in human serum, in real-time, which is the first time this has been achieved using a nanohole array based sensor. Finally the two pancreatic cancer biomarkers in buffer were detected using a multiplexed setup.

3.5 References

- [1] J. N. Anker, W. P. Hall, O. Lyandres, N. C. Shah, J. Zhao, and R. P. Van Duyne, "Biosensing with plasmonic nanosensors," *Nature materials*, vol. 7, pp. 442-453, 2008.
- [2] A. G. Brolo, "Plasmonics for future biosensors," *Nature Photonics*, vol. 6, pp. 709-713, 2012.
- [3] H. Im, S. H. Lee, N. J. Wittenberg, T. W. Johnson, N. C. Lindquist, P. Nagpal, *et al.*, "Template-stripped smooth Ag nanohole arrays with silica shells for surface plasmon resonance biosensing," *ACS nano*, vol. 5, pp. 6244-6253, 2011.
- [4] B. Ai, Y. Yu, H. Möhwald, G. Zhang, and B. Yang, "Plasmonic films based on colloidal lithography," *Advances in colloid and interface science*, vol. 206, pp. 5-16, 2014.
- [5] Y. N. Kulchin, O. Vitrik, A. Kuchmizhak, A. Nepomnyashchii, A. Savchuk, A. Ionin, *et al.*, "Through nanohole formation in thin metallic film by single nanosecond laser pulses using optical dielectric apertureless probe," *Optics letters*, vol. 38, pp. 1452-1454, 2013.
- [6] A. A. Yanik, M. Huang, A. Artar, T.-Y. Chang, and H. Altug, "Integrated nanoplasmonic-nanofluidic biosensors with targeted delivery of analytes," *Applied physics letters*, vol. 96, p. 021101, 2010.
- [7] F. Eftekhari, C. Escobedo, J. Ferreira, X. Duan, E. M. Girotto, A. G. Brolo, *et al.*, "Nanoholes as nanochannels: flow-through plasmonic sensing," *Analytical chemistry*, vol. 81, pp. 4308-4311, 2009.
- [8] A. Barik, L. M. Otto, D. Yoo, J. Jose, T. W. Johnson, and S.-H. Oh, "Dielectrophoresis-enhanced plasmonic sensing with gold nanohole arrays," *Nano letters*, vol. 14, pp. 2006-2012, 2014.
- [9] A. A. Yanik, M. Huang, O. Kamohara, A. Artar, T. W. Geisbert, J. H. Connor, *et al.*, "An optofluidic nanoplasmonic biosensor for direct detection of live viruses from biological media," *Nano letters*, vol. 10, pp. 4962-4969, 2010.

- [10] H. Im, H. Shao, Y. I. Park, V. M. Peterson, C. M. Castro, R. Weissleder, *et al.*, "Label-free detection and molecular profiling of exosomes with a nano-plasmonic sensor," *Nature biotechnology*, vol. 32, pp. 490-495, 2014.
- [11] J. S. Kee, S. Y. Lim, A. P. Perera, Y. Zhang, and M. K. Park, "Plasmonic nanohole arrays for monitoring growth of bacteria and antibiotic susceptibility test," *Sensors and Actuators B: Chemical*, vol. 182, pp. 576-583, 2013.
- [12] <http://emedicine.medscape.com/article/136368-clinical#aw2aab6b3b2>.
- [13] S. Sethi and F. C. Fervenza, "Membranoproliferative glomerulonephritis—a new look at an old entity," *New England Journal of Medicine*, vol. 366, pp. 1119-1131, 2012.
- [14] J. Font, R. Cervera, G. Espinosa, L. Pallarés, M. Ramos-Casals, S. Jiménez, *et al.*, "Systemic lupus erythematosus (SLE) in childhood: analysis of clinical and immunological findings in 34 patients and comparison with SLE characteristics in adults," *Annals of the rheumatic diseases*, vol. 57, pp. 456-459, 1998.
- [15] C. Siegert, M. Daha, M. Westedt, E. Van Der Voort, and F. Breedveld, "IgG autoantibodies against C1q are correlated with nephritis, hypocomplementemia, and dsDNA antibodies in systemic lupus erythematosus," *The Journal of rheumatology*, vol. 18, pp. 230-234, 1991.
- [16] Y. Hong and B. Ghebrehiwet, "Effect of *Pseudomonas aeruginosa* elastase and alkaline protease on serum complement and isolated components C1q and C3," *Clinical immunology and immunopathology*, vol. 62, pp. 133-138, 1992.
- [17] R. Rossen, M. Reisberg, E. Hersh, and J. Gutterman, "The C1q binding test for soluble immune complexes: clinical correlations obtained in patients with cancer," *Journal of the National Cancer Institute*, vol. 58, pp. 1205-1215, 1977.
- [18] J. Chen, W. Wu, H. Tang, C. Zheng, Y. Xia, H. Zhou, *et al.*, "[Analysis of pancreatic cancer peripheral blood by comparative proteomics]," *Zhonghua wai ke za zhi [Chinese journal of surgery]*, vol. 51, pp. 62-65, 2013.

- [19] J. Li, Z. Zhang, J. Rosenzweig, Y. Y. Wang, and D. W. Chan, "Proteomics and bioinformatics approaches for identification of serum biomarkers to detect breast cancer," *Clinical chemistry*, vol. 48, pp. 1296-1304, 2002.
- [20] R. G. Moore, A. K. Brown, M. C. Miller, S. Skates, W. J. Allard, T. Verch, *et al.*, "The use of multiple novel tumor biomarkers for the detection of ovarian carcinoma in patients with a pelvic mass," *Gynecologic oncology*, vol. 108, pp. 402-408, 2008.
- [21] S. P. Dillon, A. D'Souza, B. T. Kurien, and R. H. Scofield, "Systemic lupus erythematosus and C1q: A quantitative ELISA for determining C1q levels in serum," *Biotechnology Journal*, vol. 4, pp. 1210-1214, 2009.
- [22] G. Széplaki, Z. Prohászka, J. Duba, S. Rugonfalvi-Kiss, I. Karádi, M. Kókai, *et al.*, "Association of high serum concentration of the third component of complement (C3) with pre-existing severe coronary artery disease and new vascular events in women," *Atherosclerosis*, vol. 177, pp. 383-389, 2004.
- [23] A. Lesuffleur, H. Im, N. C. Lindquist, K. S. Lim, and S.-H. Oh, "Laser-illuminated nanohole arrays for multiplex plasmonic microarray sensing," *Optics express*, vol. 16, pp. 219-224, 2008.
- [24] A. Blanchard-Dionne, L. Guyot, S. Patskovsky, R. Gordon, and M. Meunier, "Intensity based surface plasmon resonance sensor using a nanohole rectangular array," *Optics express*, vol. 19, pp. 15041-15046, 2011.
- [25] H. Im, A. Lesuffleur, N. C. Lindquist, and S.-H. Oh, "Plasmonic nanoholes in a multichannel microarray format for parallel kinetic assays and differential sensing," *Analytical chemistry*, vol. 81, pp. 2854-2859, 2009.
- [26] L. Pang, G. M. Hwang, B. Slutsky, and Y. Fainman, "Spectral sensitivity of two-dimensional nanohole array surface plasmon polariton resonance sensor," *Applied Physics Letters*, vol. 91, p. 123112, 2007.
- [27] J. C. Sharpe, J. S. Mitchell, L. Lin, N. Sedoglavich, and R. J. Blaikie, "Gold nanohole array substrates as immunobiosensors," *Analytical chemistry*, vol. 80, pp. 2244-2249, 2008.

- [28] A. Dhawan, M. D. Gerhold, and J. F. Muth, "Plasmonic structures based on subwavelength apertures for chemical and biological sensing applications," *Sensors Journal, IEEE*, vol. 8, pp. 942-950, 2008.
- [29] A. G. Brolo, R. Gordon, B. Leathem, and K. L. Kavanagh, "Surface plasmon sensor based on the enhanced light transmission through arrays of nanoholes in gold films," *Langmuir*, vol. 20, pp. 4813-4815, 2004.
- [30] D. Weinstein and M. R. Pérez, *Record of the IUE Three-Agency Coordination Meeting*, vol. D, p. 112, 1992.
- [31] C. Ruffin and R. King, "The analysis of hyperspectral data using Savitzky-Golay filtering-Theoretical basis (part 1)," in *Geoscience and Remote Sensing Symposium, Hamburg, Germany*, 1999.
- [32] H. Im, J. N. Sutherland, J. A. Maynard, and S.-H. Oh, "Nanohole-based surface plasmon resonance instruments with improved spectral resolution quantify a broad range of antibody-ligand binding kinetics," *Analytical chemistry*, vol. 84, pp. 1941-1947, 2012.
- [33] C. Escobedo, Y.-W. Chou, M. Rahman, X. Duan, R. Gordon, D. Sinton, *et al.*, "Quantification of ovarian cancer markers with integrated microfluidic concentration gradient and imaging nanohole surface plasmon resonance," *Analyst*, vol. 138, pp. 1450-1458, 2013.
- [34] P. Jia, H. Jiang, J. Sabarinathan, and J. Yang, "Plasmonic nanohole array sensors fabricated by template transfer with improved optical performance," *Nanotechnology*, vol. 24, p. 195501, 2013.

Chapter 4

**Arrays of anisotropic shaped nanoholes and
novel applications**

4.1 Introduction

The previous chapters have focused solely on circular nanoholes. During the fabrication of the circular nanoholes, using the FIB, it was seen that if the ion beam lost its focus, the shape of the hole was altered. Thus, by defocusing the beam it was possible to fabricate elliptical nanoholes where the size and shape could be controlled by how much the beam was defocused.

A benefit accruing from the use of non-circular nanohole arrays is that the shape anisotropy induces polarisation sensitive transmission spectra in both individual nanoholes and nanohole arrays [1-11]. Recently, it was shown that this polarisation could be used to tune the optical response in the visible spectral region when using arrays of crossed shaped nanoantennas, and that these devices had potential as encrypted tags for security application [12].

In this chapter, the polarisation dependence of light transmitted in both the visible and near infrared (NIR) through an array of elliptical nanoholes in a thin gold film self-assembled at a glass substrate is examined. A very strong spectral anisotropy was observed for spectra acquired using polarized excitation light along both the short and long axis of the ellipses showing distinct features, such as sharp peaks and spectral minima, in the 600-1200 nm regions. 3D Finite Difference Time Domain (FDTD) simulations suggested that the observed peaks were related to Fano resonances between the spectrally broad Localized Surface Plasmon (LSP) of the nanohole array and a sharp Rayleigh Anomaly (RA) on the Au/glass interface. Finally, the potential use of such sample as visible and NIR tag for anti-counterfeiting applications is demonstrated.

This work has been published as "Polarization tunable transmission through plasmonic arrays of elliptical nanopores," *Optics express*, vol. 20, pp. 25325-25332, 2012.

4.2 Experimental

4.2.1 Fabrication

Patches of $60\ \mu\text{m} \times 60\ \mu\text{m}$ periodic nanohole arrays were fabricated on thin films of chrome/gold (10 nm/50 nm) deposited on Si substrate using a focused ion beam (FIB). Elliptical nanoholes with dimensions of 150 nm for the minor axis and 350 nm for the major axis were fabricated with a lattice period of 450 nm. The gold film was released from the underlying Si substrate by wet etching the chromium layer (Chrome Etchant Lodyne, Grower Chemicals Ltd.) for 10 minutes. The chip was then immersed into deionized water. The Si substrate sank to the bottom while the Au film floated on the water surface due to surface tension. Using this approach, the highly fragile gold films were easily freed from the silicon substrate in a contactless manner. Finally, the nanostructured film was flow assembled onto a glass microscope slide and allowed to dry for 24 h. After assembly, the film was observed to adhere strongly to the glass substrate via Van Der Waals interactions.

4.2.2 Optical characterisation

Transmission spectra of the nanohole arrays in Au thin film were recorded using a home-built optical system, see Figure 4.1. The light from a Xe arc lamp was collimated by a combination of lenses, pinhole and slightly focused onto the sample. The angle of incidence of the beam was chosen to be 90° . The transmitted light (in zeroth-order diffraction) through the sample was collimated by a 50X objective (LMPlanFL, Olympus, n.a. 0.5)) and focused onto a collection fiber bundle connected to a Triax 190 0.19 metre monochromator (1200 lines / mm grating). Visible spectra were recorded at an integration time of 0.1 second using a R928 PMT (Hamamatsu Photonics). Infrared spectra were recorded at an integration time of 0.1 second using a nitrogen cooled germanium detector (EI-L, Edinburgh Instruments). All acquired spectra were divided by one obtained through the glass substrate. Analysis was performed using Jobin-Yvon's SpectRad software. A CMOS camera (DCC1645C, Thorlabs) was used to assure proper focusing on the nanohole array. Polarised measurements were performed by adding a Glan-Thomson polarizer (NT47-045, Edmund Optics Ltd.) in the incident and/or collection path. Polarisation bias of the optical setup was determined by taking spectra of a blank substrate with light polarized every 15° . No polarisation bias was observed.

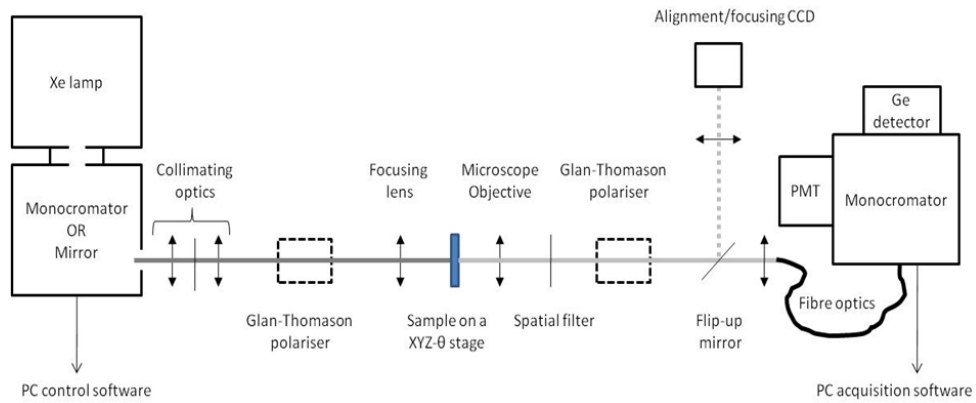


Figure 4.1: Schematic of the optical set-up used for measurements of transmission spectra of nanohole array in thin Au film.

4.2.3 FDTD simulations of nanohole arrays

3D-FDTD simulations were undertaken using JFDTD3D as described in Chapter 2 for the circular nanoholes. In the plane of the film, the elliptical nanohole was centered in the middle of the square ($x_0 = y_0 = 225 \times 10^{-9}$) and the equations used to define the ellipse were,

$$\frac{[(x_{pos} - x_0) + (y_{pos} - y_0)]^2}{(150 \times 10^{-9})^2} + \frac{[(x_{pos} - x_0) - (y_{pos} - y_0)]^2}{(350 \times 10^{-9})^2} \leq 1 \quad (4.1)$$

and

$$\frac{[(x_{pos} - x_0) - (y_{pos} - y_0)]^2}{(150 \times 10^{-9})^2} + \frac{[(x_{pos} - x_0) + (y_{pos} - y_0)]^2}{(350 \times 10^{-9})^2} \leq 1 \quad (4.2)$$

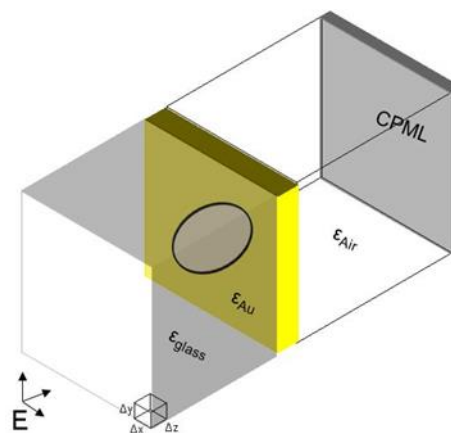


Figure 4.2: Computational domain used for the FDTD simulation

4.2.3.1 Transmission spectrum

In order to simulate the excitation source, a Gaussian damped sinusoidal pulse (having a frequency content of 1 to 6 eV) with a 45° polarisation was launched from the glass side and simulation run (for 200.10-15 sec) in the time domain. Total transmission spectra were obtained by Fourier transforming the simulated electric and magnetic fields on a surface above the holes and constructing the surface integral of the outward Poynting vector.

4.3 Results and discussion

4.3.1 Characterisation of the nanohole arrays

SEM and AFM were used to characterise the structure of the nanoholes. Figure 4.3(a) shows a scanning electron microscope image of an elliptical nanohole array fabricated using FIB in a thin gold film deposited on a Si substrate; inset, the surface of the film appears smooth and the edges of the nanohole sharp and well defined. Figure 4.3(b) shows an atomic force micrograph of a gold film bearing a nanohole array following its transfer by self-assembly onto a transparent substrate. As for the circular nanoholes described in Chapter 2 no defects could be seen.

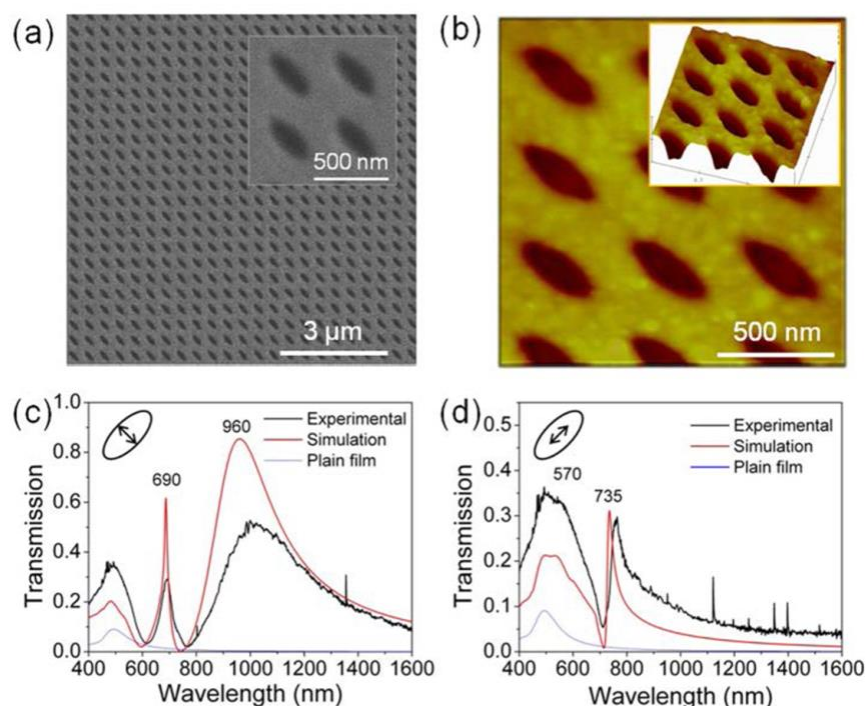


Figure 4.3: SEM (a) and AFM (b) micrographs of the array of elliptical nanoholes in a thin gold film. Insets: higher resolution image of four nanoholes Lattice period is 450 nm, nanohole dimensions are 350x150 nm with orientation angle of 45° with respect to the array edge. Measured (black curve) and FDTD simulated (red curve) far-field transmission spectrum with light polarised across (c) the short and (d) the long axis of the ellipses. Blue curves show the transmission spectrum through an un-patterned gold film.

To characterise the optical properties of these samples, polarised transmission spectra were recorded. Figure 4.3(c-d) show far-field transmission spectra with light polarized

across and along the long axis of the ellipses, respectively. Spectra recorded by illuminating at angles other than along the short or the long axis could be related to a linear combination of these two spectra, suggesting the observed anisotropy was dictated by the shape of the nanohole, and not by the symmetry of the repetition pattern as previously reported [3, 6, 13]. Also, a very good agreement between the simulated (red) and experimental (black) data, both in terms of peak position and overall trend was observed. The discrepancy in the relative intensity may be attributed to minor imperfections in the nanohole structure such as errors in hole dimension and sharpness of the hole edges or, to imperfections in the Drude-Lorentz model. All spectra exhibited a broad peak around $\lambda = 490 \text{ nm}$, with a transmission of 20-35% (simulation and experiment, respectively). This peak can also be found in the spectrum of a plain gold film and corresponds to direct transmission (intraband transition) for gold and occurs irrespective of the incident polarisation see Figure 4.3(c-d) [14]. However, at wavelengths above 490 nm the recorded spectra differ significantly for the two polarisation states.

When the incident light is polarized along the short axis of an ellipse, two peaks were observed (Figure 4.3(c)), a broad peak in the near infrared at $\lambda = 980 \text{ nm}$ and a sharp, asymmetric peak at $\lambda = 690 \text{ nm}$. On either side of this sharp peak, transmission reaches zero at $\lambda = 735 \text{ nm}$ and $\lambda = 595 \text{ nm}$. These dips in the transmission spectrum can be correlated to the $(1,0)_{\text{Glass}}$ and $(1,1)_{\text{Glass}}$ Surface Plasmon Polariton (SPP) mode on the glass/metal interface, respectively.

Table 4.1: Solutions to the SPP and RA equations predicting the spectral positions of Surface Plasmon Polariton and Rayleigh Anomaly on the glass/metal and metal/ air interfaces.

Surface Plasmon Polariton (SPP)		Rayleigh anomaly (RA)	
Order	Wavelength (nm)	Order	Wavelength (nm)
$(1,0)_{\text{air}}$	519	$(1,0)_{\text{air}}$	450
$(1,1)_{\text{air}}$	296	$(1,1)_{\text{air}}$	318
$(1,0)_{\text{Glass}}$	721	$(1,0)_{\text{Glass}}$	675
$(1,1)_{\text{Glass}}$	573	$(1,0)_{\text{Glass}}$	477

The solutions the equations to predict the SPP and RA (discussed in the previous chapters) are shown in Table 4.1. As can be seen in this table, the predicted $(1,0)_{Glass}$ and $(1,1)_{Glass}$ occur at 721 nm and 573 nm, respectively, in close proximity to the 735 nm and 595 nm dips observed. The peak at $\lambda = 690 \text{ nm}$ might also be associated with a Rayleigh anomaly. Rayleigh anomalies (RA) describe light waves diffracted to move in the plane of the surface [15]. As can be seen in Table 4.1, one can predict a $(1,0)_{Glass}$ RA at $\lambda = 675 \text{ nm}$, close to the $\lambda = 690 \text{ nm}$ peak.

When the incident light was polarized along the long axis of an ellipse, a shoulder at $\lambda = 570 \text{ nm}$ in the low energy side of the 490 nm peak and a very sharp, asymmetric peak at $\lambda = 735 \text{ nm}$ with an associated minimum at 715 nm was observed see Figure 4.3(d). This minimum value is in close spectral proximity to the expected $(1,1)$ RA. The unusual asymmetric shape of the $\lambda = 735 \text{ nm}$ peak is indicative of Fano resonance. Fano resonances are characteristic of systems where two transmission pathways interfere, a resonant and a non-resonant one, and have been observed in a variety of plasmonic nanostructures [16-19].

4.3.2 FDTD simulated near field profiles

To further understand the origins of the observed peaks, frequency-resolved near-field profiles were simulated at the wavelengths of interest. Top Panel Figure 4.4(a) shows the plan view of the electric field intensity at 960 nm distributed symmetrically along both edges of the long axis of an elliptical nanohole when irradiated with light polarized along the short axis. The observed symmetric dipole-like distribution with maximum intensities in the $(1, -1)$ direction corresponds to the transverse Localized Surface Plasmon (tLSP) resonance of the nanohole. Figure 4.4(a) bottom panel shows a side elevation view of the electric field distribution, which is observed to be bound and concentrated on the top and bottom surfaces of the nanohole.

Top Panel Figure 4.4(b) shows the plan view of the electric field intensity distribution at 690 nm along both edges of the long axis of an elliptical nanohole when irradiated with light polarized along the short axis. At this wavelength, the electric field is not bound to the rim of the nanohole anymore, but is instead concentrated in the area in between two

adjacent holes and is thus supported by the film, confirming its SPP nature as suggested previously.

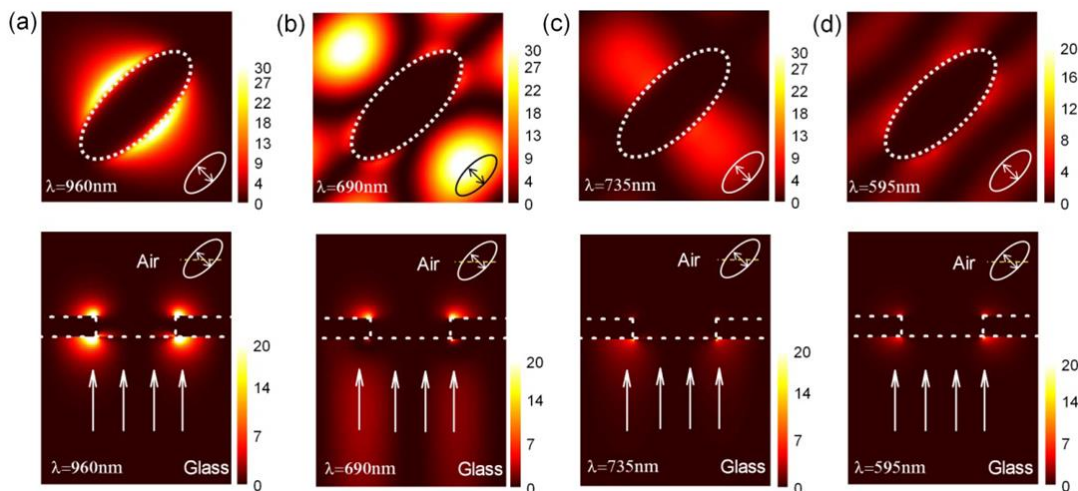


Figure 4.4: FDTD calculated frequency-resolved $|E_z|^2$ profiles at (a) $\lambda = 960$ nm, (b) $\lambda = 690$ nm (c) $\lambda = 735$ nm and (d) $\lambda = 595$ nm with incident light polarized along the short axis of the ellipses. Top panels show near field profiles 10 nm below the Au film and bottom shows cross section across the middle of the ellipses. The hole is centered at the origin, and the film boundaries are outlined in white.

While the excitation lies in the $(1, -1)$ direction, it excites the $(1, 0)_{Glass}$ SPP mode. This is possible because the electric field vector of the incident light has a component in the direction of SPP propagation, i.e., $E \cdot k_{SP} \neq 0$, with k_{SP} the wavevector of the SPP [20]. As the periodicity is the same in the x and y direction, both the $(1, 0)_{Glass}$ and the $(0, 1)_{Glass}$ modes are excited, explaining why the distribution is symmetric with respect to the long axis of the ellipse. The side elevation view of the electric field distribution (Figure 4.4(b)) clearly shows that the light is escaping into the substrate from the Au-glass interface, which is a signature of a Rayleigh anomaly [21]. The interference between the $(1, 0)_{Glass}$ SPP and the $(1, 0)$ Rayleigh anomaly then results in the Fano interference, characterized by the dip observed at 735 nm in Figure 4.3(c).

Figure 4.4(c) shows the electric field profile on the glass side at the minimum in transmission at 735 nm. In the top panel, it can be seen that the field profile possesses a hybrid character, being both localized to the rim of the ellipse and propagating along the interface in the $(1, -1)$ direction. This mode thus results from the combination of the tLSP of the nanohole and the $(1, 0)_{Glass}$ SPP at 690 nm.

The side elevation shows the intensity on the air/metal interface is very weak, suggesting there is a destructive interference between the tLSP and the $(1, 0)_{\text{Glass}}$ SPP at this wavelength [21, 22]. Also note that on the glass/metal interface, the electric field is also starting to escape from the metal film, marking the onset of the RA.

Finally, Figure 4.4(d) shows the electric field on the glass side at the second minimum at 595 nm. Here again, the distribution is hybrid, being both bound to the edge of the hole, corresponding to the tLSP and also propagating in the $(1, -1)$ direction, corresponding to the $(1, -1)_{\text{Glass}}$ SPP [23]. In a manner similar to the minimum at 735 nm, the field profile suggest a destructive interference between the tLSP and the $(1, -1)_{\text{Glass}}$ SPP.

Figure 4.5 shows, the electric field profiles, on the glass side, when irradiated with light polarized along the long axis. The top panel of Figure 4.5(a) shows the electric field profile at $\lambda = 735 \text{ nm}$ where a dipolar symmetric profile is observed with the maximum intensity in the $(1, 1)$ direction. This profile can be attributed to a combination of the longitudinal Localized Surface Plasmon (lLSP) resonance of the nanohole and the $(1, 0)_{\text{Glass}}$ SPP.

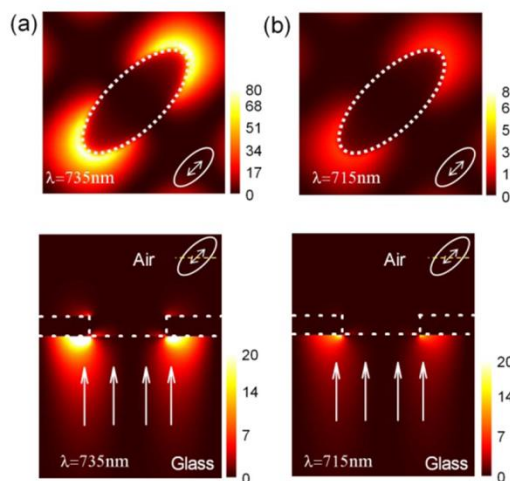


Figure 4.5: FDTD calculated frequency-resolved $|E_z|^2$ profiles at (a) $\lambda = 735 \text{ nm}$, (b) $\lambda = 715 \text{ nm}$ with incident light polarized along the long axis of the ellipses. Top panels show near field profiles 10 nm below the Au film and bottom shows cross section across the middle of the ellipses. The hole is centered at the origin, and the film boundaries are outlined in white.

As for the peak at 690 nm in Figure 4.5(b), the side elevation view of the electric field distribution of the bottom panel clearly shows that the light is escaping into the substrate from the Au-glass interface, suggesting a Rayleigh Anomaly.

The top panel (Figure 4.5(b)) also shows the profile at the minimum at $\lambda = 715 \text{ nm}$, which is similar, however a lot less intense, to the one at $\lambda = 735 \text{ nm}$. As in Figure 4.4(c), the side elevation shows the intensity on the air/metal interface is very weak, suggesting there is a destructive interference between the ILSP and the $(1, 0)_{\text{Glass}}$ SPP at this wavelength. Also note that on the glass/metal interface, the electric field is also starting to escape from the metal film, here again marking the onset of the RA.

4.3.3 Application as anti-counterfeiting tag

Polarized nanohole arrays have potential applicability for use in anti-counterfeiting applications, such as high end product labelling, drug packaging etc. Figure 4.6 demonstrates the concept of these devices where the ILSP and tLSP plasmon resonances have different frequencies in the visible and NIR regions of the spectrum. The CIE 1931 colour coordinates of the nanohole arrays measured for different polarisation angles exhibited different values ranging from (0.214, 0.306) to (0.317, 0.361).

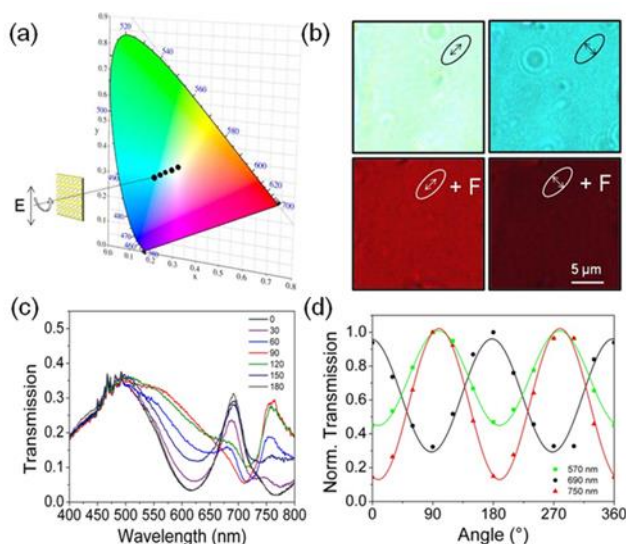


Figure 4.6: (a) illustration of the polarisation-dependant colour transmission with mapping of spectra to points on the CIE 1931 coordinates showing blue to white light tuning (b) Real colour transmission images showing dual visible-invisible tagging. Top: no filter and light polarised along (white) and across (blue) the long axis of the ellipse. Bottom: same images through 700 nm long path filters (c) Polarised transmission

spectra acquired every 30°. (d) Transmission intensity vs. polarisation angle for wavelength of 570, 690 and 750 nm. Solid lines are $\cos^2 \theta$ fit.

Real colour transmission images obtained using incident white light polarized along and across the long axis have been recorded, see Figure 4.6(b). The array appears white under polarisation along the long axis (CIE coordinate 0.317, 0.361) and turns to sky blue (CIE coordinate 0.214, 0.306) as the polarisation (or, conversely, the sample) is rotated by 90° such that light is polarized along the short axis. Under the same conditions, the image turns from bright to dark in the NIR observed when a 700 nm long path filter is placed in the optical path. This NIR spectral region is outside of the sensitivity of human eyes but may be resolved by a commercial CMOS camera. The inclusion of NIR spectral features adds a further level of security to an encrypted tag while the micron size of these arrays renders them difficult to see by the naked eye. Figure 4.6(c) and (d) show the measured polarisation dependence of the different plasmonic peaks. Spectra recorded by illuminating at angles other than along the short or the long axis could be related to a linear combination of these two spectra, suggesting the observed anisotropy was dictated by the shape of the nanohole, and not by the symmetry of the repetition pattern as previously reported [3, 6, 13]. The peaks at 570 nm and 750 nm are in phase and in quadrature with the 690 nm peak. When the polarisation of the incident light is parallel to the long axis, the ILSP intensity dominates and the tLSP is barely observable. In contrast, when the incident light is polarized parallel to the short axis the tLSP intensity dominates.

Simultaneously combining all these features (polarisation dependent visible and invisible transmission – simultaneous white/bright under one polarisation state and blue/dark by 90° rotation) in a security label would be quite unique and would be very challenging to illegally reproduce. Moreover, the transmission spectra could be further tuned by changing nanohole shapes, dimension or arrangement and metal used.

4.4 Summary and Conclusion

In summary, arrays of elliptical nanohole in thin gold films have been fabricated by focused ion beam milling and assembled onto a glass substrate. These samples showed strong optical anisotropy, and their transmission spectra showed sharp asymmetric features. Optical response of the samples was simulated by FDTD and a good agreement was found between the simulated and experimental data. Analysis of the simulated near-field profile suggested the observed peaks were related to Fano resonances between the $(\pm 1, 0)$ Surface Plasmon Polariton mode and the $(\pm 1, 0)$ Rayleigh Anomaly. Polarized transmission images acquired using commercial CMOS color chip showed simultaneous eye visible and eye invisible anisotropies. The optical signature of these arrays is quite unique and would be difficult to reproduce using other techniques, making them attractive for security tag applications.

4.5 References

- [1] Y. Alaverdyan, J. Alegret, M. K nll, and P. Johansson, "Shape effects in the localized surface plasmon resonance of single nanoholes in thin metal films," *Optics express*, vol. 16, pp. 5609-5616, 2008.
- [2] J. Elliott, I. I. Smolyaninov, N. I. Zheludev, and A. V. Zayats, "Polarization control of optical transmission of a periodic array of elliptical nanoholes in a metal film," *Optics letters*, vol. 29, pp. 1414-1416, 2004.
- [3] R. Gordon, A. Brolo, A. McKinnon, A. Rajora, B. Leathem, and K. Kavanagh, "Strong polarization in the optical transmission through elliptical nanohole arrays," *Physical review letters*, vol. 92, p. 037401, 2004.
- [4] K. K. Koerkamp, S. Enoch, F. Segerink, N. Van Hulst, and L. Kuipers, "Strong influence of hole shape on extraordinary transmission through periodic arrays of subwavelength holes," *Physical Review Letters*, vol. 92, p. 183901, 2004.
- [5] X.-F. Ren, P. Zhang, G.-P. Guo, Y.-F. Huang, Z.-W. Wang, and G.-C. Guo, "Polarization properties of subwavelength hole arrays consisting of rectangular holes," *Applied Physics B*, vol. 91, pp. 601-604, 2008.
- [6] A. Degiron and T. Ebbesen, "The role of localized surface plasmon modes in the enhanced transmission of periodic subwavelength apertures," *Journal of Optics A: Pure and Applied Optics*, vol. 7, p. S90, 2005.
- [7] K. Van der Molen, K. K. Koerkamp, S. Enoch, F. Segerink, N. Van Hulst, and L. Kuipers, "Role of shape and localized resonances in extraordinary transmission through periodic arrays of subwavelength holes: Experiment and theory," *Physical Review B*, vol. 72, p. 045421, 2005.
- [8] A. Degiron, H. Lezec, N. Yamamoto, and T. Ebbesen, "Optical transmission properties of a single subwavelength aperture in a real metal," *Optics Communications*, vol. 239, pp. 61-66, 2004.
- [9] J. Li, H. Iu, D. Lei, J. Wan, J. Xu, H. Ho, *et al.*, "Dependence of surface plasmon lifetimes on the hole size in two-dimensional metallic arrays," *Applied Physics Letters*, vol. 94, p. 183112, 2009.

- [10] X. Wang, H. Liu, H. Luo, W. Zhu, Z. Chen, J. Liu, *et al.*, "Optical filtering properties of subwavelength Tai-chi-shaped metal hole arrays," *Optics Communications*, 2014.
- [11] Y. Wang, Y. Qin, and Z. Zhang, "Extraordinary optical transmission property of X-Shaped plasmonic nanohole arrays," *Plasmonics*, vol. 9, pp. 203-207, 2014.
- [12] T. Ellenbogen, K. Seo, and K. B. Crozier, "Chromatic plasmonic polarizers for active visible color filtering and polarimetry," *Nano letters*, vol. 12, pp. 1026-1031, 2012.
- [13] R. Gordon, M. Hughes, B. Leathem, K. Kavanagh, and A. Brolo, "Basis and lattice polarization mechanisms for light transmission through nanohole arrays in a metal film," *Nano letters*, vol. 5, pp. 1243-1246, 2005.
- [14] H. Gao, J. Henzie, and T. W. Odom, "Direct evidence for surface plasmon-mediated enhanced light transmission through metallic nanohole arrays," *Nano Letters*, vol. 6, pp. 2104-2108, 2006.
- [15] R. Wood, "Anomalous diffraction gratings," *Physical Review*, vol. 48, p. 928, 1935.
- [16] B. Luk'yanchuk, N. I. Zheludev, S. A. Maier, N. J. Halas, P. Nordlander, H. Giessen, *et al.*, "The Fano resonance in plasmonic nanostructures and metamaterials," *Nature materials*, vol. 9, pp. 707-715, 2010.
- [17] Y. Sonnefraud, N. Verellen, H. Sobhani, G. A. Vandenbosch, V. V. Moshchalkov, P. Van Dorpe, *et al.*, "Experimental realization of subradiant, superradiant, and Fano resonances in ring/disk plasmonic nanocavities," *ACS nano*, vol. 4, pp. 1664-1670, 2010.
- [18] Y. Francescato, V. Giannini, and S. A. Maier, "Plasmonic systems unveiled by Fano resonances," *ACS nano*, vol. 6, pp. 1830-1838, 2012.
- [19] M. Rahmani, B. Lukiyanchuk, B. Ng, A. Tavakkoli KG, Y. Liew, and M. Hong, "Generation of pronounced Fano resonances and tuning of subwavelength spatial light distribution in plasmonic pentamers," *Optics express*, vol. 19, pp. 4949-4956, 2011.

- [20] J. Elliott, I. I. Smolyaninov, N. I. Zheludev, and A. V. Zayats, "Wavelength dependent birefringence of surface plasmon polaritonic crystals," *Physical Review B*, vol. 70, p. 233403, 2004.
- [21] S.-H. Chang, S. Gray, and G. Schatz, "Surface plasmon generation and light transmission by isolated nanoholes and arrays of nanoholes in thin metal films," *Optics Express*, vol. 13, pp. 3150-3165, 2005.
- [22] S. Wu, Q.-j. Wang, X.-g. Yin, J.-q. Li, D. Zhu, S.-q. Liu, *et al.*, "Enhanced optical transmission: Role of the localized surface plasmon," *Applied Physics Letters*, vol. 93, p. 101113, 2008.
- [23] P. Lalanne, J. Rodier, and J. Hugonin, "Surface plasmons of metallic surfaces perforated by nanohole arrays," *Journal of Optics A: Pure and Applied Optics*, vol. 7, p. 422, 2005.

Chapter 5

Summary, Conclusion and Future Work

5.1 Summary and Conclusion

This thesis explored the fabrication of plasmonic nanohole arrays and their potential for use in biosensing applications. The objective was to demonstrate their use in a proof of concept, point of care diagnostic system

In Chapter 2, nanohole arrays in thin Au films have been simulated, and then fabricated by FIB milling and assembled onto glass substrates. The holes have a diameter of 110nm and a pitch of 450 nm. The arrays are characterised using a number of techniques, including: optical microscopy, SEM, AFM and transmission spectrum. It was shown that they can detect refractive index changes by measuring the spectra in solution of varying concentrations of salt water. A bioassay and the attachment chemistry was developed, which led to assay development on the nanohole arrays, where the transmission spectrum showed a shift as each layer of biomaterial was attached.

In Chapter 3, a benchtop system was designed and implemented, to use the nanohole arrays for real time sensing. This involved integrating the optical setup, software program, microfluidic system and the nanohole sensors. There were two iterations of the optical setup designed to achieve a low cost setup capable of measuring the spectral changes caused by biomolecule attachment. The microfluidic system was integrated with the optical setup to give independent addressing of two individual nanohole arrays. The algorithms to record and analyse the spectra was written to measure the slopes on either side of the plasmonic dip and calculate the intersection point. All of these parameters were displayed on-screen in real time. An assay using pancreatic cancer biomarkers was developed and optimised on an SPR platform. This assay was extensively tested and allowed multiplexed detection of both 4 $\mu\text{g/ml}$ C1q antigen and 4 $\mu\text{g/ml}$ C3 antigen in buffer in real time. Also, it was shown that the system was selective (no non-specific binding). Finally, C1q Ag was successfully detected in 2% human serum.

In Chapter 4, elliptical nanoholes were examined in detail. Holes with dimensions of 150 nm for the minor axis and 350 nm for the major axis were fabricated, with a lattice period of 450 nm, in thin gold films. These nanoholes were simulated and compared to the fabricated samples. The transmission spectra of both the fabricated and simulated

nanoholes have sharp asymmetric features and show strong optical anisotropy. The simulated near field profile suggests the peaks are Fano resonances between the SPPs and RAs. Polarised transmission images showed both visible and invisible colour changes, simultaneous white/bright under one polarisation state and blue/dark by 90° rotation. Using these nanohole arrays in a security label would be quite unique and would be very challenging to illegally reproduce.

5.2 Future Work

There is currently a tremendous interest in multiplexed, remote sensing for biological applications. In this regards, the nanoplasmonic sensors developed throughout the course of this project offer attractive prospects. Indeed, the fabrication method described in Chapter 2, allows the samples to be transferred onto any substrate, including optical fibers (tip or core). Further work would be required for the optical interrogation.

Also, while the FIB method reported in this work is suitable for the research and development of the nanohole arrays, other methods have the potential to offer high throughput, low cost manufacturing. Fabrication of nanohole arrays using nanoimprint lithography for example would allow rapid and waferscale fabrication of the plasmonic sensor. Work in this area is currently on-going in the NTG lab.

Another area of interest lies in the functional layer. Use of novel molecules such as functional polymers could extend the capabilities of the plasmonic sensors from biological sensing to chemical sensing.

Finally, further development of the integrated platform (both on the optical and microfluidics parts) could allow higher multiplexing, higher sensitivities and lower footprint at lower cost. Work in this direction is also on-going in the NTG lab.

Appendices

A1. Abbreviations

Ab	Antibody
AFM	Atomic Force Microscopy
Ag	Antigen
Au	Gold
CCD	Charge-Coupled Detector
CMOS	Complementary Metal-Oxide Semiconductor
Cr	Chrome
DI	De-ionised
DNA	Deoxyribonucleic Acid
EDC	ethyl-(N',N'-dimethylamino)propylcarbodiimide hydrochloride
ELISA	Enzyme-Linked Immunosorbent Assay
EOT	Extraordinary Transmission
FDTD	Finite Difference Time Domain
FIB	Focussed Ion Beam
Ga	Gallium
HCl	Hydrochloric Acid
IgG	Immunoglobulin G
IL	Interference lithography
IPA	Isopropanol Alcohol
LED	Light Emitting Diode
LSP	Localized Surface Plasmon
MDA	Mercaptododecanoic acid
MHDA	Mercaptohexadecanoic acid
N ₂	Nitrogen
NaCl	Sodium Chloride (Salt)
NHS	N-hydroxysulfosuccinimide
PBS	Phosphate Buffered Saline

PDMS	Polydimethylsiloxane
PML	Perfectly Matched Layers
POC	Point Of Care
PSP	Phase Shifting Photolithography
QCM	Quartz Crystal Microbalance
RA	Raleigh Anomaly
RIU	Refractive Index Unit
RMS	Root Mean Square
SEM	Scanning Electron Microscopy
scFv	Single Chain Variable Fragment
Si	Silicon
SPP	Surface Plasmon Polariton
SPR	Surface Plasmon Resonance
UV	Ultra Violet
VCSEL	Vertical-Cavity Surface-Emitting Laser

A2. Peer Reviewed Publications

- [1] **D. Jones**, N. Liu, B. Corbett, P. Lovera, A. Quinn, and A. O'Riordan, "Surface Plasmon assisted extraordinary transmission in metallic nanohole arrays and its suitability as a bio-sensor," in *Journal of Physics: Conference Series*, 2011, p. 012005.
- [2] P. Lovera, **D. Jones**, B. Corbett, and A. O'Riordan, "Polarization tunable transmission through plasmonic arrays of elliptical nanopores," *Optics express*, vol. 20, pp. 25325-25332, 2012.
- [3] P. Lovera, **D. Jones**, and A. O'Riordan, "Elliptical nanohole array in thin gold film as micrometer sized optical filter set for fluorescent-labelled assays," in *Journal of Physics: Conference Series*, 2011, p. 012006.
- [4] C. Schopf, A. Martín, M. Burke, **D. Jones**, A. Pescaglioni, A. O'Riordan, *et al.*, "Au nanorod plasmonic superstructures obtained by a combined droplet evaporation and stamping method," *Journal of Materials Chemistry C*, vol. 2, pp. 3536-3541, 2014.

A3. Publications in Preparation

- [5] **D. Jones**, P.Lovera, M. Mitchell, and A. O'Riordan, "Fabrication of nanohole arrays and their use as label free biosensors", submitted to *Biosensors & Bioelectronics*
- [6] **D. Jones**, P.Lovera, M. Mitchell, and A. O'Riordan, "A point of care platform for label-free, multiplexed, real-time detection of pancreatic cancer biomarkers", *Biosensors & Bioelectronics*

A4. Conferences Attended

- [1] Institute of Physics: Sensors & their Applications XVI, Tyndall National Institute, Cork, Ireland (Oral Presentation), 2011

- [2] Postgraduate Symposium on Nanotechnology, University of Birmingham, United Kingdom (Oral Presentation), 2011

A5. LabVIEW block diagram

